Preparation, Characterization and Testing of an Electrochemical Pumping System for Modifying the Nonstoichiometry of Cerium Oxide CeO_{2-x}

Präparation, Charakterisierung und Test eines elektrochemischen Pump-Systems

zur Modifizierung der Nichtstöchiometrie von Ceroxid CeO_{2-x}

Dissertation

zur Erlangung des akademischen Grades

Dr. rer. nat.

am Fachbereich 08

der Justus-Liebig-Universität Gießen

Florian Rink

Gießen, 2026

Selbstständigkeitserklärung

Ich erkläre: Ich habe die vorgelegte Dissertation selbstständig und ohne unerlaubte fremde Hilfe und nur mit den Hilfen angefertigt, die ich in der Dissertation angegeben habe. Alle Textstellen, die wörtlich oder sinngemäß aus veröffentlichten Schriften entnommen sind, und alle Angaben, die auf mündlichen Auskünften beruhen, sind als solche kenntlich gemacht. Ich stimme einer evtl. Überprüfung meiner Dissertation durch eine Antiplagiat-Software zu. Bei den von mir durchgeführten und in der Dissertation erwähnten Untersuchungen habe ich die Grundsätze guter wissenschaftlicher Praxis, wie sie in der „Satzung der Justus-Liebig-Universität Gießen zur Sicherung guter wissenschaftlicher Praxis“ niedergelegt sind, eingehalten.

Angaben zu auf künstlicher Intelligenz (KI) basierender Hilfen wie ChatGPT oder SchulKI von OpenAI oder Gemini von Google zur Erstellung meiner Dissertation (Zutreffendes angekreuzt):

☐ Ich habe bei der Erstellung dieses Textes kein KI-Tool verwendet.

☒ Ich habe ein KI-Tool in den folgenden Bereichen eingesetzt (Mehrfachnennungen möglich):

- ☒ Ideen finden, meine Kreativität anregen
- ☐ Verstehen von Konzepten, Recherche von Fakten und Definitionen
- ☒ Optimierung eines von mir verfassten Textes
- ☐ Erstellen ganzer Textpassagen nach meinen Vorgaben

Folgende KI-Tools habe ich verwendet, damit aufgeführte Teile meines Textes von dem Tool wie folgt profitiert haben:

Im Rahmen dieser Arbeit habe ich die KI-Tools ChatGPT und DeepL genutzt. ChatGPT und DeepL habe ich jeweils für die Optimierung eines von mir verfassten Textes genutzt. Des Weiteren habe ich ChatGPT genutzt, um wissenschaftliche Veröffentlichungen zu recherchieren.

_____ _____

Ort, Datum Florian Rink

Die vorliegende Arbeit wurde im Zeitraum von Mai 2022 bis März 2026 am Physikalisch-chemischen Institut der Justus-Liebig-Universität Gießen unter Betreuung von Prof. Dr. Dr. h.c. Jürgen Janek angefertigt.

Dekan:	Prof. Dr. Holger Zorn
Erster Gutachter:	Prof. Dr. Dr. h.c. Jürgen Janek
Zweiter Gutachter:	Prof. Dr. Herbert Over
Arbeit eingereicht:	25.03.2026
Tag der Disputation:	27.05.2026

Danksagung

An erster Stelle möchte ich mich in besonderem Maße bei **Prof. Dr. Dr. h.c. Jürgen Janek** bedanken. Ich danke ihm für die Aufnahme in seine Arbeitsgruppe, die vielen Möglichkeiten zum fachlichen Austausch und die allgemein sehr gute Betreuung.

In besonderem Maße möchte ich mich ebenfalls bei **Prof. Dr. Herbert Over** bedanken. Auch ihm danke ich für die (inoffizielle) Aufnahme in seine Arbeitsgruppe und die Möglichkeiten zum fachlichen Austausch. Außerdem danke ich ihm für Erstellung des Zweitgutachtens.

Ein weiteres Dankeschön möchte ich **Dr. Bjoern Luerßen** aussprechen. Sowohl organisatorisch als auch fachlich konnte er mir immer weiterhelfen. Von seinem Wissen über das Pt/YSZ-Elektrodensystem habe ich stets profitieren können.

Auch **Prof. Dr. Matthias Elm** möchte ich an dieser Stelle danken. Ich danke ihm für die (spontanen) fachlichen Diskussionen und die (Wieder-)Inbetriebnahme des Röhrenofens, an dem ich gefühlt die Hälfte meiner Promotion gesessen habe.

Als nächstes möchte ich mich in hohem Maße bei **Dr. Boris Mogwitz** bedanken. Bei technischen Fragen oder Problemen konnte er mir jedes Mal weiterhelfen. So danke ich ihm unter anderem für die zahlreichen Hilfestellungen im Umgang mit der PLD-Anlage.

Des Weiteren möchte ich **Dr. Sebastian Benz** und **Dr. Joachim Sann** für die Unterstützung bei der Etablierung und Durchführung der (*operando*-)XPS-Messungen danken. Für die Diskussion und Auswertung der dabei entstandenen Daten möchte ich mich ebenfalls bei **Lorena Glatthaar** bedanken.

Für die Raman-Messungen und den kollegialen Umgang mit der PLD-Anlage möchte ich mich außerdem bei **Julius Dinter** bedanken.

Einen weiteren Dank möchte ich an **Dr. Volkmar Koller** richten, der mir die ersten Schritte bei der Bearbeitung des Projektes erleichterte. Für die Zusammenarbeit im Projekt möchte ich mich in diesem Rahmen ebenfalls bei **Alexander Spriewald-Luciano** bedanken.

Zudem möchte ich mich bei **Dr. Miguel Wiche** für die allwöchentlichen Kaffeepausen bedanken, die stets eine willkommene Unterbrechung des Arbeitsalltags darstellten.

Abschließend gilt mein besonderer Dank meinen Eltern, **Anne** und **Harald**, meinem Bruder **Fabian** und meiner Freundin **Clara**, die mich seit dem ersten Tag der Promotion beständig begleitet und unterstützt haben.

Zusammenfassung

Ceroxid gilt als vielversprechendes Katalysator-Material für die HCl-Oxidation. In diesem Zusammenhang konnte bereits gezeigt werden, dass der Oxidationszustand von Ceroxid (CeO_{2-x}, $0 \leq x \leq 0{,}5$) dessen katalytische Aktivität beeinflusst. Für eine genauere Untersuchung dieses Einflusses wäre jedoch ein System wünschenswert, das die kontrollierte Modifikation während der Katalyse ermöglicht. An dieser Stelle setzt die vorliegende Arbeit an. Basierend auf dem Pt/YSZ-Elektrodensystem wurde ein elektrochemisches Pump-System entwickelt, mit dem der Oxidationszustand einer CeO_{2-x}(111)-Schicht gezielt verändert werden kann. Die Ceroxid-Schichten wurden mittels gepulster Laserdeposition hergestellt und mithilfe von Rasterelektronenmikroskopie, Röntgendiffraktometrie, Raman-Spektroskopie und Röntgenphotoelektronenspektroskopie charakterisiert. Darüber hinaus wurden elektrochemische Messungen an verschiedenen (CeO_{2-x}/)Pt/YSZ/Pt-Systemen durchgeführt. Bereits mittels Impedanzspektroskopie, Zyklovoltammetrie und potentiostatischen Polarisationsexperimenten konnten Effekte gefunden werden, welche durch die Ceroxid-Schicht bedingt waren und die Funktionalität des Pump-Systems andeuteten. Final konnte die Funktionalität des Pump-Systems dann mithilfe eines *operando*-Aufbaus gezeigt werden, der es erlaubte, Messungen der CeO_{2-x}-Oberfläche mittels Röntgenphotoelektronenspektroskopie bei hohen Temperaturen und nach dem Anlegen eines elektrischen Potentials durchzuführen. Hierbei konnte sowohl die Oxidation als auch die Reduktion der Ceroxid-Schicht nachgewiesen werden.

Abstract

Cerium oxide is considered a promising catalyst for HCl oxidation reaction. In this context, it has been found that the oxidation state of cerium oxide (CeO_{2-x}, $0 \leq x \leq 0.5$) influences the corresponding catalytic activity. For a more detailed investigation, however, a system would be desirable that allows the controlled modification of this. In this work, a respective approach is presented. Based on the Pt/YSZ electrode system, an electrochemical pumping system was devised that allows the oxidation state modification of a CeO_{2-x}(111) film. The cerium oxide films were prepared by pulsed laser deposition and characterized by scanning electron microscopy, X-ray diffraction, Raman spectroscopy and X-ray photoelectron spectroscopy. Beyond that, electrochemical measurements were conducted on various (CeO_{2-x}/)Pt/YSZ/Pt systems. Here, impedance spectroscopy, cyclic voltammetry and potentiostatic polarization experiments revealed effects caused by the cerium oxide film, indicating thereby the working principle of the pumping system. Ultimately, the working principle could be proven using an *operando* setup that allowed X-ray photoelectron spectroscopy measurements at high temperatures and after applying electric potentials. By this, oxidation as well as reduction of the cerium oxide film could be verified.

Table of Contents

1 Introduction

Chlorine (Cl_2) is among the most important basic chemicals as it is part of many industrial processes. In the first half year of 2025, the European chlorine production reached 3.9 Mega tons[1]. One of the main by-products in processes that contain Cl_2 is hydrogen chloride (HCl). Even though HCl can be used in some other processes, the amount of emerging HCl is too big, making it a huge industrial waste product. Regarding the importance of Cl_2 and the excess of HCl, processes that recover Cl_2 out of HCl are considered with big interest. Beyond energy intensive HCl electrolysis[2], the Deacon process, *i.e.*, heterogenous catalyzed HCl oxidation, is a less energy-consuming alternative. Here, HCl reacts with O_2 whereby Cl_2 and H_2O are formed (see Figure 1.1). For this process, ruthenium-based catalysts[3] have been established on an industrial scale. However, since ruthenium is rare and expensive, alternative catalysts are investigated. Among these, cerium oxide is a very promising material[4] as it is stable and very cheap. Its ability to reversibly incorporate and remove oxygen (CeO_{2-x}; $0 \leq x \leq 0.5$) while maintaining structural integrity led to interesting applications. In Deacon catalysis, this property becomes quite important since it was shown that the corresponding activity is related to the oxygen deficiency x of CeO_{2-x}[4,5].

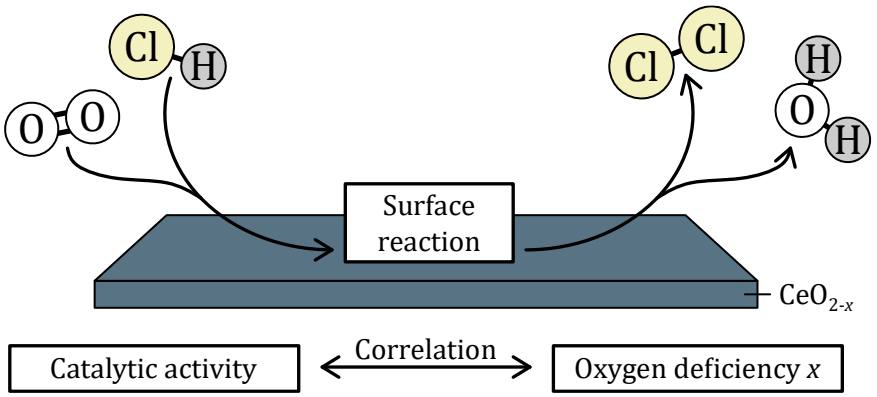

Figure 1.1: Deacon reaction, *i.e.*, heterogenous catalyzed HCl oxidation, on a cerium oxide surface. Hydrogen chloride (HCl) and molecular oxygen (O_2) are converted into chlorine (Cl_2) and water (H_2O). Catalytic activity is affected by the oxygen deficiency x of cerium oxide.

To further investigate this correlation, a system is desirable that enables the modification of oxygen deficiency in cerium oxide. Chueh et al.[6,7] devised an electrochemical system based on platinum (Pt) and yttria-stabilized zirconia (YSZ) that enabled a tuning of the oxidation state of a Sm-doped cerium oxide film. Their pumping approach is adapted in this work to generate a system that allows the modification of pure cerium oxide (see Figure 1.2). Two platinum thin films deposited on YSZ serve as basic cell system. One of these platinum electrodes is de-wetted so that the cerium oxide film on top can fill the respective trenches. Depending on the potential applied, oxygen ions can be either pumped to the de-wetted working electrode or away from it. Oxygen ions can then either diffuse into the cerium oxide film or out of it. By that, the cerium oxide film can be oxidized or reduced.

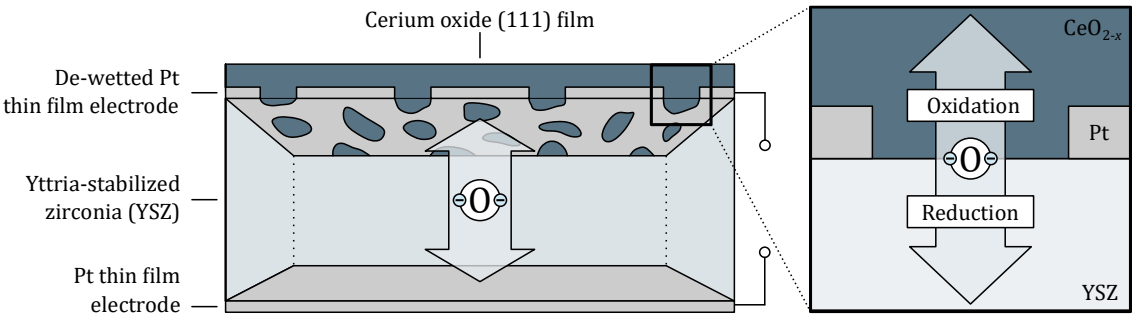

Figure 1.2: Illustration of an electrochemical pumping system for modification of the oxidation state of a cerium oxide (111) film. By applying a respective potential, oxygen ions can either be pumped to the de-wetted platinum electrode or away from it. At the interface of cerium oxide and YSZ, oxygen ions can then migrate into cerium oxide or out of it, meaning an oxidation or reduction of the film.

This work deals with the preparation, characterization and testing of a system as illustrated in Figure 1.2. This includes several issues to be addressed. In the following, these issues are outlined.

The first issue addressed in this work deals with the preparation of dense and crystalline cerium oxide films that exhibit a (111) preferential orientation. This facet is considered as the most stable one among the low index facets[8]. Accordingly, Deacon investigations on this specific surface have been already conducted[9–14]. The cerium oxide films were fabricated by pulsed laser deposition (PLD) and characterized by scanning electron microscopy (SEM) and X-ray diffraction (XRD). Besides, Raman spectroscopy (RS) and X-ray photoelectron spectroscopy (XPS) were applied to investigate the oxidation state.

A further part of this work deals with the preparation and electrochemical characterization of Pt/YSZ/Pt cell systems. As indicated by Figure 1.2, this cell type serves as base for the intended pumping system. Thus, respective investigations of oxygen transport and oxygen exchange reaction at the triple phase boundary O_2/Pt/YSZ were conducted. For this, electrochemical impedance spectroscopy (EIS) was applied.

A substantial issue of this work concerns the preparation and electrochemical characterization of a CeO_{2-x}/Pt/YSZ/Pt system as it is schematically shown in Figure 1.2. Here, impedance spectroscopy and cyclic voltammetry (CV) were performed to find effects that could be ascribed to the cerium oxide film, proving thereby the electrochemical integration of the cerium oxide film in the Pt/YSZ system. Beyond that, potentiostatic polarization experiments were conducted to examine differences between anodic and cathodic currents.

The last part of this work deals with *proof of principle* measurements that were conducted by *operando* XPS. Here, a setup for the XPS chamber is presented that enables the polarization of a respective CeO_{2-x}/Pt/YSZ/Pt system at elevated temperatures. By this, the working principle of the system, *i.e.*, the oxidation and reduction of the cerium oxide film, was examined.

2 Materials

Cerium oxide (CeO_{2-x}), yttria-stabilized zirconia (YSZ) and platinum (Pt) were employed as materials in this work. Cerium oxide and platinum were applied as films and YSZ was applied as substrate (see also Chapter 4.1). In this chapter, relevant physical and chemical properties as well as applications are presented.

2.1 Cerium Oxide (CeO_{2-x})

Physical and chemical properties

Cerium oxide (CeO_2) is an oxide of the element cerium. Cerium is a lanthanide and is more abundant than other elements like lead, mercury or cadmium[15]. Stoichiometric CeO_2 is pale yellow and crystallizes in the fluorite structure as illustrated in Figure 2.1. Here, the Ce^{4+} cations (blue) are present in a face-centered cubic sublattice. The O^{2-} anions (white) occupy the tetrahedral vacancies, leading to a simple cubic sublattice. The fluorite structure is present from room temperature to the melting point, which is around 2,477 °C.[16] The lattice constant of stoichiometric CeO_2 is 5.41 Å[17].

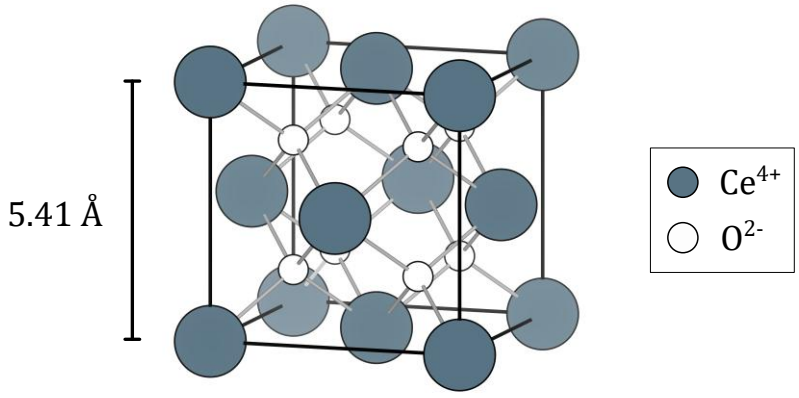

Figure 2.1: Fluorite structure of stoichiometric cerium oxide (CeO_2). The Ce^{4+} cations are present in a face-centered cubic lattice. The O^{2-} anions occupy the tetrahedral vacancies. The lattice constant is 5.41 Å.

A prominent property of cerium oxide is its ability to reversibly remove and incorporate oxygen. By reducing Ce^{4+} cations to Ce^{3+}, oxygen is removed from the lattice and oxygen vacancies are formed. The removal can be described by a Kroeger-Vink defect equation (2.1). For respective incorporation of oxygen, the reverse reaction applies.[16]

$$O_O + 2\,Ce_{Ce} \rightleftharpoons \frac{1}{2}\,O_2 + V_O^{\bullet\bullet} + 2\,Ce'_{Ce} \qquad (2.1)$$

With increasing oxygen removal, cerium oxide first turns blue and then black. By this, the lattice constant increases due to lower ionic radius of Ce^{4+} compared to Ce^{3+} [18]. The fluorite crystal structure, however, is maintained even with large amounts of removed oxygen[16]. For describing the nonstoichiometry, the formula CeO_{2-x} is commonly applied. Here, oxygen deficiency x can be between 0 (fully oxidized) and 0.5 (fully reduced). For investigation of the oxidation state, X-ray photoelectron spectroscopy is considered a quite common method[19–21]. Besides, Raman spectroscopy and X-ray absorption spectroscopy are further methods that can be applied[22].

The defect concentrations $[V_O^{\bullet\bullet}]$ and $[Ce'_{Ce}]$ depend on oxygen partial pressure $p(O_2)$ and on temperature. In general, the defect concentrations increase with higher temperature and decrease with higher oxygen partial pressure[23–25]. Based on Equation (2.1), the $p(O_2)$ dependence can be determined using the equilibrium constants and taking charge neutrality into account. By this, a $p(O_2)^{-1/6}$ dependence can be found for $[V_O^{\bullet\bullet}]$ and $[Ce'_{Ce}]$. However, this exponent only applies if the nonstoichiometry or the deficiency x is low. For higher x values, interactions between defects must be considered. One example is $(Ce'_{Ce}\,V_O^{\bullet\bullet}\,Ce'_{Ce})$ clustering, which affects the $p(O_2)$ dependence.[22] In air, the oxygen deficiency x is close to zero[26].

Pure cerium oxide is considered a mixed conductor with ionic and predominantly n-type electronic conductivity. Here, electronic conductivity is based on hopping of polarons, *i.e.*, an electron coupled to its surrounding lattice distortion. The ionic conductivity is based on oxygen vacancies. Therefore, cerium oxide is often doped with two- or three-valent metal oxides like CaO or Gd_2O_3 to increase and control the amount of oxygen vacancies and, by that, the ionic conductivity. A more detailed description of respective conductivities can be found in a review article by Mogensen et al.[16].

Applications of cerium oxide

Cerium oxide has many applications, especially in catalysis and electrochemistry. One prominent application can be found in automotive three-way catalysts (TWC). As a carrier material for precious metals, cerium oxide acts as an oxygen storage medium that can promote oxidation as well as reduction reactions. Accordingly, carbon monoxide (CO) and unburnt hydrocarbons can be oxidized, and nitrogen oxides (NO_x) can be reduced. Furthermore, cerium oxide is employed in solid oxide fuel cells (SOFC) and as catalyst in reforming reactions. Review articles by Montini et al.[27] or Sun et al.[28] give more insights into respective applications.

2.2 Yttria-stabilized Zirconia (YSZ)

Physical and chemical properties

Depending on temperature, pure zirconium dioxide (ZrO_2) can occur in three different crystal modifications. Up to a temperature of 1,100 °C, it has a monoclinic structure. Above this temperature, ZrO_2 transitions into a tetragonal crystal structure. At temperatures above 2,370 °C, it exhibits a cubic fluorite structure.[29] Here, the Zr^{4+} cations form a face-centered cubic sublattice where the O^{2-} anions occupy the tetrahedral gaps. The incorporation of metal oxides with lower cation valence can lead to a stabilization of the cubic phase. For that, yttrium oxide (Y_2O_3) is a prominent dopant, leading to yttria-stabilized zirconia (YSZ). For incorporation, Equation (2.2) can be formulated.

$$Y_2O_3 \xrightarrow{ZrO_2} 2\,Y'_{Zr} + 3\,O_O^X + V_O^{\bullet\bullet} \qquad (2.2)$$

When Y_2O_3 is incorporated, trivalent Y^{3+} ions replace tetravalent Zr^{4+} ions, resulting in a relative charge of −1 in each case (see Figure 2.2). To maintain the charge neutrality of the crystal, oxygen vacancies are formed, which have a relative charge of +2 to the lattice. At Y_2O_3 concentrations of approximately eight molar percent or higher, the cubic structure is stabilized, even at room temperature[30]. The lattice constant of cubic YSZ increases linearly with the amount of yttrium oxide added[31]. In this work, YSZ with 9.5 mol percent Y_2O_3 was employed, exhibiting a lattice constant of 5.13 Å[31].

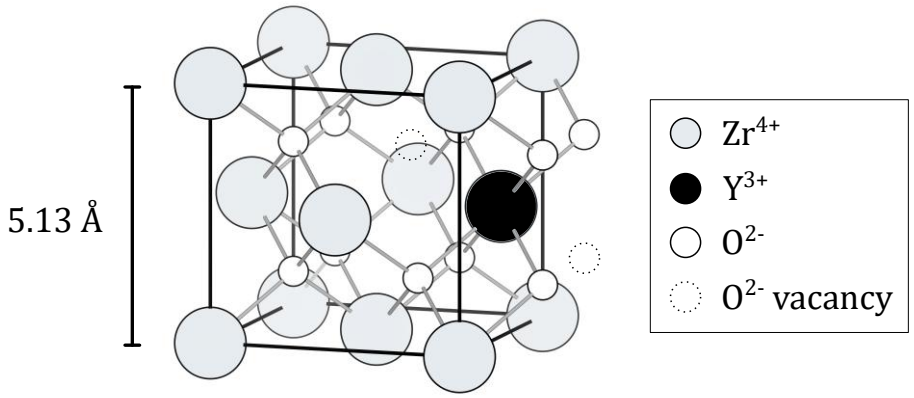

Figure 2.2: Crystal structure of yttria-stabilized zirconia. Fluorite structure of ZrO_2 and schematically introduced Y_2O_3, leading to the formation of oxygen vacancies (dashed lines). The lattice constant is 5.13 Å as YSZ with 9.5 mol percent Y_2O_3 was used in this work.

Over a wide $p(O_2)$ range, YSZ is considered a pure ionic conductor, whose electronic contributions to the total conductivity are negligible ($\sigma_{total} \approx \sigma_{ion}$). The ionic conductivity is based on the movement of oxygen vacancies and increases consequently with higher Y_2O_3 doping level. However, the maximum conductivity is reached at approximately 8 mol percent Y_2O_3[30,32,33]. Besides, the temperature-dependent ionic conductivity cannot be described by a single activation energy[30] since the activation energy decreases with increasing temperature. This is commonly ascribed to the interaction of Y'_{Zr} and $V_O^{\bullet\bullet}$ defects, which form $(Y'_{Zr}V_O^{\bullet\bullet})^{\bullet}$ and $(Y'_{Zr}V_O^{\bullet\bullet}\,Y'_{Zr})^{X}$ complexes, resulting in an immobilization of oxygen vacancies. However, at higher temperatures, these complexes decay, and the previously 'frozen' oxygen vacancies contribute to ionic conduction.[34]

Applications of yttria-stabilized zirconia

Due to high oxygen conductivity and stability at elevated temperatures, electrolytes based on yttria-stabilized zirconia are frequently used in solid oxide fuel cells (SOFC)[35,36]. YSZ is further applied in gas sensors[37] like oxygen sensors, which are used to determine the oxygen content in exhaust gases. Beyond these electrochemical applications, YSZ is employed as thermal barrier coating (TBC) for protection of metallic components due to low thermal conductivity[38].

2.3 Platinum (Pt)

Physical and chemical properties

Platinum (Pt) is a rare chemical element that belongs to the group of precious metals. It is characterized by high chemical and thermal stability. In addition, platinum exhibits high electrical conductivity ($\rho_{25°C}$ = 10.7 · 10^{-8} Ωm[17]) as well as high thermal conductivity ($\lambda_{27°C}$ = 0.716 W/cmK[17]). Platinum crystallizes in a face-centered cubic structure with a lattice constant of 3.92 Å[39] (see Figure 2.3). The melting point is 1,769 °C. Important oxidation states of platinum are +2 and +4, the highest oxidation state is +6.[15]

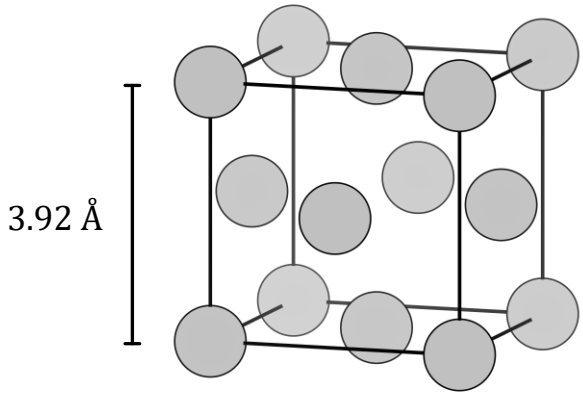

Figure 2.3: Face-centered cubic unit cell of platinum. The lattice constant is 3.92 Å.

Applications of platinum

Platinum exhibits a broad range of applications, especially in heterogenous catalysis. Its use in automotive three-way catalysts (TWC) is of particular importance for reduction of exhaust emissions. Beyond that, platinum-based catalysts are used in numerous organic syntheses. Due to its conductivity and chemical inertness, platinum is also considered a prominent electrode material and is applied in fuel cells and electrolysis systems. A review article by Hughes et al. provides more insights into respective applications[40].

3 Theoretical Background

This chapter provides a theoretical background for this work. In Chapter 3.1, key aspects of the Pt/YSZ electrode system are presented. This system serves as the electrochemical base for the intended pumping system. Chapter 3.2 introduces cerium oxide as a Deacon catalyst and highlights the importance of oxygen vacancies in this regard. By combining the Pt/YSZ electrode system with cerium oxide, Chapter 3.3 depicts the intended pumping system. Chapter 3.4 concludes this chapter by presenting essentials in solid state diffusion and ionic conductivity.

3.1 The Pt/YSZ System

General aspects

The Pt/YSZ electrode system is widely employed in high temperature electrochemistry, combining the ionic conductivity of yttria-stabilized zirconia with the electronic conductivity and catalytic activity of platinum (see Chapters 2.2 and 2.3). For both practical applications and fundamental studies, Pt/YSZ is considered an important system and is, *e.g.*, employed for solid oxide fuel cells and oxygen sensors. It is also of particular importance for catalytic processes. Here, the electrochemical promotion of catalysis (EPOC) or non-Faradaic electrochemical modification of catalytic activity (NEMCA) marks a major research topic[41–50].

Figure 3.1 shows schematically a Pt/YSZ/Pt cell in an oxygen-containing atmosphere. When a potential is applied between the platinum electrodes, oxygen ions move to the anode and oxygen vacancies move to the cathode. At the anode, oxygen ions are oxidized and removed from the YSZ lattice (see Equation 3.1). Vice versa, at the cathode, oxygen is reduced and incorporated into the YSZ lattice by occupying a vacancy. Both the oxidation reaction and the reduction reaction take place at the triple phase boundary of oxygen, platinum and YSZ.

$$O_O^X \rightleftharpoons V_O^{\bullet\bullet} + 2\,e^- + \frac{1}{2}\,O_2 \qquad (3.1)$$

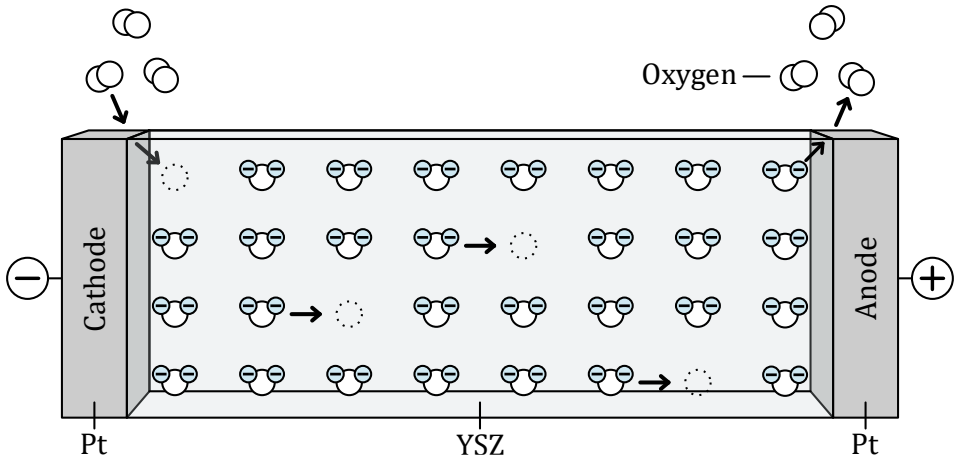

Figure 3.1: Principle of a Pt/YSZ/Pt cell with applied potential. Oxygen ions move to the anode where they are oxidized and removed from the lattice. At the cathode, oxygen is reduced and incorporated into the lattice. The reactions occur, respectively, at the triple phase boundary of oxygen, platinum and YSZ.

The triple phase boundary O_2/Pt/YSZ

The electrode characteristics are mainly defined by the triple phase boundary (TPB) of oxygen, platinum and YSZ (O_2/Pt/YSZ). Here, oxidation and reduction of oxygen take place (see Equation (3.1)). For illustration of the corresponding mechanisms, Figure 3.2 shows a Pt/YSZ/Pt cell with highlighted TPB. When the platinum working electrode (WE) is polarized anodically (positively vs. counter electrode (CE)), oxygen ions (O^{2-}) migrate towards the WE where they are oxidized by transferring two electrons to the platinum electrode. The remaining oxygen species (O) is thereby removed from the YSZ lattice and migrates to the platinum surface. Here, it can diffuse on the surface and recombine with further O species whereby molecular oxygen (O_2) is formed. In a further step, this oxygen can desorb from the platinum surface. Vice versa, when the platinum working electrode is polarized cathodically (negatively vs. CE), the reverse reaction takes place. The oxygen species located on the platinum surface are reduced by receiving two electrons from the platinum electrode. The resulting oxygen ion is then incorporated into the YSZ lattice.[51,52]

In general, the longer the triple phase boundary per area is the more oxygen can be exchanged[53–56]. In electrochemical measurement techniques, this corresponds to higher current or lower resistance values for the electrode process. This was, *e.g.*, shown in a work by Opitz et al.[53]. They deposited round and dense platinum electrodes with various diameters on YSZ and performed electrochemical impedance spectroscopy on these electrodes. It turned out that the resistance attributed to the oxygen exchange reaction decreases inversely with the perimeter of the electrode, which represents the length of the triple phase boundary.

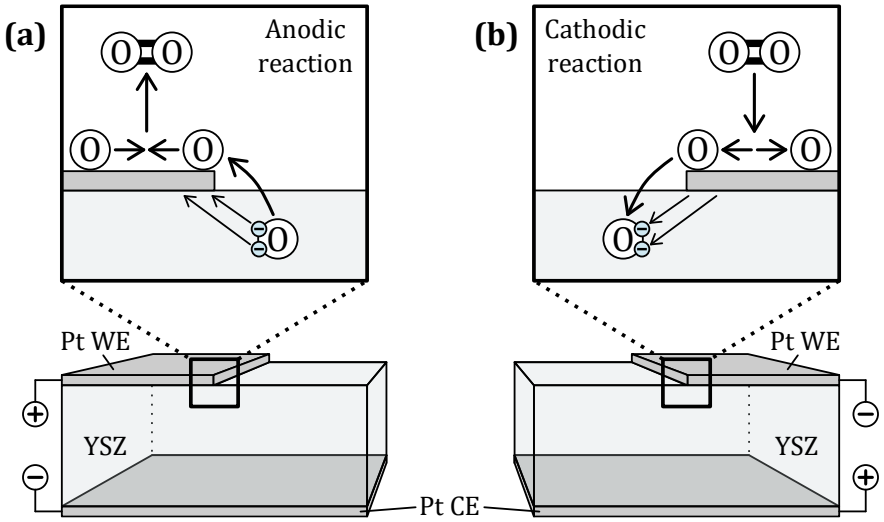

Figure 3.2: Reactions occurring at the triple phase boundary of oxygen, platinum and YSZ; **(a)** anodic reaction, *i.e.*, the removal of oxygen ions out of YSZ; **(b)** cathodic reaction, *i.e.*, the incorporation of oxygen ions into YSZ.

Formation of platinum oxides (PtO_x)

The formation of platinum oxides (PtO_x) represents an important issue for the Pt/YSZ electrode system[57–63]. Platinum oxides can form reversibly under oxidative conditions like anodic polarization or high oxygen partial pressures. Platinum oxides influence the electrochemical properties as they impede the oxygen exchange reaction. This was, *e.g.*, shown in a study by Pöpke et al.[57] where anodic polarization caused an increase of the impedance resistance attributed to the oxygen exchange reaction. Conversely, cathodic polarization led to a decrease for the respective resistance due to the decomposition of platinum oxides (see Figure 3.3). In a further study, Pöpke et al.[63] investigated the passivation of a de-wetted platinum electrode at elevated temperatures in air. Here, respective impedance measurements indicated that the resistance attributed to the oxygen exchange reaction increases linearly with square root of time.

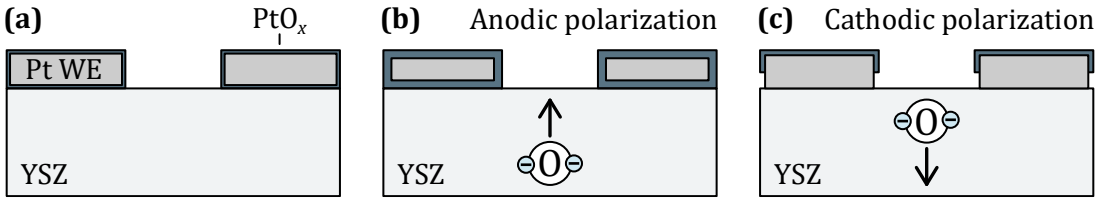

Figure 3.3: The role of PtO_x in the Pt/YSZ system; derived from Pöpke et al.[57]; **(a)** relaxed system; **(b)** formation of PtO_x through anodic polarization; **(c)** decomposition of PtO_x through cathodic polarization.

Polarization induced changes in the Pt/YSZ system

In this subchapter, specific phenomena that can occur through anodic or cathodic polarization of Pt/YSZ electrode systems are presented. For a theoretical view on polarized Pt/YSZ electrode systems, a work by Janek et al.[44] gives more insights.

Under strong anodic polarization, morphological changes in dense platinum film electrodes can occur[50,58,64,65] (see Figure 3.4). Here, oxygen ions move to the Pt/YSZ interface where they are oxidized. The resulting O species recombine with each other, and molecular oxygen is formed (see (a)). As this process continues, the increasing O_2 pressure leads to a delamination of the platinum film and thereby to the formation of bubbles (see (b)). These bubbles can even lead to a cracking of the platinum film (see (c)), whereby oxygen escapes. By this, the triple phase boundary grows.

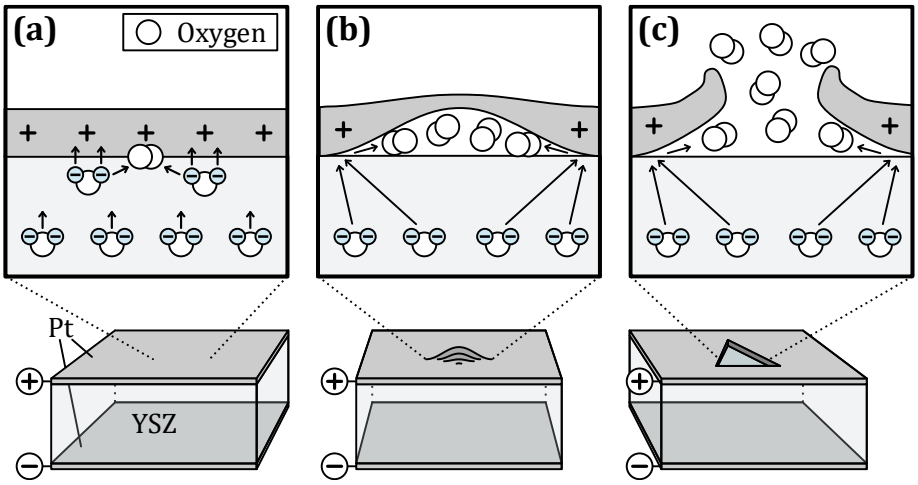

Figure 3.4: Cracking of dense platinum film electrodes on YSZ caused by anodic polarization; **(a)** oxygen ions are oxidized and recombine at the Pt/YSZ interface, whereby molecular oxygen is formed; **(b)** formation of a bubble containing molecular oxygen and delamination of the platinum film; **(c)** cracking of the platinum film and escaping of oxygen molecules.

Under strong cathodic polarization, yttria-stabilized zirconia can undergo electrochemical blackening, *i.e.*, the reduction of the electrolyte. This process is associated with the formation of oxygen vacancies and the reduction of Zr^{4+} cations, which causes the material to darken. Within the reduced areas, the electronic conductivity is significantly increased and the ionic conductivity is significantly decreased.[66,67]

3.2 Cerium Oxide as Catalyst for HCl Oxidation

In 1868, Henry Deacon developed a procedure to recover chlorine (Cl_2) out of hydrogen chloride (HCl). Based on a solid catalyst, HCl reacts with O_2 whereby H_2O and Cl_2 are formed (see Equation (3.2)). As the reaction is exothermic ($\Delta H^0 = -57$ kJ/mol), catalysts that exhibit high activity at low temperatures (<700 K) are required. Originally, copper-based materials were applied as catalysts for the Deacon reaction. However, by now, catalysts based on ruthenium oxide (RuO_2)[3] are commercially established as they are quite stable and active. Nevertheless, ruthenium is a rare and expensive metal, and its market price is highly volatile[68]. Therefore, alternative catalyst materials are investigated.[69–71]

$$4\ HCl + O_2 \rightleftharpoons 2\ Cl_2 + 2\ H_2O \qquad (3.2)$$

Among investigated Deacon catalysts, cerium oxide is considered a promising and cheap alternative. Fundamental studies by Amrute et al.[4] demonstrated both catalytic activity and stability for cerium oxide powders. The corresponding activity was ascribed to the presence of oxygen vacancies, which were occupied by chlorine atoms during the surface reaction. The stability was related to the resistance against chlorination, *i.e.*, the formation of an inactive $CeCl_3$ phase. Under O_2-rich conditions, however, chlorination was only observed for the outermost cerium oxide layers. In a further study, Li et al.[5] investigated shape-controlled cerium oxide nanoparticles as Deacon catalysts. It turned out that nano-rods possess higher catalytic activity than nano-cubes and nano-octaeders. This result was ascribed to the higher oxygen storage capacity (OSC) of nano-rods, emphasizing again the importance of oxygen vacancies.

For gaining deeper insights into the fundamental mechanisms of the Deacon reaction, recent studies[9,10,12–14] have focused on well-defined CeO_{2-x}(111) surfaces. Among the low-index facets, the (111) facet is considered the most stable[8]. In a work by C. Sack[9], various CeO_{2-x}(111) films were prepared and investigated. It was shown that stoichiometric CeO_2 films did not show any catalytic activity, which was ascribed to the absence of oxygen vacancies. In contrast, catalytic activity was observed on partially reduced cerium oxide films where Cl atoms could occupy the respective oxygen vacancies. Subsequent investigations on the mechanism were conducted by V. Koller[10].

For the underlying mechanism of HCl oxidation on partially reduced CeO_{2-x}(111) surfaces, a Mars-van-Krevelen mechanism has been proposed[72] (see Figure 3.5). Here, hydrogen chloride (HCl) adsorbs and dissociates on the cerium oxide surface by an acid-base reaction. Cl fills an oxygen vacancy site and H is transferred to an oxygen atom forming an OH group (2). After that, a second HCl molecule dissociates on the surface forming an additional OH group and a Cl species on a Ce atom (3). By recombination of the two Cl species, chlorine (Cl_2) is formed (4). By desorption of Cl_2, an oxygen vacancy is re-created (5), which is filled with an oxygen molecule (O_2) (6). In the next step, the two OH groups recombine forming the by-product water (H_2O) and an oxygen vacancy (7,8). By cleavage of the oxygen molecule, this vacancy is occupied (9).

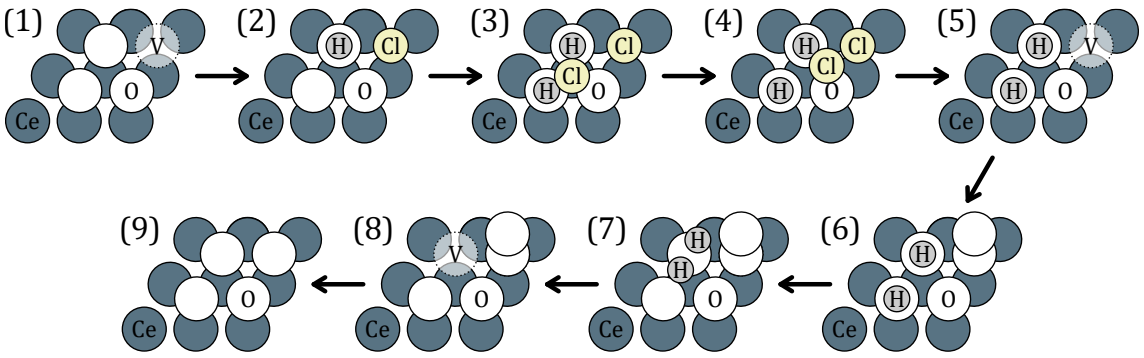

Figure 3.5: Proposed mechanism for HCl oxidation reaction on a partially reduced CeO_{2-x}(111) surface. Derived from Capdevila-Cortada et al.[72].

Although the proposed mechanism seems to be convenient, it has not been finally proven yet. Indeed, no HCl oxidation experiment on CeO_{2-x}(111) surfaces was performed that could validate this mechanism. Accordingly, a system would be desirable that enables the adjustment of oxygen vacancies independently of the reaction conditions. In literature, it was already demonstrated that CeO_{2-x}(111) films can be grown on Pt(111) surfaces[73–75]. Based on that, combining cerium oxide with the Pt/YSZ electrode system could provide an electrochemical system that allows the modification of oxygen deficiency in cerium oxide films. The respective approach is presented in Chapter 3.3.

3.3 Intended Pumping System CeO_{2-x}/Pt/YSZ/Pt

As described in Chapter 3.2, a device that enables the controlled modification of oxygen deficiency *x* in CeO_{2-x}(111) films would be desirable for fundamental investigations on the mechanisms behind the Deacon process. Chueh et al.[6,7] devised an electrochemical system based on Pt/YSZ that could be used for tuning the oxidation state of a Sm-doped CeO_{2-x}(100) film. Here, platinum thin films were deposited on both sides of a YSZ(100) single crystal and subsequently patterned into a comb-like structure using metal-liftoff photolithography. Sm-doped cerium oxide films were then grown on these patterned electrodes. In the present work, this concept is adapted and modified to evolve a system allowing the respective tuning of pure cerium oxide. The corresponding approach is presented in the following.

Based on a YSZ(111) substrate serving as the electrolyte, two platinum thin film electrodes are fabricated by pulsed laser deposition (PLD). One electrode is dense and the other is de-wetted. A cerium oxide (111) film is then deposited on the de-wetted Pt(111) thin film electrode, also by PLD. By that, cerium oxide fills the trenches of the de-wetted platinum film generating a CeO_{2-x}/YSZ interface (see Figure 3.6).

Applying a potential across the Pt/YSZ/Pt system, oxygen ions and accordingly oxygen vacancies start to move in the direction of the local field. Applying a negative potential to the de-wetted electrode as depicted in Figure 3.6, oxygen vacancies are accumulated beneath the cerium oxide film. Besides, Ce^{4+} ions are reduced to Ce^{3+}, enabling the diffusion of oxygen ions from cerium oxide into YSZ. By this, cerium oxide is reduced. For oxidation, the reverse process applies.

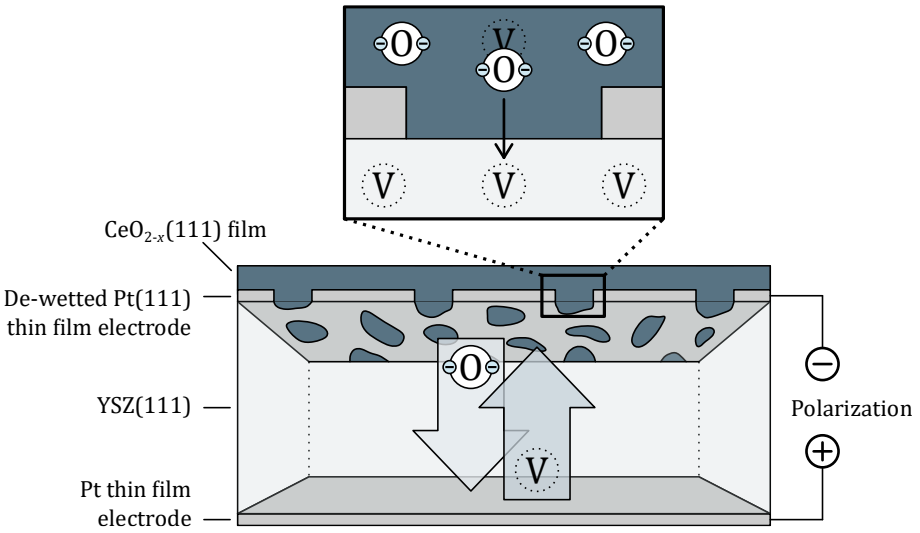

Figure 3.6: Pursued approach of this work, aiming at an electrochemical pumping system that enables the oxidation state modification of a cerium oxide (111) film. By applying negative potential to the de-wetted platinum electrode (vs. dense platinum electrode), oxygen vacancies are pumped beneath the CeO_{2-x}/YSZ interface. By reduction of Ce^{4+} ions to Ce^{3+}, oxygen ions can diffuse from cerium oxide into YSZ.

3.4 Diffusion and Ionic Conductivity in Solids

Diffusion

Diffusion, in general, describes the movement of species like atoms or ions within a medium caused by a gradient in concentration (as well as statistical motion in the absence of a driving force). For illustration, Figure 3.7 shows two types of atoms (white and blue) that are initially separated by an interface. By random movements of both species, however, a stepwise mixture is observed. As indicated by Figure 3.7, a gradient dc/dx in concentration of one species leads to a flux J of that species. The corresponding correlation is given by Fick's first law (see Equation (3.3)). Here, the diffusion coefficient D is a specific constant.

$$J = -D\frac{dc}{dx} \tag{3.3}$$

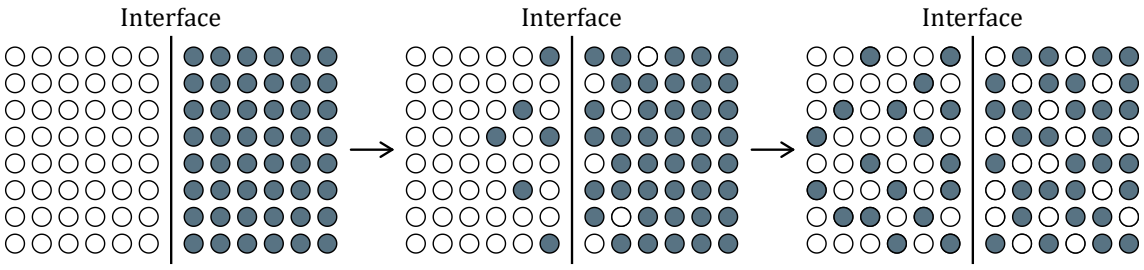

Figure 3.7: Illustration of diffusion by two initially separated atom species. With increasing time, the interface got stepwise blurred leading to a mixture of the species. Derived from a book by Tilley[26].

In crystalline solids, diffusion is based on defects like vacancies or interstitials enabling a species to leave a regular lattice site and occupy a vacant site. Here, the most common description is given by the random-walk model, which is based on a series of random jumps induced by thermal energy. Figure 3.8 (a) shows a one-dimensional energy profile consisting of alternating minima and maxima. The minima represent a regular lattice site for a species. For jumping to a vacant site in a distance a, a maximum or an energy barrier (Δg_m) must be overcome. The probability of jumping to the left or to the right is 0.5, respectively. In general, the jump frequency Γ increases with temperature T as shown by Equation (3.4). Here, k_B is the Boltzmann constant and ν is the attempt frequency.

$$\Gamma = \nu \exp\left(-\frac{\Delta g_\mathrm{m}}{k_\mathrm{B}T}\right) \tag{3.4}$$

Based on Equation (3.4), Equation (3.5) can be derived[26] for the diffusion coefficient *D*, emphasizing the temperature dependence of diffusion. Here, D_0 is a pre-exponential factor, E_A is the activation energy and *R* is the gas constant.

$$D = D_0 \exp\left(-\frac{E_A}{RT}\right) \tag{3.5}$$

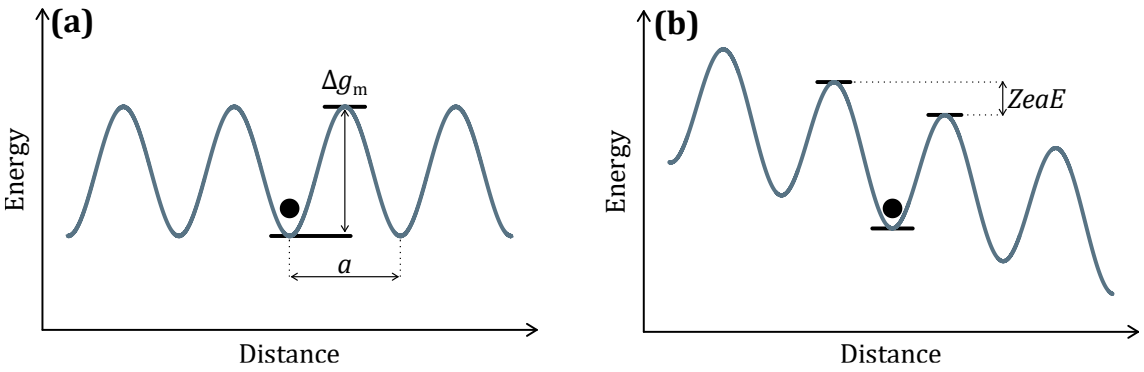

Figure 3.8: Illustration of energy barriers for one-dimensional random-walk model for ion movement within crystalline solids; **(a)** energy landscape without electric field; **(b)** energy landscape with applied electric field in +*x* direction. Figures are derived from a book by Tilley[26].

Ionic conductivity

Ionic conductivity is the movement of ions by applying an electric field. For description in a crystalline solid, the random-walk model for one dimension is applied again. Assuming an electric field *E* in +*x* direction, the energy barrier is modified as illustrated in Figure 3.8 (b). The barrier height becomes lower in +*x* direction (–0.5 *ZeaE*) and higher in –*x* direction (+0.5 *ZeaE*). This means that jumping of respective ions become more likely in +*x* direction than in the opposite direction. Based on random-walk model, Equation (3.6) can be derived[26] for ionic conductivity (= σ). The logarithmic plot (3.7) of this equation was applied in this work to determine activation energies. The corresponding σ values were calculated by Equation (3.8) out of the resistance values *R* (*d* = thickness of the electrolyte, *A* = electrode area).

$$\sigma T = \sigma_0 \exp\left(-\frac{E_A}{RT}\right) \tag{3.6}$$

$$\ln(\sigma T) = \ln(\sigma_0) - \frac{E_A}{k_B T} \tag{3.7}$$

$$\sigma = \frac{d}{RA} \tag{3.8}$$

4 Experimental Background

This chapter presents the methods as well as the corresponding devices and parameters employed in this work. The platinum and cerium oxide films were fabricated by pulsed laser deposition (PLD). For characterization of the films, scanning electron microscopy (SEM), X-ray diffraction (XRD), and profilometry were applied. Additionally, Raman spectroscopy (RS) and X-ray photoelectron spectroscopy (XPS) were used to investigate the oxidation state of the cerium oxide films. These film-related methods are presented in Chapter 4.1. For electrochemical characterization, impedance spectroscopy (EIS), cyclic voltammetry (CV) and potentiostatic polarization experiments were performed. These methods and the corresponding setup are presented in Chapter 4.2.

4.1 Preparation and Characterization of the Films

4.1.1 Pulsed Laser Deposition (PLD)

Pulsed laser deposition (PLD) is one of the physical vapor deposition methods and it is used to fabricate thin films. There is a wide range of material compositions that can be deposited by this method.

Figure 4.1 illustrates the setup used in this work as well as the operation process. For PLD, a target and a substrate are essential. They are placed inside a vacuum chamber and fixed by respective holders. The chamber itself consists of an inlet for various gases and a window through which laser light can pass. A shutter located in front of the vacuum pump enables the modification of pressure within the chamber. When performing PLD, laser pulses are adjusted to the rotating target. Thereby, atoms, ions, and electrons are ejected. A plasma plume is formed, which expands perpendicular to the target surface and towards the substrate, which is placed in the path of this plume. Atoms that reach the substrate can diffuse and aggregate on the surface and start growing a film. Heating the substrate promotes this self-assembly mechanism. A more detailed description of underlying mechanisms can be found in several review articles[76,77].

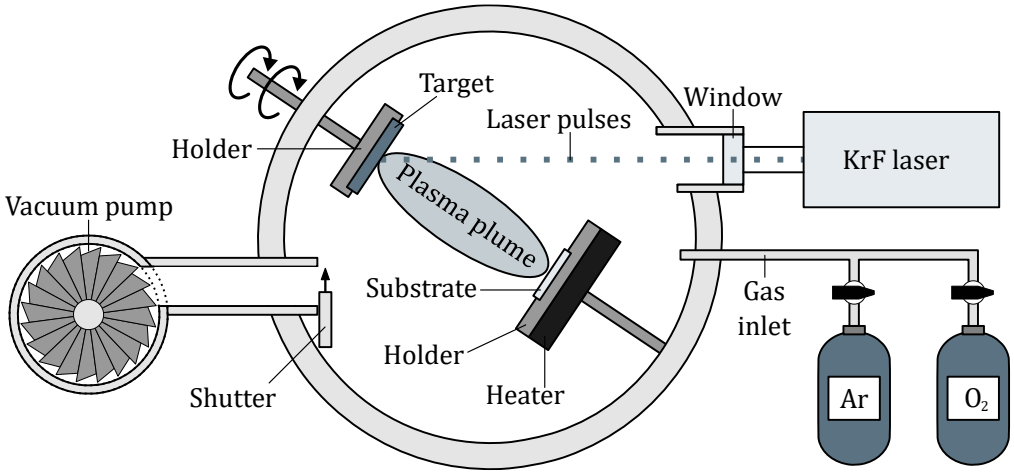

Figure 4.1: Illustration of pulsed laser deposition. Laser pulses are adjusted to the rotating target where respective material is ejected. A plasma plume is formed, which moves towards the substrate. At the substrate surface, self-assembly mechanisms lead to a growing film. By a gas inlet and a shutter to the vacuum pump, various gas pressures can be adjusted.

There is a wide range of parameters that can affect the properties of the resulting film. Firstly, laser energy E, pulse frequency f and laser spot size A are important as they define the power that is delivered to the target. Besides, the number of pulses N influences the final thickness of the film. A further point concerns the background gas since pressure p affects the expansion of the plasma plume. In general, higher pressure leads to more collisions and thus to a reduced kinetic energy of the plasma species reaching the substrate. Besides, the type of background gas can also play a decisive role for the final chemical composition of the film as reactive gases can react with the plasma species. As outlined above, heating the substrate is important for self-assembly or the crystallization process. Therefore, heater temperature $\vartheta_{\mathrm{Heater}}$ and thermal contact to the substrate (holder) are also crucial for final film properties. In a review article by Shepelin et al.[78] more specific information on the parameters can be found.

In this work, a KrF excimer laser[79] (λ = 248 nm) from *Coherent* was applied. The distance between the respective target and the substrate was approximately 4.1 cm for the depositions shown in Chapter 5, 7, 8, and 9. The cerium oxide depositions shown in Chapter 6 were prepared in another chamber with about 5 cm distance between target and substrate. To obtain the geometries shown in this work, stainless-steel masks were fixed on the substrate during deposition. Platinum targets from *Chempur* were applied (99.95% purity). The cerium oxide targets were self-made out of cerium oxide powder (*Sigma-Aldrich*, 99.99% purity). The preparation procedure is described in a work by M. Kleine-Boymann[80]. As substrates, one-side polished YSZ(111) crystals (9.5 mol percent Y_2O_3, *CrysTec*) with a volume of 10 mm × 10 mm × 0.5 mm were used.

4.1.2 Scanning Electron Microscopy (SEM)

Scanning electron microscopy (SEM) is an imaging method that can resolve the surface structure of a (conductive) sample in the nanometer range. For that, an electron beam is focused on a confined spot on the sample. The electrons of the beam can either be scattered back or transfer energy to the electrons of the sample. These electrons can thereby be released and leave the sample as secondary electrons, which are gathered by a detector. For the current position of the electron beam, a pixel is generated whose brightness depends on the number of secondary electrons detected. The electron beam can be moved by electrostatic or magnetic fields in two spatial directions. In this way, the beam scans over the sample and a corresponding pixel for each position is generated. More insights into SEM can be found in a book by Egerton[81].

A *Merlin* device from *Zeiss* was applied in this work. The acceleration voltage was 3 kV and the SE2 detector was used. The WD was between 3.8 mm and 6.8 mm.

4.1.3 X-ray Diffraction (XRD)

X-ray diffraction (XRD) is applied to investigate the crystalline structure of a sample. In a crystal, atoms are arranged periodically so that a crystal can be described as stacks of atom planes, which have a defined distance d (see Figure 4.2). When monochromatic X-rays with wavelength λ interact with this periodic crystal lattice, constructive interference occurs at specific angles θ that fulfill Bragg's law (4.1). By the resulting pattern, information about, *e.g.*, preferred crystal orientations can be obtained. Further information on XRD (on thin films) can be found in a review article by Harrington and Santiso[82].

In this work, an *X'Pert PRO MRD* device from *PANalytical* was used. Cu K_α radiation (λ = 1.541 Å) was used and the X-ray tube worked with 40 kV and 40 mA. The *pp collector* detector and the *mirror* optics were applied.

$$2d \sin(\theta) = n\lambda \tag{4.1}$$

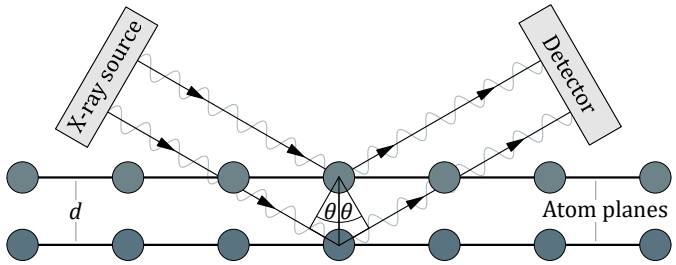

Figure 4.2: Illustration of X-ray diffraction. X-rays are diffracted at atom planes with distance d. The diffracted waves can interfere constructively or destructively depending on the angle θ.

4.1.4 Profilometry

The thickness of platinum and cerium oxide films was determined by an *AlphaStep D-600* device from *KLA Tencor*. The measurements were carried out by moving the stylus from the prepared film down onto the substrate. The recorded profile was normalized to the substrate. To compensate for fluctuations, several measurements were taken, and the average value was calculated. For several samples, it was not possible to measure the film thickness, *e.g.*, for cerium oxide films on de-wetted platinum or platinum films on unpolished YSZ.

4.1.5 Raman Spectroscopy (RS)

Raman spectroscopy (RS) can be applied to investigate structural properties of crystalline solids. For that, laser light is focused on a sample. The corresponding photons can be scattered elastically or inelastically by the sample. In case of elastic scattering, the incoming and scattered photons have the same energy. In case of inelastic scattering, an energy difference is given caused by an interaction between the photons and lattice vibrations. The photons can either transfer energy to the lattice or receive energy from it. The energy difference is represented by the Raman shift, *i.e.*, the change in wave number of incoming and inelastically scattered photons. The Raman shift represents distinctive vibrational modes of a material. In general, highly symmetric crystals only have a few Raman active modes, but lattice distortions can yield to additional modes. A book by Loudon[83] gives further information on Raman spectroscopy on solids.

In this work, an *In-Via* device with a charge-coupled device camera from *Renishaw* was used. The laser light (Cobalt 08-DPL) applied had a wavelength of 515 nm and a power of 50 mW.

4.1.6 X-ray Photoelectron Spectroscopy (XPS)

X-ray photoelectron spectroscopy (XPS) is a surface-sensitive analytical technique, which is used to investigate the chemical composition and bonding of a sample. Based on the photoelectric effect, photons with specific energy ($E = h \cdot \nu$) are focused on a sample where they can excite and eject core electrons (see Figure 4.3). Depending on binding energy E_B and work function ϕ, photoelectrons can be released from the sample and detected. By measuring their kinetic energy E_K, the binding energy can be calculated by Equation (4.2). The binding energy is characteristic for specific atomic orbitals and allows therefore the identification of elements. Moreover, further chemical information can be derived as the binding energy is sensitive to the oxidation state and to the local chemical environment of

detected species. Here, increasing oxidation leads to a decrease of electron density and therefore to a higher binding energy of a species. Effects like spin-orbit coupling or relaxation processes can additionally affect the resulting spectrum. A review article by Stevie and Donley[84] gives more insights into XPS technique.

$$E_{\mathrm{K}} = h \cdot \nu - E_{\mathrm{B}} - \phi \tag{4.2}$$

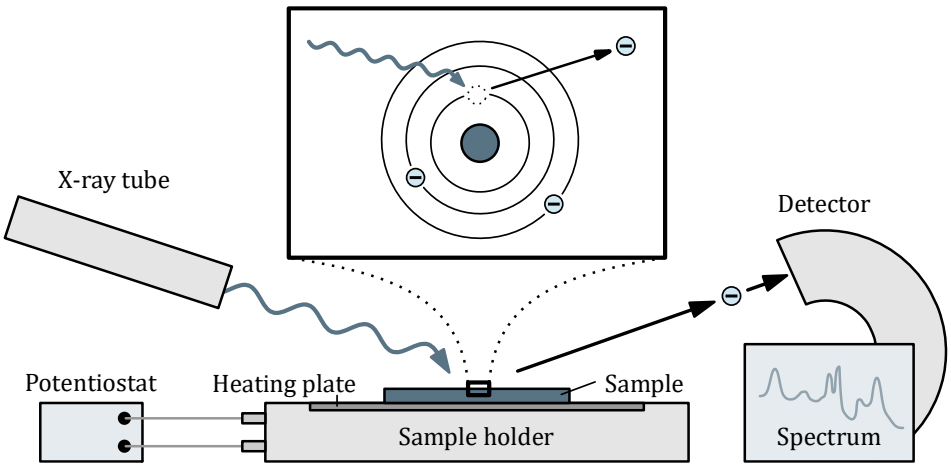

Figure 4.3: Illustration of (*operando*) X-ray photoelectron spectroscopy. X-ray photons excite and eject electrons from the sample, which can then leave the sample. Those photoelectrons are detected, and a respective spectrum is generated. For *operando* experiments a sample holder with heating plate and electrical pins was used that enables the connection of a potentiostat out of the XPS chamber.

XPS is frequently employed in *operando* experiments, enabling real-time investigations of electrochemical systems under operating conditions. By that, structural, chemical or electronic changes induced by an applied potential can be investigated. To perform *operando* experiments with ion-conducting solids, elevated temperatures are typically required, necessitating the use of a special setup. In literature, several approaches can be found, enabling XPS measurements at several hundred degrees Celsius[6,7,85–88]. Also in the present work, a specific setup was devised, allowing *proof of principle* measurements on the CeO_{2-x}/Pt/YSZ/Pt system (see Chapter 3.3) at approximately 385 °C. The description and discussion of the experimental setup are presented in Chapter 9.1.

A *PHI 5000 VersaProbe IV Scanning ESCA Microscope* device from *Physical Electronics* was used in this work. Monochromatized Al K_α X-ray radiation (E = 1486.6 eV) was applied. The spectra were normalized to the C 1s peak at 284.8 eV[89]. A *Zennium Pro* potentiostat from *Zahner* was connected to the XPS device for *operando* experiments.

4.2 Electrochemical Characterization

This chapter provides an overview of the electrochemical setup and the corresponding techniques applied in this work. As techniques, electrochemical impedance spectroscopy (EIS), cyclic voltammetry (CV) and potentiostatic polarizations were performed.

4.2.1 Preparation and Setup

For preparing samples for electrochemical characterization, corresponding platinum thin film electrodes were bonded with platinum wires as illustrated in Figure 4.4. In the first step, a piece of platinum wire (Ø = 0,1 mm, *ChemPur*, purity: 99.9%) was placed on the platinum thin film and fixed by *Ceramabond* (*T-E-Klebetechnik*, *Ceramabond 503*). After one hour, platinum paste (*ChemPur,* Item no.: *900487*) was brushed on the tip of the wire to bond it with the platinum thin film. Approximately 24 hours later the sample was turned, and the procedure was repeated to also bond the opposite electrode. Another 24 hours later, the sample was mounted in the tube furnace.

The electrochemical characterization was carried out combining a tube furnace (*Heraeus LT 14-0*) and a potentiostat (*Zahner*, *Zennium Pro*). Here, a ceramic sheathed wire extends into the interior of the furnace, allowing the bonding of respective wires by spot-welding. A two-electrode setup was used.

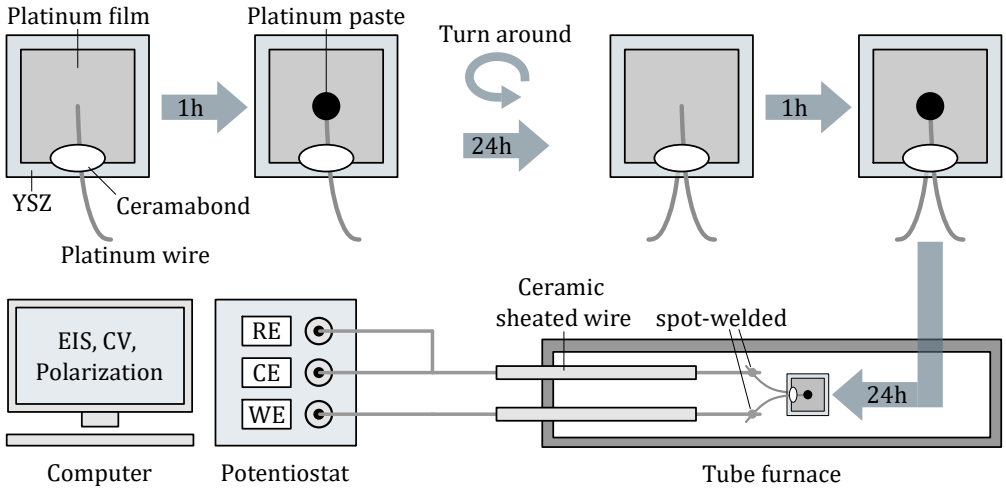

Figure 4.4: Preparation and two-electrode setup for electrochemical measurements. The two platinum electrodes were bonded with *Ceramabond*, platinum wire and platinum paste. By spot-welding, wires were mounted in a tube furnace, which is connected to a potentiostat.

4.2.2 Electrochemical Impedance Spectroscopy (EIS)

Electrochemical impedance spectroscopy (EIS) is used to investigate processes within an electrochemical system. By applying a sinusoidal alternating voltage $U_{AC}(\omega)$ and measuring the resulting current $I_{AC}(\omega)$, the frequency-dependent impedance $Z(\omega)$ can be determined (see Equation 4.3). In general, different frequencies ω are applied to trigger various electronic or ionic processes.

$$Z(\omega) = \frac{U_{AC}(\omega)}{I_{AC}(\omega)} \tag{4.3}$$

$$C = (Q \cdot R^{1-\alpha})^{\frac{1}{\alpha}} \tag{4.4}$$

There are two common methods for representing impedance data. The first is the Bode plot, in which the impedance Z or the phase angle φ is plotted as a function of frequency. The second method is the Nyquist plot, in which imaginary part and real part of impedance are plotted on x and y axis. Based on the Nyquist plot, an equivalent circuit can be modeled that describes the system by (several) circuit parts. Each part stands for a specific process within the electrochemical system. Table 4.1 lists all circuit parts used in this work, including the underlying equation for the impedance Z. Apart from pure ohmic resistance R, all circuit parts have an imaginary part and depend on the frequency ω. The constant phase element (CPE) is a special circuit part. It allows more flexibility in fitting and can be seen as something in between a resistor and a capacitor. The corresponding Q and α values, however, have no physical meaning, but they can be used for determining the capacitance C (see Equation (4.4)). More information on electrochemical impedance spectroscopy can be found in a review article by Lzanas and Prodromidis[90].

Table 4.1: Circuit parts that were used in this work to model electrochemical systems.

Ohmic resistance *R*	***RL* circuit**	**CPE**	***R*CPE circuit**
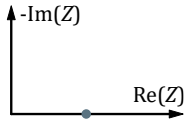	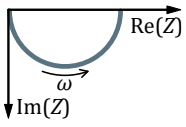	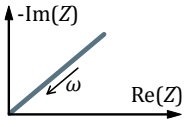	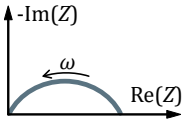
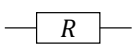	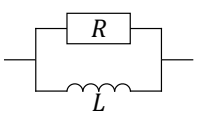		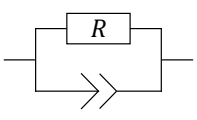
$Z = R$	$Z = \frac{i\omega LR}{R+i\omega L}$	$Z = \frac{1}{Q(i\omega)^{\alpha}}$	$Z = \frac{R}{1+QR(i\omega)^{\alpha}}$

The EIS measurements in this work were performed in a frequency range from 0.1 Hz to 5 MHz. A voltage amplitude of 50 mV was applied. For evaluation, *RelaxIS 3* was used.

4.2.3 Cyclic Voltammetry (CV)

Cyclic voltammetry (CV) is an electrochemical technique for investigating electrode reactions or redox processes. Here, the potential E of a working electrode (vs. CE) is shifted linearly and the resulting current I is recorded. Figure 4.5 (a) shows a typical potential profile like it was applied in this work. The potential is swept anodically or cathodically with a scan rate ν (= dE/dt) until a defined reverse potential E_R is reached. Figure 4.5 (b) illustrates a resulting cyclic voltammogram with two peaks. The peaks are associated with a specific redox process, where the anodic peak corresponds to the oxidation process and the cathodic peak to the respective reduction process.

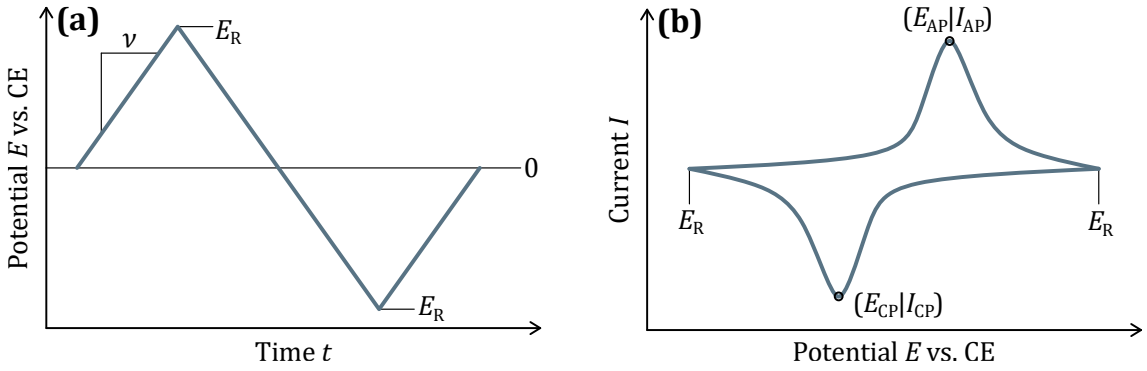

Figure 4.5: Illustration of a cyclic voltammetry measurement with relevant parameters; **(a)** potential profile of the working electrode potential E vs. CE as a function of time with scan rate ν and reverse potential E_R; **(b)** resulting cyclic voltammogram with an anodic (AP) and a cathodic peak (CP).

For higher scan rates ν, higher peak currents I_P are observed. For liquid electrolytes, Randles-Ševčík equation (4.5) claims an $I_P \sim \sqrt{\nu}$ correlation. Besides, an $E_P \sim \ln(\nu)$ correlation holds for irreversible systems (see Equations (4.6) and (4.7)[91]). In this work, the peak values ($E_P|I_P$) illustrated in Figure 4.5 (b) were determined by picking the highest current value and its corresponding potential value from the data set. More insights into cyclic voltammetry can be found in a book by Bard, Faulkner and White[92].

$$I_P = 0.4463\, nFAc\sqrt{\frac{nF\nu D}{RT}} \tag{4.5}$$

$$E_{\mathrm{AP}} = E^0 + \frac{RT}{(1-\alpha)nF}\ln\left(\frac{(1-\alpha)nF\nu}{RTk}\right) \tag{4.6}$$

$$E_{\mathrm{CP}} = E^0 - \frac{RT}{\alpha nF}\ln\left(\frac{\alpha nF\nu}{RTk}\right) \tag{4.7}$$

4.2.4 Potentiostatic Polarization

In potentiostatic polarization experiments, a constant potential (= E_{POL}) is applied to the working electrode (vs. CE) and the resulting current I is recorded. Figure 4.6 illustrates a typical I versus t curve obtained in this work. During polarization, the current decreases with time and drops to zero after polarization time t_{POL} is reached. The decrease of current is ascribed to diffusive limitations of redox species that are transported towards the working electrode. According to Cottrell equation (4.8), the current is expected to follow an $I \sim 1/\sqrt{t}$ dependence. However, it should be noted that this correlation is derived for liquid electrolytes and is therefore not valid for solid electrolytes.

$$I = \frac{nFAc\sqrt{D}}{\sqrt{\pi t}} \tag{4.8}$$

$$Q = \int_{t_0}^{t_1} I(t)\,\mathrm{d}t \tag{4.9}$$

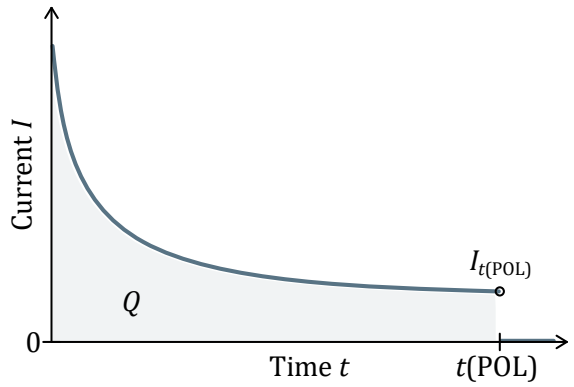

Figure 4.6: Illustration of a typical I versus t curve obtained by applying a constant potential E to the WE (vs. CE) for a polarization time t(POL). Q represents the area beneath the curve, and $I_{t(\mathrm{POL})}$ represents the current value before current drops to zero.

For evaluation of potentiostatic polarization experiments, two quantities were determined. First, the area beneath the I versus t curves was determined (see Figure 4.6). Due to Equation (4.9) this area corresponds to the moved or converted charge Q and was calculated by *OriginPro 2023b*. Second, the last current value $I_{\mathrm{t(POL)}}$ before the current drops to zero was determined by picking it from the data set.

5 Preparation of Pt and CeO_{2-x} Films

This chapter deals with the fabrication and characterization of platinum (Pt) and cerium oxide (CeO_{2-x}) films. For that, preparation by pulsed laser deposition (PLD) is considered a suitable method. Here, the fabrication of dense[93–95] and de-wetted[63,96] platinum films on polished YSZ(111) substrates are well documented in literature. However, since the YSZ substrates employed in this work were only polished on one side, the fabrication of platinum films on the unpolished side had to be investigated (Chapter 5.1). These films were supposed to work as counter electrodes in the pumping system which is why the preparation of dense and electrically conductive films was necessary. Beyond that, the fabrication of cerium oxide films is investigated in this chapter. Also for cerium oxide films, preparation by PLD is a common method[97–100]. In this work, dense cerium oxide films with a (111) preferential orientation were pursued (see Chapter 3.3). For that, the deposition was primarily tested on the polished side of the YSZ(111) substrate (Chapter 5.2). Based on this, Chapter 5.3 shows the deposition of cerium oxide films deposited on Pt(111) films that were deposited on the polished side of YSZ(111) beforehand (see Figure 5.1). All films were characterized by scanning electron microscopy (SEM) and X-ray diffraction (XRD).

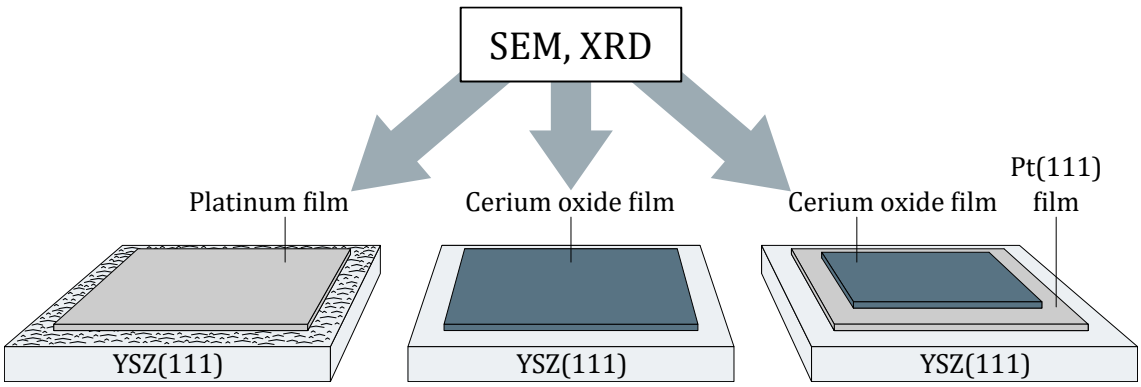

Figure 5.1: Illustration of Chapter 5. Platinum films were grown on the unpolished side of the YSZ(111) substrate and cerium oxide films were grown on the polished side of the YSZ(111) substrate as well as on Pt(111) films. All films were fabricated by pulsed laser deposition (PLD) and characterized by scanning electron microscopy (SEM) and X-ray diffraction (XRD).

5.1 Preparation of Pt Films on Unpolished YSZ(111)

Platinum deposition on the unpolished side of the YSZ(111) substrate by PLD was carried out in argon atmosphere (p = 2 Pa) with a pulse energy of 400 mJ and a pulse frequency of 6 Hz. The temperature of the heater was set to 700 °C. These parameters were taken from a work by Beck et al.[93]. 7,200 pulses were emitted.

The electrical conductivity of the platinum film was examined by a multimeter. The two pins were pressed onto the film with around seven millimeters distance. Resistance values in the single digit Ω range were obtained, making the film suitable for the application as counter electrode in the intended pumping system (see Chapter 3.3). The SEM images in Figure 5.2 show a dense, but inhomogeneous platinum film with fragments of various sizes. In XRD analysis, reflexes at 30.1°, 39.9° and 62.5° were found, which could be attributed to YSZ(111), Pt(111) and YSZ(222)[93] (see Figure 5.3). The reflexes at 27.2°, 28.8°, 55.9° and 59.6° are not discussed, but they did not appear for respective Pt depositions on the polished YSZ(111) side (cf. Figure 11.1).

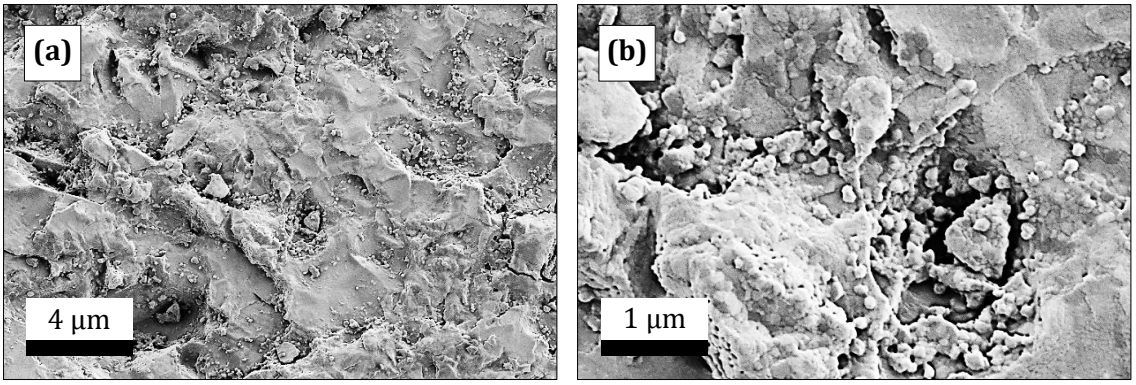

Figure 5.2: SEM images of a platinum film deposited on the unpolished YSZ(111) substrate side; **(a)** overview image showing a dense film; **(b)** more detailed image with fragments of different sizes.

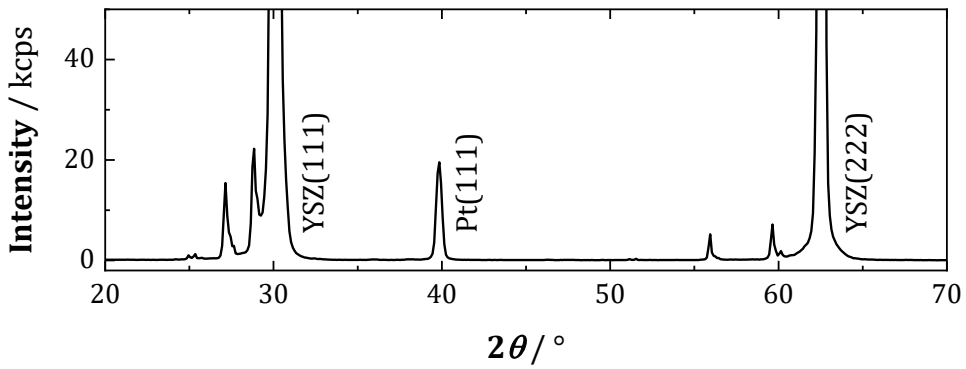

Figure 5.3: XRD pattern of a platinum film deposited on the unpolished YSZ(111) substrate side. Reflexes are attributed to YSZ(111), Pt(111) and YSZ(222).

5.2 Preparation of CeO_{2-x} Films on YSZ(111)

The preparation of cerium oxide films was tested on the polished YSZ(111) substrate side. The films were prepared by PLD with a pulse energy of 300 mJ and a pulse frequency of 10 Hz. The depositions were carried out in an oxygen atmosphere (p = 2 Pa). The temperature of the heater was set to 300 °C. 36,000 pulses were emitted. These parameters were derived from a work by Balakrishnan et al.[98].

The so-prepared cerium oxide film had a film thickness of around 4 µm and a dark blue color. The color could indicate that the film was reduced or nonstoichiometric to a certain extent[16]. A more detailed spectroscopic investigation of this can be found in Chapter 6. Images taken by SEM show a dense film with grains of various sizes (see Figure 5.4). The cerium oxide film grew epitaxially since reflexes at 28.3° and 58.5° could be attributed to CeO_{2-x}(111) and CeO_{2-x}(222)[98].

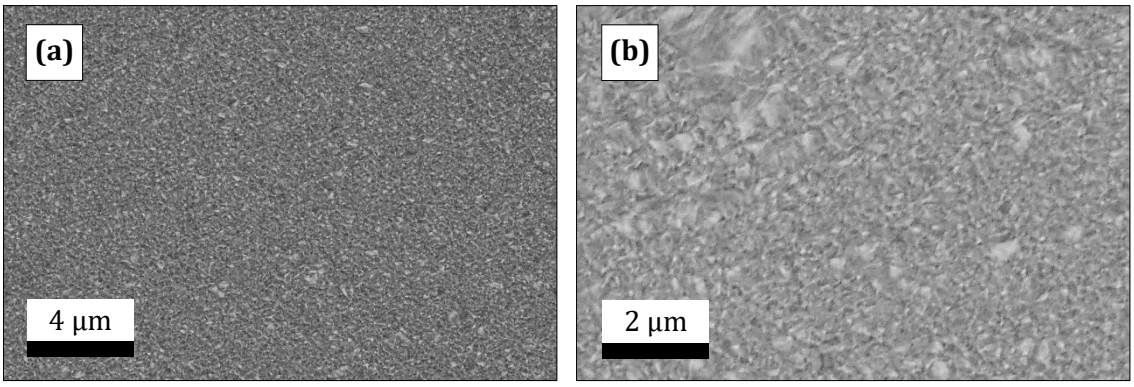

Figure 5.4: SEM images of a cerium oxide film deposited on the polished side of the YSZ(111) substrate; **(a)** overview image showing a dense film; **(b)** more detailed image showing grains of various sizes.

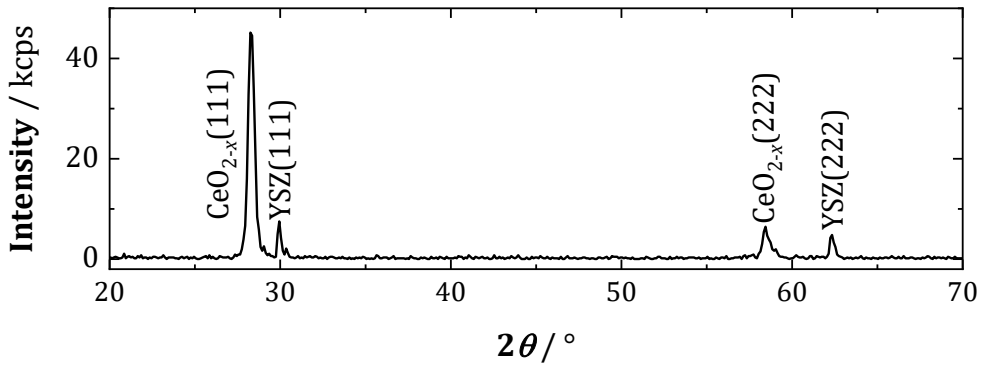

Figure 5.5: XRD pattern of a cerium oxide film deposited on the polished YSZ(111) substrate side. Reflexes are attributed to CeO_{2-x}(111), YSZ(111), CeO_{2-x}(222) and YSZ(222).

Deposition in argon atmosphere

The deposition of cerium oxide films on the polished side of the YSZ(111) substrate was also tested with argon as background gas. Apart from that change, the same parameters were used as described above (E = 300 mJ, f = 10 Hz, N = 36,000, p(Ar) = 2 Pa, $\vartheta_{\text{Heater}}$ = 300 °C).

The resulting film also had a thickness of around 4 µm and a deep blue color. However, SEM images reveal significant differences since the cerium oxide film deposited in argon atmosphere shows cracks (see Figure 5.6). The corresponding results of XRD analysis can be found in the Appendix (Figure 11.2).

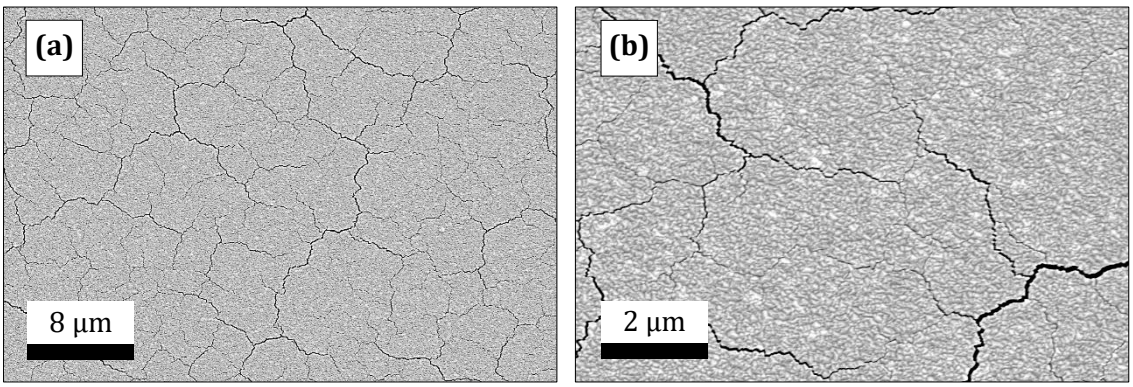

Figure 5.6: SEM images of a cerium oxide film deposited on the polished side of the YSZ(111) substrate; the deposition was performed with argon as background gas; **(a)** overview image revealing cracks within the film; **(b)** more detailed image of the cracks.

5.3 Preparation of CeO_{2-x} Films on Pt(111)/YSZ(111)

Based on the results from Chapter 5.2, cerium oxide films were deposited on a Pt(111) film, which was deposited on the polished YSZ(111) substrate side beforehand (E = 400 mJ, f = 6 Hz, p(Ar) = 2 Pa, $\vartheta_{\text{Heater}}$ = 700 °C, N = 7,200[93]). For the subsequent preparation of a cerium oxide film, a pulse energy of 300 mJ, a pulse frequency of 10 Hz and a heater temperature of 300 °C were used. Oxygen was used as background gas ($p(O_2)$ = 2 Pa) and 36,000 pulses were emitted.[98]

Figure 5.7 shows SEM images of the resulting cerium oxide film that are comparable to the images taken for the cerium oxide film deposited on YSZ(111) (cf. Figure 5.4). Figure 5.8 shows the XRD pattern of the CeO_{2-x}/Pt/YSZ system. In addition to the reflexes that are ascribed to Pt(111) (2θ = 39.8°), YSZ(111) (2θ = 30.0°) and YSZ(222) (2θ = 62.4°)[93], a

further reflex at 28.3° was attributed to CeO_{2-x}(111)[98]. Accordingly, an epitaxial growth of the cerium oxide film on the Pt(111) film was obtained.

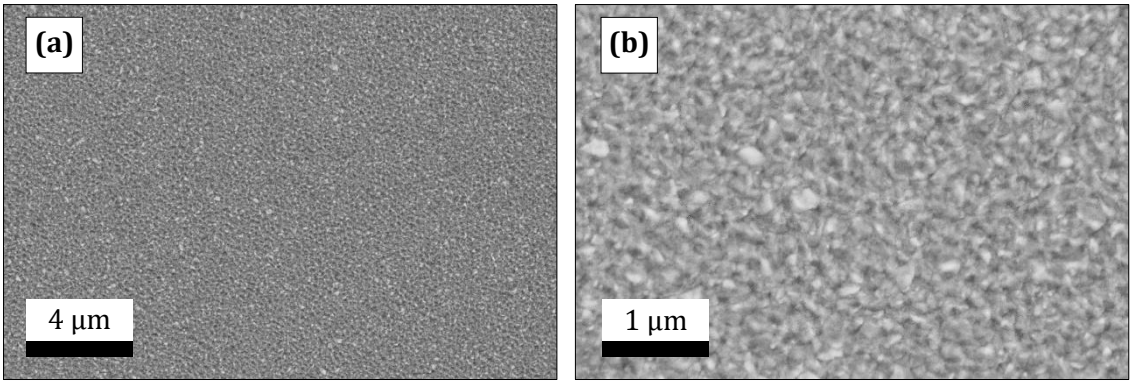

Figure 5.7: SEM images of a cerium oxide film deposited on a Pt(111) film, which was deposited on the polished YSZ(111) substrate side beforehand; **(a)** overview image showing a dense film; **(b)** more detailed image showing grains.

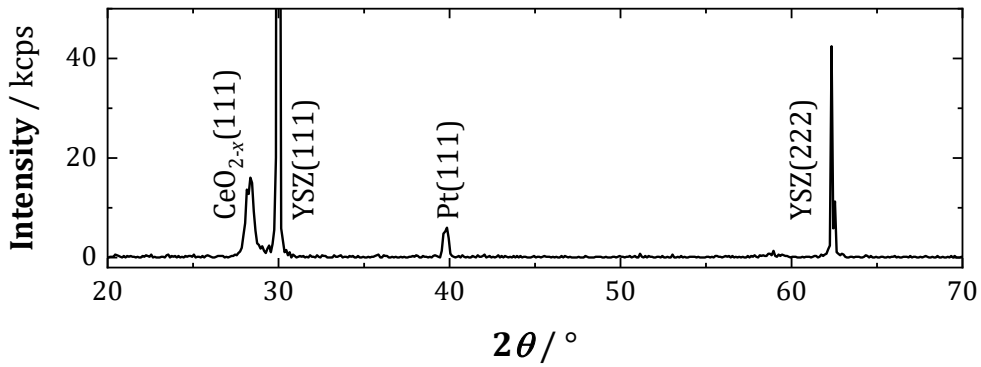

Figure 5.8: XRD pattern of a cerium oxide film deposited on a Pt(111) film, which was deposited on the polished side of YSZ(111) substrate beforehand. Reflexes are attributed to CeO_{2-x}(111), YSZ(111), Pt(111) and YSZ(222).

Regarding the intended pumping system (see Chapter 3.3), the successful preparation of dense cerium oxide films with (111) preferential orientation on dense platinum thin films represents an important intermediate result. Based on this, cerium oxide films were grown on de-wetted platinum thin films in a further step (see Chapter 8.1).

6 Spectroscopy on CeO_{2-x} Films

Raman spectroscopy (RS)[22] and X-ray photoelectron spectroscopy (XPS)[19–21] are suitable methods to investigate the oxidation state of cerium oxide (CeO_{2-x}). Accordingly, they were applied on the cerium oxide films fabricated by pulsed laser deposition (see Chapter 5). It was assumed that these films were partially reduced due to dark blue color[16] after deposition on yttria-stabilized zirconia. RS and XPS measurements were additionally performed after an annealing step in air. It was assumed that annealing in air would lead to an incorporation of oxygen into cerium oxide[26]. Thereby, spectra with different amount of oxygen vacancies could be analyzed. In addition, due to corresponding penetration depth, Raman spectroscopy gave information about bulk defects, whereas XPS provided information about the surface. The measurements were carried out on cerium oxide films deposited on YSZ(111) as well as on Pt(111)/YSZ(111). A brief description of preparation is given in Chapter 6.1. The results of the spectroscopic measurements are then presented in Chapters 6.2 and 6.3.

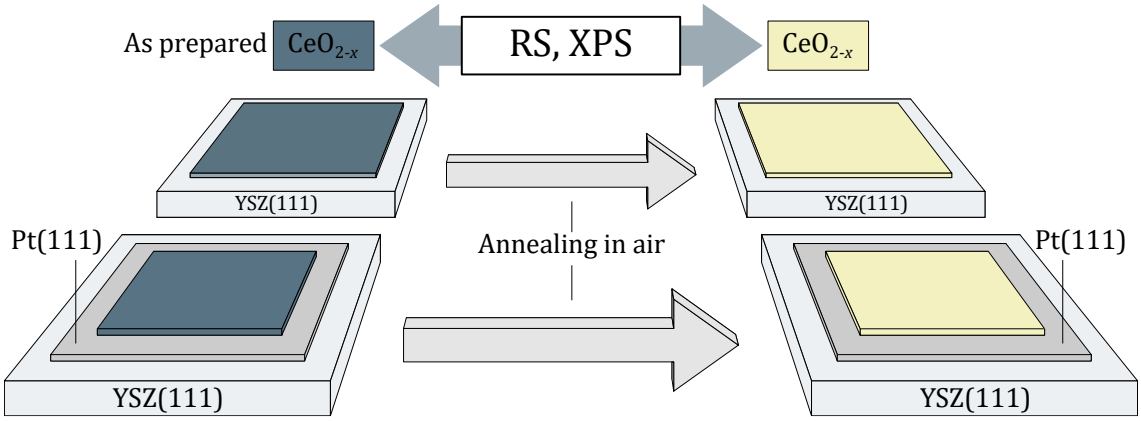

Figure 6.1: Illustration of Chapter 6. Cerium oxide films were grown by pulsed laser deposition on YSZ(111) and on a Pt(111) thin film. After preparation, films were investigated by Raman spectroscopy (RS) and by X-ray photoelectron spectroscopy (XPS). After annealing in air, measurements were repeated. It was assumed that oxygen is incorporated into cerium oxide in the annealing step.

6.1 Preparation of CeO_{2-x} Films

The cerium oxide films were prepared by PLD with a pulse energy of 300 mJ, a pulse frequency of 10 Hz and a heater temperature of 300 °C. Oxygen was used as background gas (p = 2 Pa).[98] The number of pulses was 18,000. These parameters led to films with a thickness of around 150 nm. The deviating film thickness compared to Chapter 5 is described in Chapter 4.1.1. The cerium oxide films were deposited on YSZ(111) and on Pt(111)/YSZ(111) as illustrated by Figure 6.1. The polished side was deposited, respectively. The intermediate Pt(111) film was also prepared by PLD[93] (E = 400 mJ, f = 6 Hz, $\vartheta_{\mathrm{Heater}}$ = 700 °C, p(Ar) = 2 Pa, N = 7,200). The thickness of the Pt(111) film was around 130 nm. After the initial Raman and XPS measurements were carried out, the samples were annealed in air ($p(O_2) \approx 0.2$ atm) at 600 °C for 12 hours. After that, measurements were repeated.

6.2 Raman Spectroscopy on CeO_{2-x} Films

This chapter presents the results of Raman measurements on cerium oxide films deposited on YSZ(111) as well as on Pt(111)/YSZ(111). Since the results differ significantly, this chapter is divided into two subchapters.

Raman spectroscopy on CeO_{2-x}/YSZ(111)

Figure 6.2 (a) shows the Raman spectra for a cerium oxide film grown on YSZ(111) after preparation via PLD (black graph) and after annealing in air (blue graph). Several modes were observed, which were assigned to the underlying YSZ substrate as a reference spectrum of a pure YSZ substrate shows (grey graph). The only mode that did not occur for pure YSZ is the characteristic F_{2g} mode of CeO_2 caused by the symmetric breathing vibration of the oxygen ion sublattice[22]. Regarding Figure (b), the position of the F_{2g} peak shifts through annealing. As prepared, the position of this peak was found at around 460 cm^{-1}. After heat treatment, the F_{2g} mode was located at 463 cm^{-1}. This shift to higher wave numbers can be explained by oxidation of the cerium oxide film[101]. In addition to the peak shift, a change in peak width was observed. As prepared, the full width at half maximum (FWHM) of the F_{2g} mode was 25 cm^{-1}. After annealing in air, however, the FWHM was only 15 cm^{-1}. This effect is ascribed to growing crystallites. The correlation between crystallite size within cerium oxide films and peak width is also shown in a publication by Suzuki et al.[102]. Here, they presented a linear behavior between half width and the inverse of the grain size.

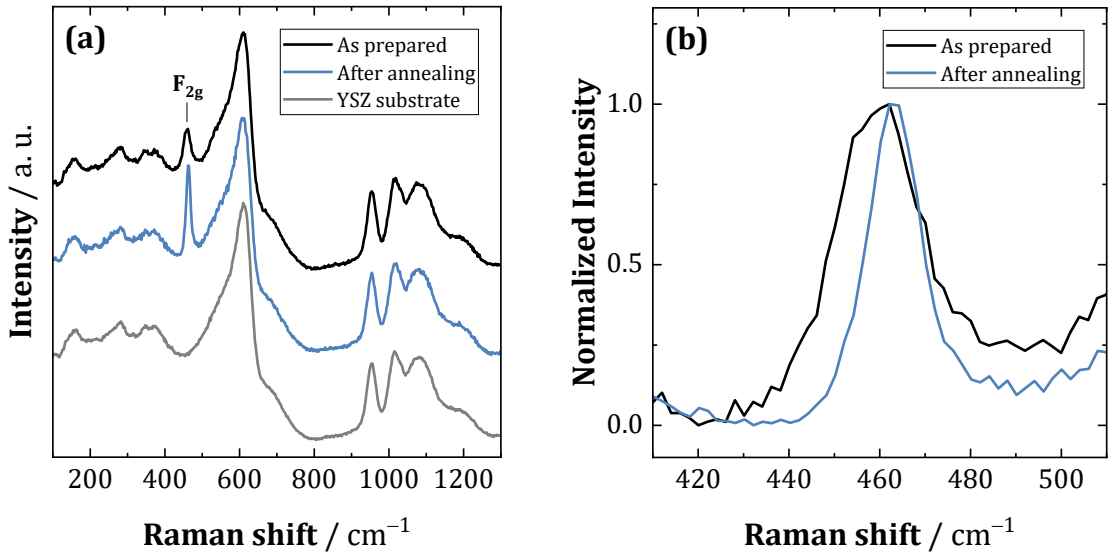

Figure 6.2: Raman spectra of a cerium oxide film deposited on the polished side of YSZ(111) substrate after preparation via pulsed laser deposition (black) and after annealing in air (blue); **(a)** overview spectra compared with a reference spectrum of the YSZ substrate (grey); **(b)** normalized F_{2g} mode of cerium oxide.

Raman spectroscopy on CeO_{2-x}/Pt(111)/YSZ(111)

This subchapter presents the obtained Raman spectra for the CeO_{2-x}/Pt(111)/YSZ(111) system after preparation by PLD and after annealing in air (see Figure 6.3). The respective Raman spectra differ significantly from that of the CeO_{2-x}/YSZ(111) system since there are no peaks that could be attributed to YSZ. Presumably, this is caused by the high reflectivity of the intermediate platinum film. Indeed, no YSZ peak was obtained when the laser spot is focused on the platinum film. Figure 6.3 clearly shows the characteristic F_{2g} mode[22] in both cases at around 463 cm^{-1} meaning that no significant shift due to the heat treatment occurred. This contrasts with the cerium oxide film deposited on YSZ. However, the FWHM decreased through annealing (21 cm^{-1} to 16 cm^{-1}) that is, again, attributed to crystallite growth[102]. Regarding (b), another difference caused by annealing can be noticed. Before heat treatment, additional modes at around 542 cm^{-1} and 592 cm^{-1} were observed. After heat treatment, these modes are hardly noticeable or absent. Comparable spectra containing these modes can be found in literature for Gd-doped[103–107] or Sm-doped[104,106,107] cerium oxide samples. There are also publications that found defect modes at 560 cm^{-1} [108] and at 592 cm^{-1} [109] for pure nonstoichiometric cerium oxide. Overall, these modes can be attributed to the presence of oxygen vacancies. Therefore, annealing led to a decrease of oxygen vacancies and accordingly to an oxidation of the cerium oxide film. Since these modes nearly disappeared, cerium oxide is considered fully oxidized or stoichiometric. The Raman spectrum of the cerium oxide target employed for PLD can be found in the Appendix.

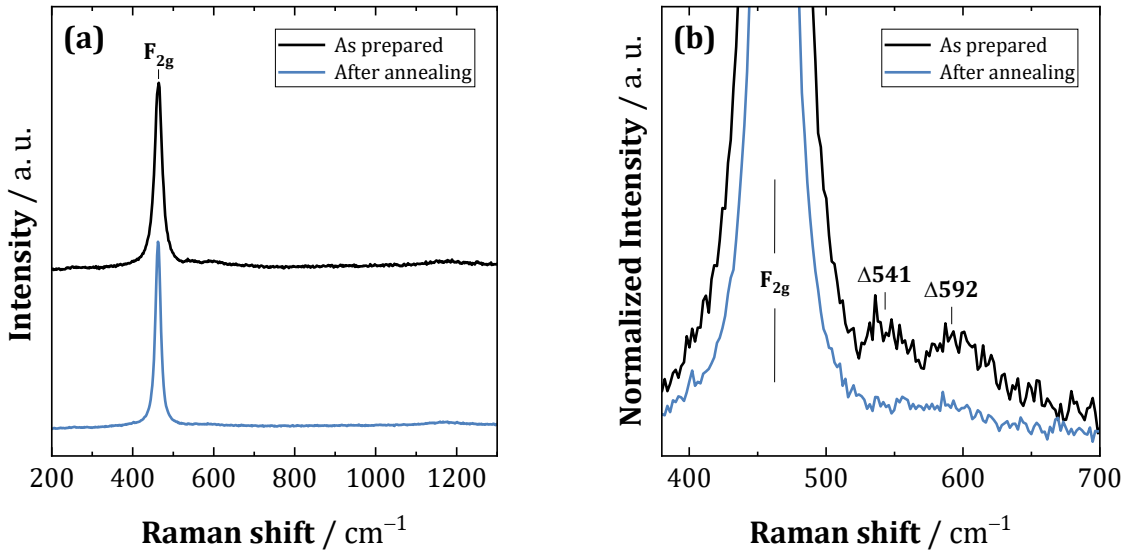

Figure 6.3: Raman spectra of a cerium oxide film deposited on Pt(111)/YSZ(111) after preparation via pulsed laser deposition (black) and after annealing in air (blue); **(a)** overview spectra; **(b)** normalized F_{2g} mode of cerium oxide with defect modes at 541 cm^{-1} and 592 cm^{-1} after preparation that nearly disappeared after annealing.

The Raman results presented here are particularly important for the interpretation of electrochemical data obtained for the CeO_{2-x}/Pt/YSZ/Pt system (see Chapter 8). Based on the presented Raman data, it can be concluded that stochiometric CeO_2 is present during electrochemical characterization, which was conducted at elevated temperatures in air.

6.3 X-ray Photoelectron Spectroscopy on CeO_{2-x} Films

Like Raman spectroscopy, X-ray photoelectron spectroscopy (XPS) is another method that can be used to investigate the oxidation state of cerium oxide. XPS has an information depth of a few nanometers and is therefore significantly more surface-sensitive than Raman spectroscopy. Figure 6.4 shows the XP spectra for the respective cerium oxide films after preparation and after annealing in air for both cerium oxide systems. Regarding (a), the Ce 3d spectra are quite similar before and after annealing. Six main peaks indicate a high Ce^{4+} concentration[21]. Before heating, slight shoulders at around 885 eV and 903 eV were observed, which are attributed to a slight nonstoichiometry or reduction of the cerium oxide surface[110]. However, after the annealing step, the cerium oxide surface is considered fully oxidized due to disappearance of these shoulders.

Figure (b) shows the corresponding O 1s XP spectra. For both the CeO_{2-x}/Pt/YSZ and the CeO_{2-x}/YSZ system the same trend was observed, *i.e.*, a slight shift of the O 1s peak towards lower binding energy due to annealing in air. It shifted from 529.4 eV to 529.2 eV, respectively. The origin of that shift might be caused by an oxidation effect. In a work by Mullins et al.[21], the O 1s position is claimed to be 530.4 eV for CeO_2 and 530.7 eV for $CeO_{1.5}$. Besides, there are further studies that investigated the O 1s peak when cerium metal is exposed to oxygen[9,111]. Also here, a shift to lower binding energies is given during oxidation. However, literature is not consistent in terms of O 1s shifting and the respective role of oxygen vacancies in this regard[112]. The corresponding Ce 4d XP spectra can be found in the Appendix.

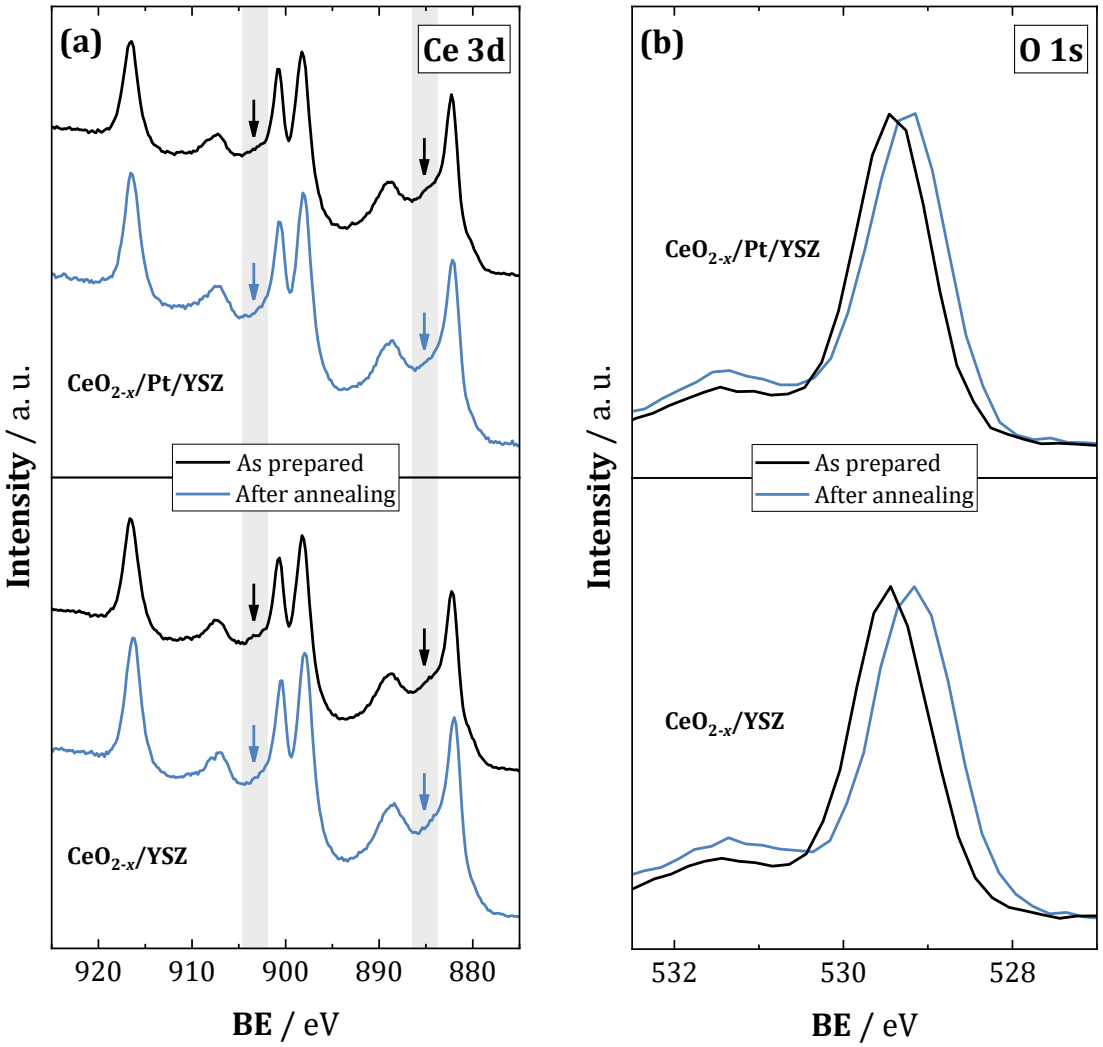

Figure 6.4: XP spectra of cerium oxide films after preparation via pulsed laser deposition (black) and after annealing in air (blue); **(a)** Ce 3d XP spectra of a CeO_{2-x} film deposited on a Pt(111) film (top) and Ce 3d XP spectra of a CeO_{2-x} film deposited on a YSZ(111) substrate (bottom); **(b)** O 1s XP spectra of a CeO_{2-x} film deposited on a Pt(111) film (top) and O 1s XP spectra of a CeO_{2-x} film deposited on a YSZ(111) substrate (bottom).

7 Characterization of Pt/YSZ/Pt Cells

The pursued pumping system is based on a Pt/YSZ/Pt cell (see Chapter 3.3). This chapter presents the preparation and electrochemical characterization of this underlying cell type. Therefore, a de-wetted platinum film electrode is deposited on one side of the YSZ substrate. On the backside, a dense platinum film electrode is deposited. For characterization, electrochemical impedance spectroscopy (EIS) was applied. It was investigated how de-wetted structure affects the impedance. For that, the EIS results were compared with those of another Pt/YSZ/Pt cell that has two dense platinum film electrodes (see Figure 7.1). EIS measurements were performed at different temperatures to make conclusions about YSZ activation energies and about the electrode process, *i.e.*, oxygen incorporation and removal occurring at the triple phase boundary O_2/Pt/YSZ. In Chapter 7.1, the preparation of respective Pt/YSZ/Pt cells by PLD is shown. Results of EIS measurements are then presented in Chapters 7.2 and 7.3. The cells were first annealed at 600 °C in air (Chapter 7.2) and then characterized in the temperature range from 300 °C to 600 °C (Chapter 7.3).

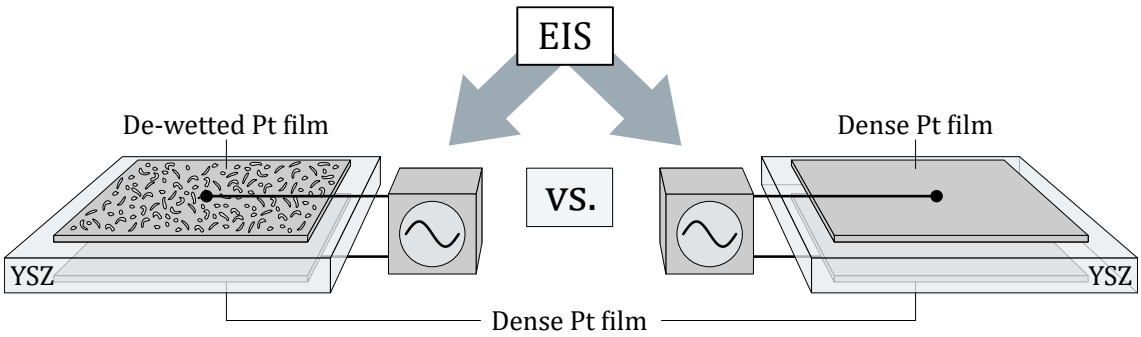

Figure 7.1: Illustration of Chapter 7. Two different Pt/YSZ/Pt cells were prepared by pulsed laser deposition. One cell consists of one de-wetted and one dense platinum thin film electrode (left). The other cell consists of two dense platinum thin film electrodes (right). Both systems were characterized by electrochemical impedance spectroscopy (EIS) to reveal differences caused by the de-wetted structure.

7.1 Preparation of Pt/YSZ/Pt Cells

For preparation of Pt/YSZ/Pt cells, platinum films were first deposited on the polished side of the YSZ(111) substrate. For preparation of a dense platinum film on polished YSZ, the same parameters[93] were used like for the deposition on unpolished YSZ (see Chapter 5.1). The resulting film had a thickness of around 161 nm and showed a Pt(111) preferential orientation. For preparation of a de-wetted platinum film on polished YSZ, a heater temperature of 800 °C and a pulse frequency of 2 Hz were applied. The deposition took place in argon atmosphere (p = 1 Pa) and 14,400 pulses with a pulse energy of 400 mJ were emitted. These parameters were derived from a publication by Pöpke et al.[63] and led to a film thickness of around 34 nm. After platinum depositions were carried out on the polished side of the YSZ substrate, respective platinum depositions were performed on the unpolished side. Again, the same PLD parameters[93] as described in Chapter 5.1 were used for preparation of dense films. All platinum depositions were performed centered with an area of 8 mm × 8 mm on the 10 mm × 10 mm YSZ substrate (see Figure 7.2).

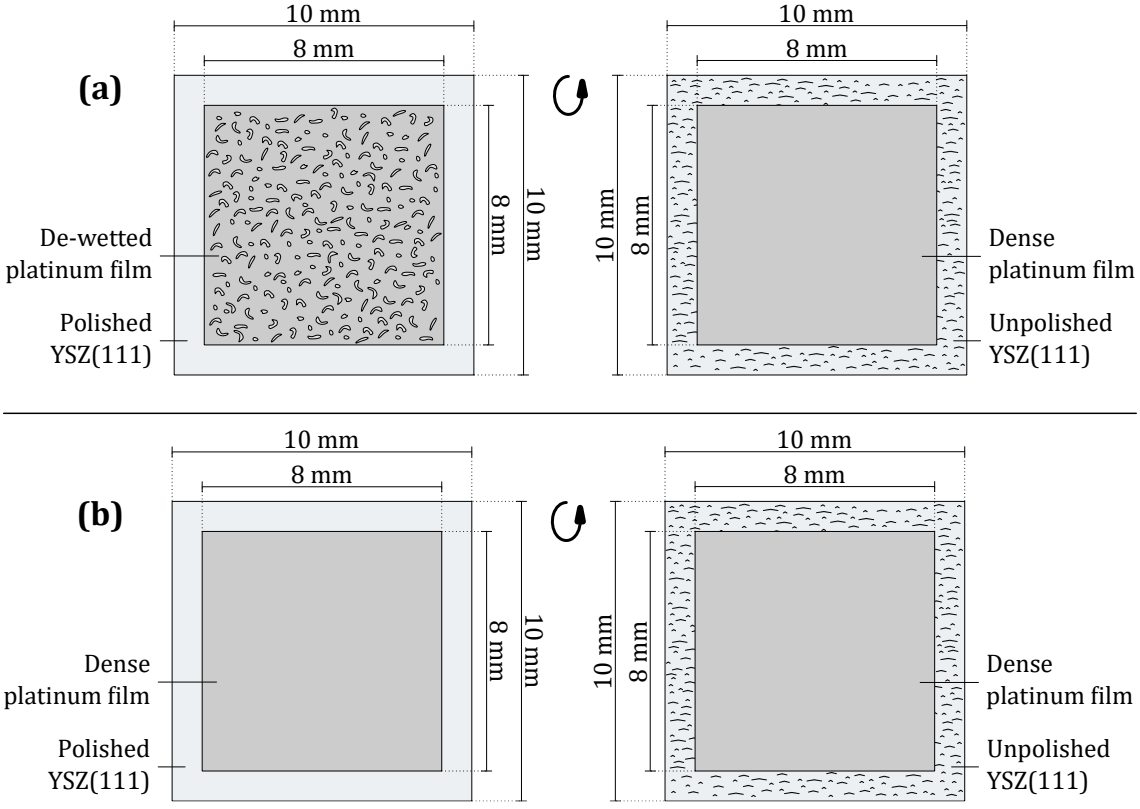

Figure 7.2: Geometries of deposited platinum thin films on the polished (left) and on the unpolished side (right) of the YSZ(111) substrate; films were prepared by pulsed laser deposition; **(a)** Pt/YSZ/Pt cell with one de-wetted and one dense platinum film; **(b)** Pt/YSZ/Pt cell with two dense platinum films.

Characterization of de-wetted platinum film

Figure 7.3 shows SEM images of the de-wetted platinum thin film. The trenches reveal different forms and a width of approximately 100 nm. Despite de-wetted structure, electrical conductivity could be confirmed by multimeter. The two pins were pressed onto the film with around seven millimeters distance and resistance values in the range of 10 Ω were obtained. The de-wetted platinum film exhibited a (111) preferential orientation[93] as indicated by the reflex at 39.8° in the XRD pattern (see Figure 7.4).

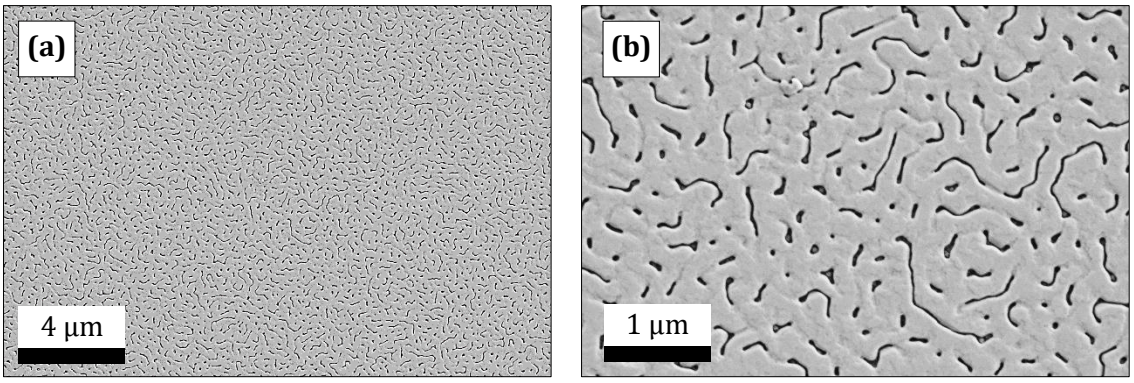

Figure 7.3: SEM images of a de-wetted platinum film that was grown on the polished side of a YSZ(111) substrate; **(a)** overview image; **(b)** more detailed image with trenches of different forms.

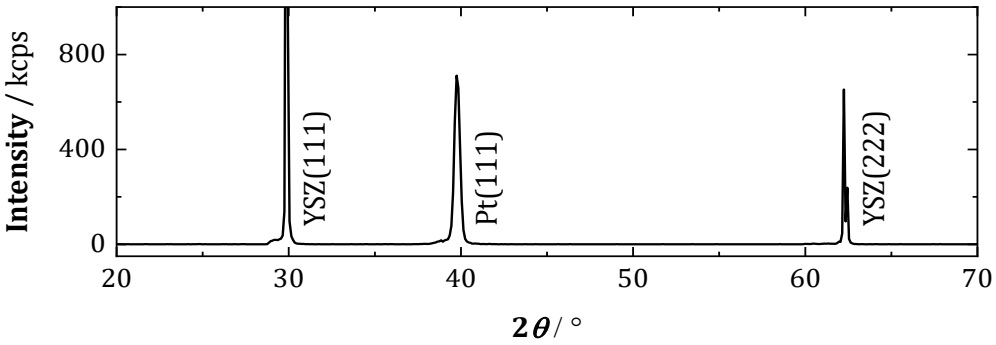

Figure 7.4: XRD pattern of a de-wetted platinum film that was grown on the polished side of a YSZ(111) substrate. Reflexes are attributed to YSZ(111), Pt(111) and YSZ(222).

7.2 EIS Measurements during Annealing

The Pt/YSZ/Pt cells (see Chapter 7.1) were first annealed in air (ϑ = 600 °C, t = 12 h, p(air)= 1 atm). During annealing, EIS measurements were performed to monitor changes. Figure 7.5 shows the resulting Nyquist plots for the two Pt/YSZ/Pt cell types. Here, part (a) shows the low-frequency range and part (b) the high-frequency range. For quantitative evaluation, a *R*-*RL*-*R*CPE equivalent circuit was applied for the sample with one de-wetted film, and a *R*-*RL*-CPE circuit was used for the cell with two dense films (see also Table 7.1).

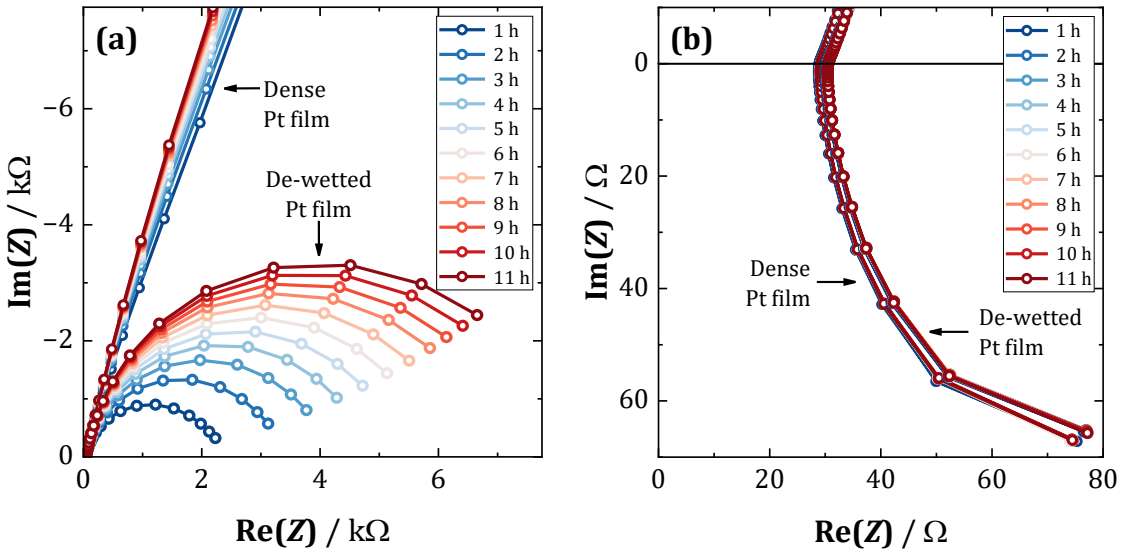

Figure 7.5: Nyquist plots for a Pt/YSZ/Pt cell with one de-wetted Pt film and one dense Pt film as well as Nyquist plots for a Pt/YSZ/Pt cell with two dense Pt films during annealing in air (ϑ = 600 °C, t = 12 h, p(air) = 1 atm); time represents the dwell time at 600 °C; **(a)** low-frequency range; **(b)** high-frequency range.

Discussion of low-frequency range

Regarding Figure 7.5 (a), Nyquist plots differ significantly in the low-frequency range. While the Pt/YSZ/Pt cell with de-wetted Pt film resulted in clearly visible semicircles, the Pt/YSZ/Pt cell with dense Pt film led to a straight line instead. This can be explained by the electrode process taking place, *i.e.*, the incorporation and removal of oxygen at the triple phase boundary (TPB) O_2/Pt/YSZ (see Chapter 3.1). Since the TPB of de-wetted platinum film is orders of magnitude longer in comparison to the dense platinum film, much more oxygen can be incorporated or removed. For that process, a semicircle (R_{EP}CPE) is obtained whose resistance (= R_{EP}) is regarded as resistance for the electrode process or the oxygen exchange reaction. In case of dense platinum film, oxygen accumulates at the dense platinum electrode since it cannot be exchanged. In the Nyquist plot, this blocking behavior results in a straight line and is therefore modelled with a constant phase element (CPE). The corresponding Q and α values of R_{EP}CPE and CPE can be found in the Appendix.

As indicated by Figure 7.5 (a), the diameter of the semicircle or the resistance R_{EP} increased with dwell time at 600 °C. This increase is proportional to $\sqrt{t}$ as shown in Figure 7.6 (a). This behavior was, *e.g.*, also observed by Pöpke et al.[63] where it was ascribed to the formation of platinum oxides. Platinum oxides inhibit the oxygen exchange reaction, leading to an increase of the corresponding resistance (see also Chapter 3.1).

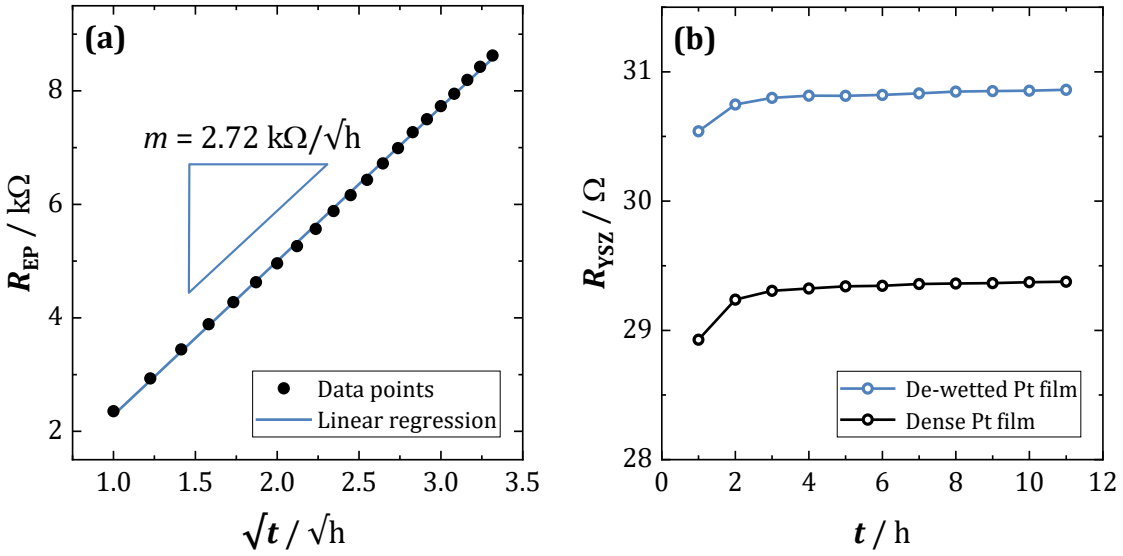

Figure 7.6: **(a)** Plot of electrode process resistance R_{EP} versus square root of dwell time $\sqrt{t}$ at 600 °C for the Pt/YSZ/Pt cell with one de-wetted and one dense Pt thin film (p(air) = 1 atm); **(b)** plot of YSZ bulk resistance R_{YSZ} versus dwell time at 600 °C for the Pt/YSZ/Pt cell with one de-wetted and one dense thin Pt film as well as for the Pt/YSZ/Pt cell with two dense Pt thin films.

Discussion of high-frequency range

In the high-frequency range, the Nyquist plots of the two Pt/YSZ/Pt cells are similar (see Figure 7.5 (b)). On the real axis an offset was obtained, which was modelled as a resistance R attributed to the YSZ bulk resistance (= R_{YSZ}). An inductive semicircle also occurred, which was included in the equivalent circuit diagram as parallel $R_L L$ element. However, R_L and L values will not be further discussed as it was assumed that they arose from the setup.

Regarding Figure 7.6 (b), R_{YSZ} values for de-wetted Pt/YSZ/Pt cell are slightly higher in comparison to those for the dense Pt/YSZ/Pt cell. This issue could be caused by a smaller electrode area due to de-wetted structure. By *ImageJ*, a de-wetted area of around 7% was calculated. That means that the electrode area A of the de-wetted film is only 93% of the area of the dense film ($A_{\text{de-wetted}}/A_{\text{dense}}$ = 0.93). By considering $R \sim 1/A$, a slightly higher resistance is therefore reasonable. Indeed, the corresponding ratio of resistances (= $R_{\text{dense}}/R_{\text{de-wetted}}$) would underline this assumption as it is 0.95 in average. Beyond that, both curves show the same trend as they first increase slightly and then remain constant.

7.3 EIS Measurements at Different Temperatures

In this chapter, the results of temperature-dependent EIS measurements are presented (p(air) = 1 atm). The Pt/YSZ/Pt cells (see Chapter 7.1) were characterized in 25 °C steps from 300 °C to 600 °C. Representative Nyquist plots for different temperature ranges are shown in Figure 7.7. In the high-frequency range (a), the two cell types do not differ in their general form. In the temperature range from 300 °C to 475 °C, a semicircle occurred in both cases, which was modelled by a *R*CPE parallel circuit, respectively (see Table 7.1). Here, corresponding *R* values were attributed to the bulk resistance of YSZ (= R_{YSZ}). From 525 °C to 600 °C, there is a single resistance (= R_{YSZ}) and an inductive semicircle (= $R_L L$) as it was also obtained during annealing at 600 °C (see Chapter 7.2). The measurement at 500 °C could not be modelled appropriately. In the low-frequency range (b), both Pt/YSZ/Pt cells exhibit blocking behavior for the temperature range from 300 °C to 475 °C. This behavior remains the same for the cell with two dense platinum films in the temperature range from 525 °C to 600 °C. For the cell with the de-wetted platinum film, however, a semicircle appears from 525 °C on, which is modelled as parallel *R*CPE element, representing the electrode process occurring at the triple phase boundary O_2/Pt/YSZ. The equivalent circuits applied for quantification are summarized for the respective temperature range in Table 7.1.

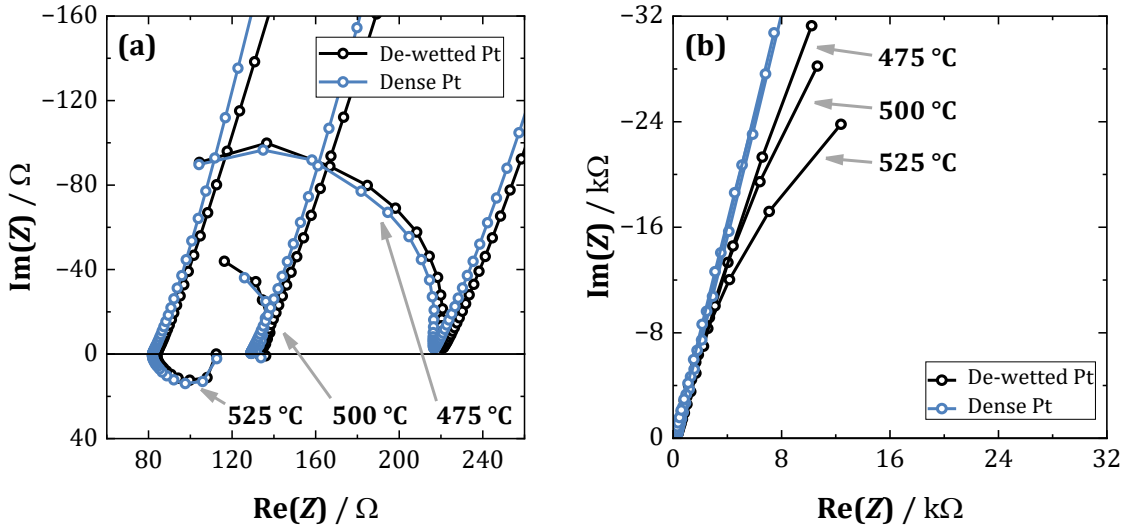

Figure 7.7: Nyquist plots for a Pt/YSZ/Pt cell with one de-wetted Pt film and one dense Pt film (black) as well as Nyquist plots for a Pt/YSZ/Pt cell with two dense Pt films (blue) for various temperatures (p(air) = 1 atm); **(a)** high-frequency range; **(b)** low-frequency range.

Table 7.1: Overview of equivalent circuits used for respective Pt/YSZ/Pt cells at various temperature ranges.

	ϑ = 300 °C to 475 °C	ϑ = 525 °C to 600 °C
Dense Pt /YSZ/ Dense Pt	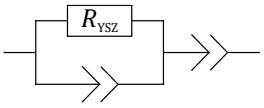	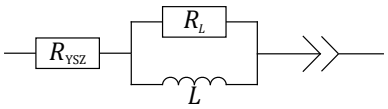
De-wetted Pt /YSZ/ Dense Pt		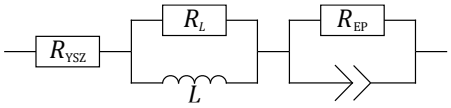

Activation energies of oxygen bulk transport in YSZ

For the two Pt/YSZ/Pt cells the same temperature dependence for YSZ bulk resistance (= R_{YSZ}) was observed. This can be demonstrated by a respective $\ln(\sigma_{YSZ}T)$ versus $1/T$ plot (see Figure 7.8). Here, a bending in the data points was found which is why no single linear regression was performed. Instead, three different regressions are presented showing the general trend of decreasing activation energy E_A with increasing temperature. Indeed, this bending is often reported in literature[30,32,113–115] and frequently ascribed to mobile and immobile oxygen vacancies. The immobile oxygen vacancies are trapped in defect complexes[34] like $(Y'_{Zr}V_O^{\bullet\bullet})^{\bullet}$ and $(Y'_{Zr}V_O^{\bullet\bullet}\,Y'_{Zr})^{X}$ and do not contribute to ionic conduction. With increasing temperature, however, these complexes decay, resulting in more mobile vacancies.

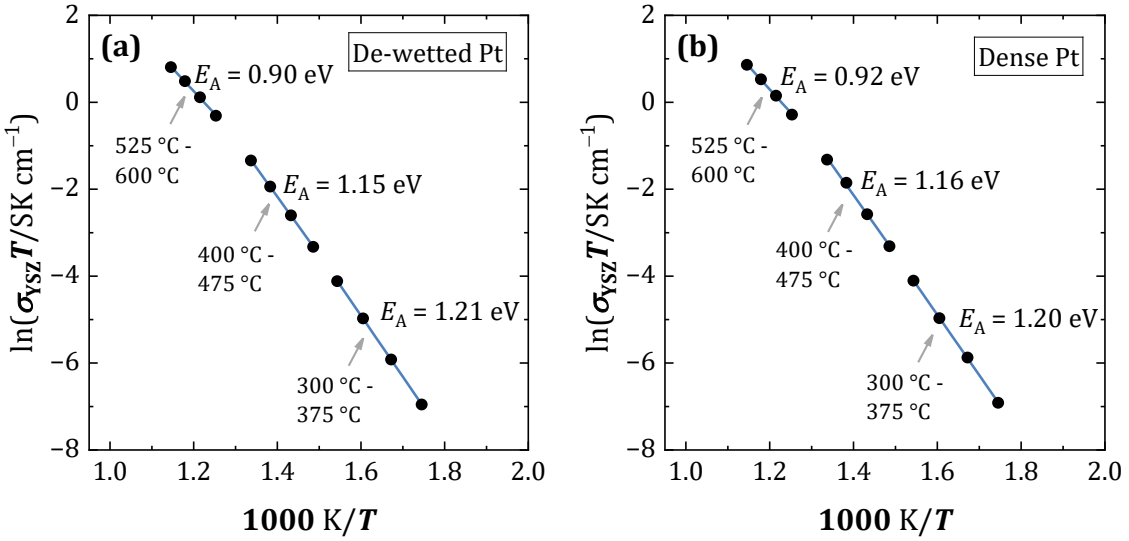

Figure 7.8: Logarithmic plot of $\sigma_{YSZ}T$ versus T^{-1} and calculated values for activation energies E_A for three different temperature ranges; **(a)** data for the Pt/YSZ/Pt cell with one de-wetted and one dense Pt thin film; **(b)** data for the Pt/YSZ/Pt cell with two dense Pt thin films.

Temperature dependence of the electrode process

In the temperature range from 525 °C to 600 °C the electrode process, *i.e.*, oxygen incorporation and removal at the O_2/Pt/YSZ triple phase boundary, can be modelled by a parallel R_{EP}CPE circuit (see Table 7.1). For evaluating the R_{EP} values in greater detail, EIS measurements were performed in 10 °C steps from 530 °C to 600 °C. The corresponding Nyquist plots (see Figure 7.9 (a)) show a decreasing semicircle diameter with increasing temperature. A plot of the corresponding R_{EP} values is given in Figure (b), providing a clear illustration of the temperature dependence of the oxygen exchange reaction. The Q and α values associated with the R_{EP}CPE circuit as well as the high-frequency parts of Figure 7.9 (a) can be found in the Appendix.

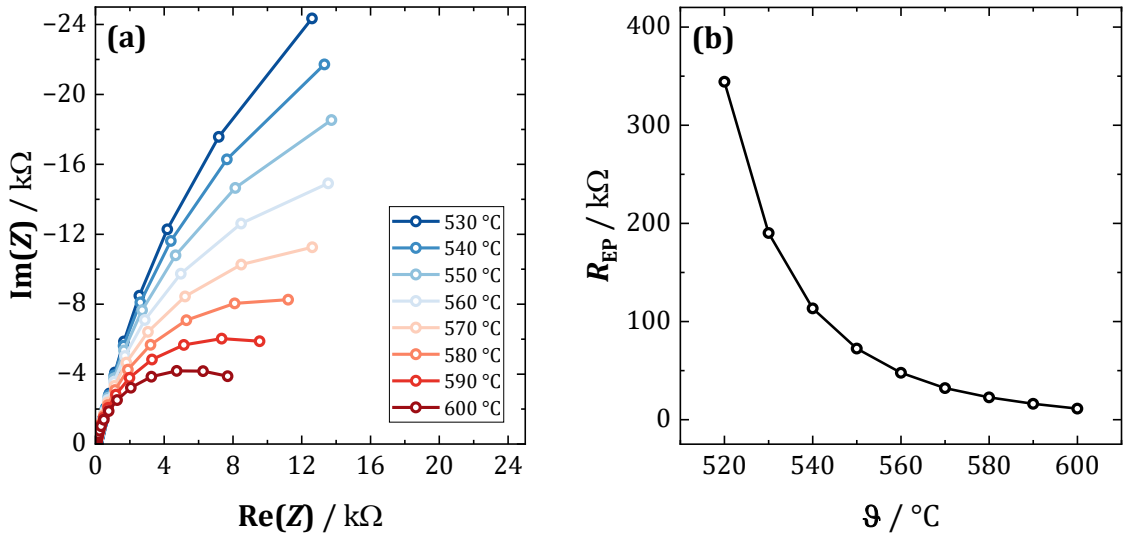

Figure 7.9: Temperature dependence of the electrode process resistance R_{EP} of the Pt/YSZ/Pt cell with one de-wetted Pt thin film and one dense Pt thin film (p(air) = 1 atm); **(a)** low-frequency range of Nyquist plots for various temperatures; the corresponding high-frequency parts are presented in the Appendix; **(b)** plot of calculated R_{EP} values versus temperature. Lines are drawn between data points to indicate the trend.

8 Electrochemistry on CeO_{2-x}/Pt/YSZ/Pt

In this chapter, the preparation and electrochemical characterization of a CeO_{2-x}/Pt/YSZ/Pt system is shown, representing a prototype for the intended pumping system (see Chapter 3.3). For that, a Pt/YSZ/Pt system with one de-wetted Pt film was prepared and extended with a cerium oxide film (see Figure 8.1). Preparation as well as SEM and XRD characterization are presented in Chapter 8.1. The main part of this chapter, however, is the electrochemical characterization of this system since the oxidation state of cerium oxide must be controlled by applying electric potentials. Therefore, electrochemical impedance spectroscopy (EIS) (Chapter 8.2) and cyclic voltammetry (CV) (Chapter 8.3) were applied to investigate at first whether influences were found, which could be ascribed to the cerium oxide film. Thus, respective EIS and CV measurements were compared with a reference system without cerium oxide (see Chapter 7). Additionally, potentiostatic polarization measurements were conducted to gain information about the currents at anodic and cathodic polarization (Chapter 8.4). All electrochemical measurements were performed in air and at various temperatures (p(air) = 1 atm, ϑ = 300 °C to 600 °C).

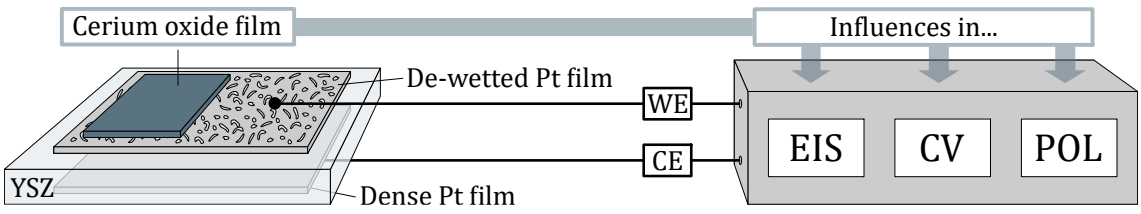

Figure 8.1: Illustration of Chapter 8. An electrochemical CeO_{2-x}/Pt/YSZ/Pt system was prepared by pulsed laser deposition that serves as a prototype for the intended pumping system. To investigate whether the cerium oxide film is electrochemically integrated in the system, impedance spectroscopy (EIS), cyclic voltammetry (CV) and potentiostatic polarization (POL) experiments were performed to find influences caused by the cerium oxide film.

8.1 Preparation of a CeO_{2-x}/Pt/YSZ/Pt System

For preparation of a CeO_{2-x}/Pt/YSZ/Pt system by PLD, a Pt/YSZ/Pt cell was prepared as described in Chapter 7.1. Thus, a de-wetted platinum film was grown on the polished side of the YSZ(111) substrate in a first step. The same parameters as depicted in Chapter 7.1 were used, except for the number of pulses, which were 21,600. As shown in Figure 8.2, the de-wetted platinum film was deposited centered with an area of 8 mm × 8 mm (Ø film thickness = 41 nm). After that, a dense platinum film was deposited on the backside of the YSZ(111) substrate, also centered with an area of 8 mm × 8 mm. For that, the same parameters as depicted in Chapter 5.1 were used. Finally, a cerium oxide film was deposited on the de-wetted platinum film with the same parameters as presented in Chapter 5.3. The area of the cerium oxide film was 3 mm × 6 mm. As shown in Figure 8.2, the cerium oxide film was not deposited centered but with 1 mm distance to the respective edges of the platinum film on the left side. This geometry was chosen to have sufficient free area for bonding with platinum paste, platinum wire and *Ceramabond*.

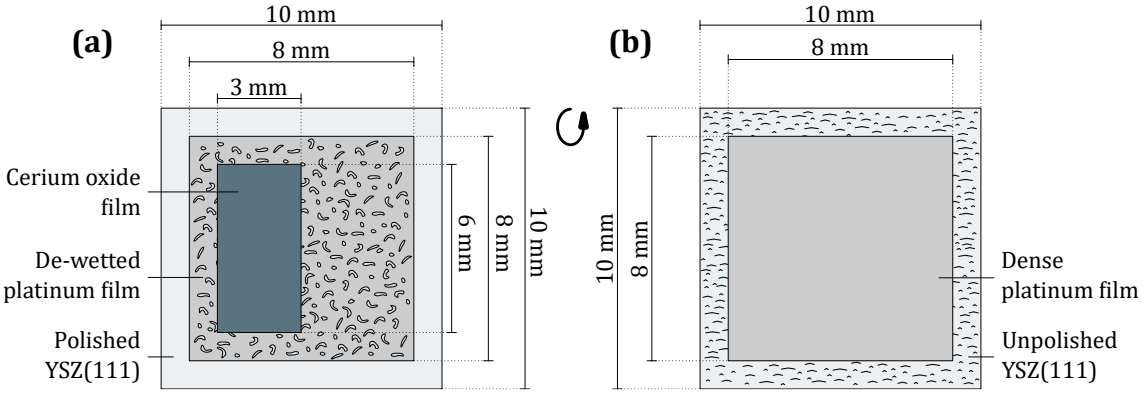

Figure 8.2: Geometries of the prepared CeO_{2-x}/Pt/YSZ/Pt system; films were prepared by pulsed laser deposition; **(a)** a de-wetted platinum was grown on the polished side of the YSZ(111) substrate; on top of this film, a cerium oxide film was deposited; **(b)** a dense platinum film was deposited on the unpolished backside of the YSZ(111) substrate.

Figure 8.3 shows SEM images of the respective films that were taken after final deposition of cerium oxide. Figure part (a) shows the de-wetted platinum thin film deposited on the polished side of the YSZ(111) substrate. In comparison to the de-wetted platinum film shown in Chapter 7 (cf. Figure 7.3), the degree of de-wetting is less for this film, which is probably due to increased number of laser pulses and increased film thickness (41 nm versus 34 nm). Regarding (b), a dense cerium oxide film can be seen, which is comparable to that obtained for deposition on dense platinum (cf. Figure 5.7). For discussion, it is assumed that the cerium oxide film fills the trenches of the de-wetted structure, resulting in a CeO_{2-x}/YSZ interface.

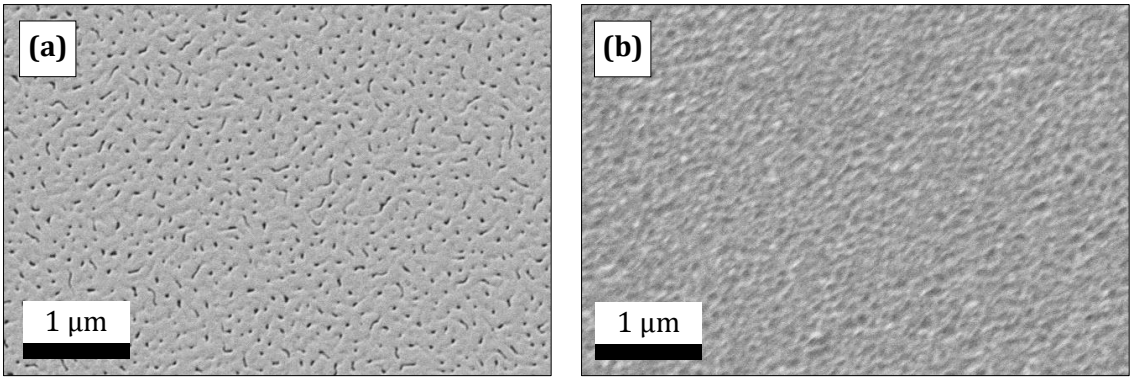

Figure 8.3: SEM images of the films after final deposition of cerium oxide; **(a)** de-wetted platinum thin film deposited on the polished side of the YSZ(111) substrate; **(b)** dense cerium oxide film deposited on the de-wetted platinum thin film.

XRD analysis of the prototype system reveals an epitaxial growth of the cerium oxide film on the de-wetted platinum film (see Figure 8.4). A respective reflex was obtained at 28.4° that is ascribed to a (111) preferential orientation of cerium oxide[98]. The pattern also shows a reflex at 39.9°, which is ascribed to a Pt(111) preferential orientation[93]. The other reflexes are attributed to YSZ(111) (2θ = 29.9°) and YSZ(222) (2θ = 62.5°).

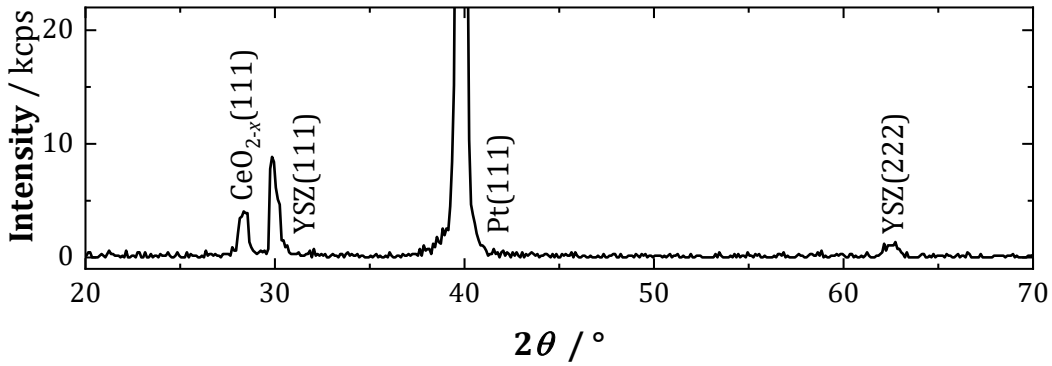

Figure 8.4: XRD pattern of the CeO_{2-x}/Pt/YSZ/Pt system. The reflexes are attributed to CeO_{2-x}(111), YSZ(111), Pt(111) and YSZ(222).

Based on the findings presented in Chapter 5.3, this chapter demonstrates that dense cerium oxide films with a (111) preferential orientation can likewise be grown on de-wetted platinum thin films. This represents a significant intermediate result with respect to the intended application as Deacon catalyst (see Chapters 3.2 and 3.3).

8.2 Impedance Spectroscopy on CeO_{2-x}/Pt/YSZ/Pt

In this chapter, EIS results of the CeO_{2-x}/Pt/YSZ/Pt system are presented and compared with those obtained for the Pt/YSZ/Pt reference system (see Chapter 7). By this, influences caused by the cerium oxide film were found. Like the Pt/YSZ/Pt system, the CeO_{2-x}/Pt/YSZ/Pt system was first annealed in air. Afterwards, it was characterized at various temperatures.

8.2.1 EIS Measurements during Annealing

At first, the CeO_{2-x}/Pt/YSZ/Pt system was annealed in air (ϑ = 600 °C, t = 12 h, p(air) = 1 atm), which was analyzed by EIS. The resulting Nyquist plots (see Figure 8.5 (a)) look quite like those obtained for the annealing process of the Pt/YSZ/Pt reference system (cf. Figure 7.5). However, the corresponding Bode plots (b) show a second peak meaning an additional process compared to the reference system (see black line). The high-frequency range of the CeO_{2-x}/Pt/YSZ/Pt system is comparable to the reference system as a resistive offset and an inductive semicircle occurred (see Figure 11.9 (a) in the Appendix).

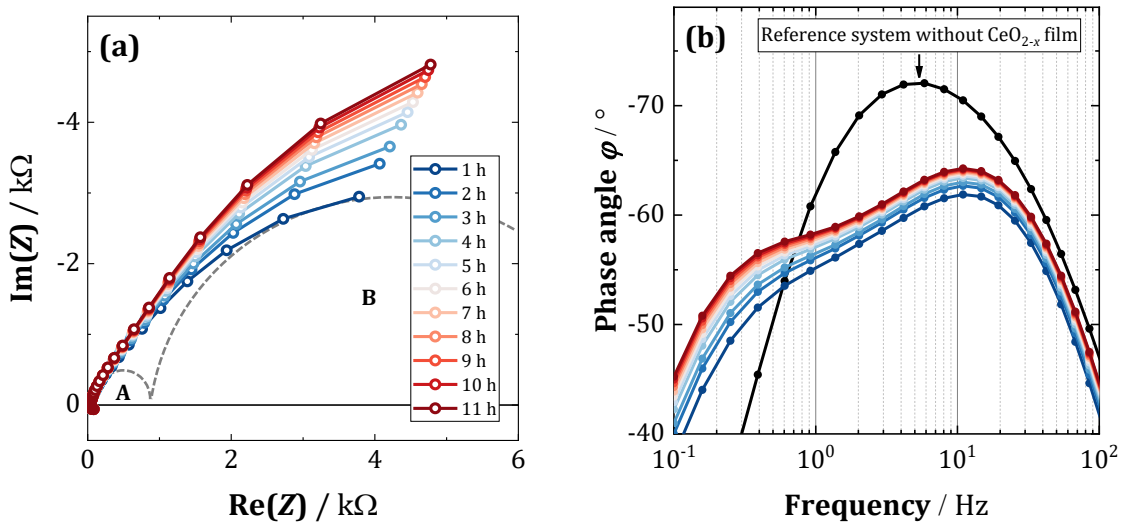

Figure 8.5: EIS measurements conducted during the annealing process of the CeO_{2-x}/Pt/YSZ/Pt system (ϑ = 600 °C, t = 12 h, p(air) = 1 atm); time represents the dwell time at 600 °C; **(a)** Nyquist plots with two schematically drawn semicircles (A) and (B); **(b)** corresponding Bode plots for the low-frequency range indicating two processes (peaks) in comparison to the Pt/YSZ/Pt reference system revealing only one peak (see black data line).

Discussion of two peaks in the low-frequency range

Due to the additional peak, two *R*CPE circuits were used for modelling the low-frequency range of the CeO_{2-x}/Pt/YSZ/Pt system, resulting in a R_1-R_L*L*-R_3CPE-R_4CPE equivalent circuit. Like for the Pt/YSZ/Pt reference system, the resistance R_1 represents the bulk resistance of YSZ (= R_{YSZ}). However, R_{YSZ} values as well as R_L and *L* values are not discussed as they did not differ significantly from the Pt/YSZ/Pt systems. Instead, the two *R*CPE elements are discussed in greater detail.

The semicircle with the bigger diameter (B) is ascribed to the process of oxygen incorporation and removal occurring at the triple phase boundary O_2/Pt/YSZ. This is because the corresponding *R* (= R_{EP}) values show a linear behavior when plotted against $\sqrt{t}$, which was also obtained for the respective process at the Pt/YSZ/Pt reference system (see Figure 8.6). Furthermore, the corresponding slope (m = 2.65 kΩ/√h) is almost the same as for the reference system (m = 2.72 kΩ/√h). Figure 8.6 shows that the resistance values for the CeO_{2-x}/Pt/YSZ/Pt system are bigger in comparison to those of the Pt/YSZ/Pt system. This could be explained by a smaller TPB length as shown by respective SEM images. Beyond that, the cerium oxide film covers around 28% of the de-wetted platinum film. Accordingly, this platinum area has no exposure to oxygen of the atmosphere, meaning that oxygen exchange is possibly suppressed within this area.

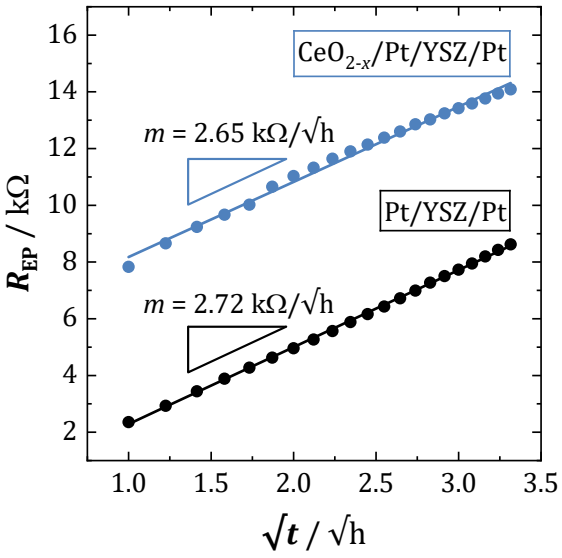

Figure 8.6: Comparison of electrode process resistance R_{EP} values versus square root of dwell time $\sqrt{t}$ at 600 °C for the CeO_{2-x}/Pt/YSZ/Pt system (blue) and for the Pt/YSZ/Pt reference system (black). Electrode process represents the oxygen exchange reaction occurring at the triple phase boundary O_2/Pt/YSZ, respectively.

The second semicircle (A) must be linked to the cerium oxide film as it is the only difference in comparison to the reference system. For description of an additional process occurring in the CeO_{2-x}/Pt/YSZ/Pt system, Figure 8.7 shows schematically the interface of cerium oxide and YSZ. During a negative phase of the sinusoidal voltage signal applied to the de-wetted platinum working electrode, Ce^{4+} ions could be reduced to Ce^{3+} by electrons from the platinum electrode, allowing oxygen ions to migrate across the CeO_{2-x}/YSZ interface and occupy oxygen vacancies within the YSZ electrolyte. In case of a positive potential phase, the reverse process takes place. Here, Ce^{3+} ions are oxidized to Ce^{4+}, allowing the incorporation of oxygen ions into the cerium oxide lattice.

This additional process identified in EIS analysis provides initial evidence for the electrochemical integration of the cerium oxide film into the pumping system and provides therefore a first hint for the intended working principle (see Chapter 3.3).

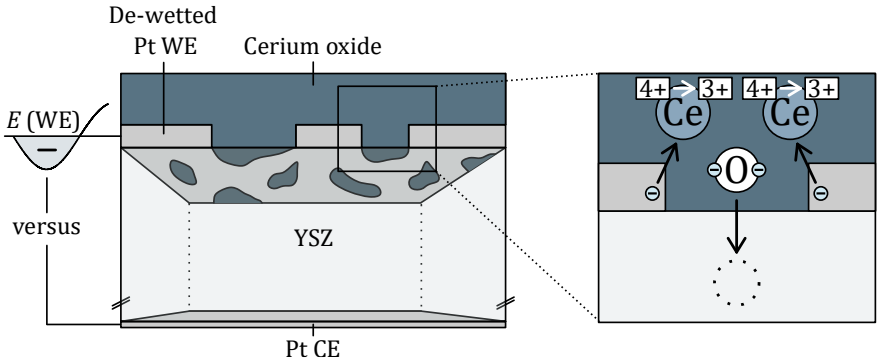

Figure 8.7: Process assumed to occur at the buried de-wetted platinum electrode during EIS measurements. During a negative potential phase, electrons of the platinum working electrode (WE) reduce Ce^{4+} ions to Ce^{3+}, whereby oxygen ions migrate from cerium oxide into YSZ.

Figure 8.8 shows the resistance (= R_{Ce}) and capacitance values (= C_{Ce}) of the as-described Ce^{4+}/Ce^{3+} redox process with increasing dwell time t at 600 °C. Here, the resistance values increase, and the capacitance values decrease. This suggests an inhibition of the process, meaning that less oxygen can be exchanged between cerium oxide and YSZ. An inhibition was also observed for the electrode process occurring at the triple phase boundary of O_2/Pt/YSZ. Here, a linear R_{EP} versus $\sqrt{t}$ correlation was ascribed to the formation of platinum oxides[63]. The formation of platinum oxides at the Pt/YSZ interface might also be a reason for the observed development in Figure 8.8. Indeed, plotting of R_{Ce} versus $\sqrt{t}$ did not yield a linear correlation. However, an appropriate linear behavior is obtained by plotting R_{Ce} versus $1/\sqrt{t}$ instead. The corresponding plot can be found in Figure 11.12 in the Appendix.

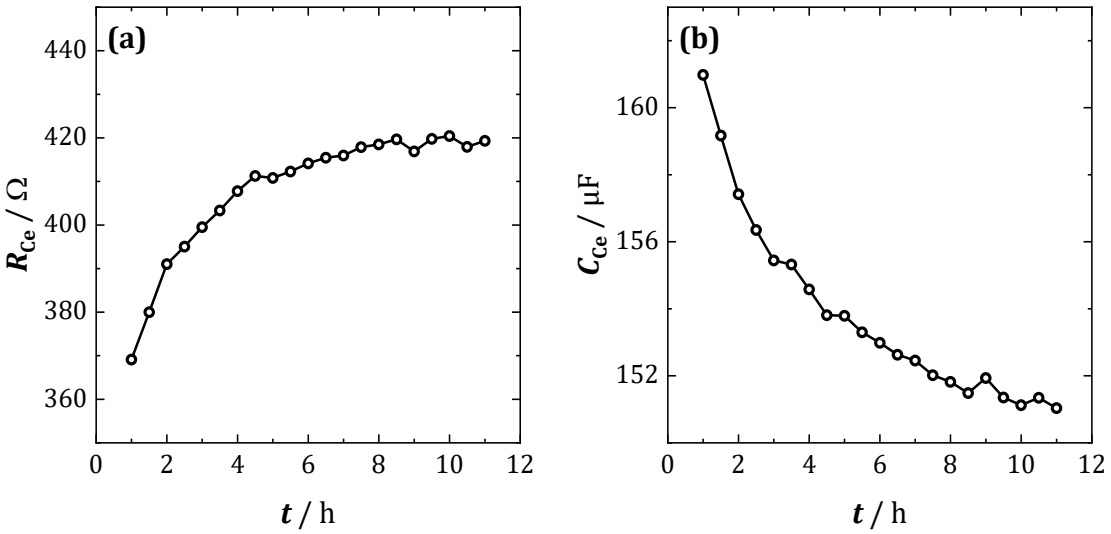

Figure 8.8: Development of parameters corresponding to the process associated with the Ce^{4+}/Ce^{3+} redox process during annealing at 600 °C; the corresponding Q and α values of the R_{Ce}CPE circuit part can be found in the Appendix; **(a)** resistance values R_{Ce} versus dwell time t; **(b)** capacitance values C_{Ce} versus dwell time t. Lines are drawn between data points to indicate the trend, respectively.

8.2.2 EIS Measurements at Different Temperatures

As shown in Chapter 8.2.1, an additional process occurred for the CeO_{2-x}/Pt/YSZ/Pt system at 600 °C. This process was ascribed to the Ce^{4+}/Ce^{3+} redox couple and to the corresponding oxidation or reduction of the cerium oxide film. To further investigate this process or other processes that could be ascribed to the cerium oxide film, EIS measurements were performed in a temperature range from 300 °C to 600 °C (25 °C steps) in air (p = 1 atm). Indeed, from 300 °C to 500 °C no significant differences compared to the reference system were found. However, from 525 °C on, the process related to the Ce^{4+}/Ce^{3+} redox couple was observed. For investigating this process in greater detail, measurements from 550 °C to 600 °C were performed in 5 °C steps. Figure 8.9 shows the resulting Nyquist plots and the corresponding Bode plots. For fitting of presented data, a R_{YSZ}-$R_L$$L$-$R_{Ce}$CPE-$R_{EP}$CPE circuit was used.

As described in Chapter 8.2.1, the semicircle with the bigger diameter (B) is ascribed to the electrode process occurring at the triple phase boundary O_2/Pt/YSZ. The semicircle with smaller diameter (A) is ascribed to the process representing the reduction or oxidation of cerium oxide. Figure 8.10 shows the temperature dependence of respective R_{Ce} and C_{Ce} values. The resistance R_{Ce} decreases with increasing temperature meaning that more oxygen ions could migrate across the CeO_{2-x}/YSZ interface. For capacitance values C_{Ce}, an increase with increasing temperature is obtained. Accordingly, more oxygen ions could be accumulated for this process.

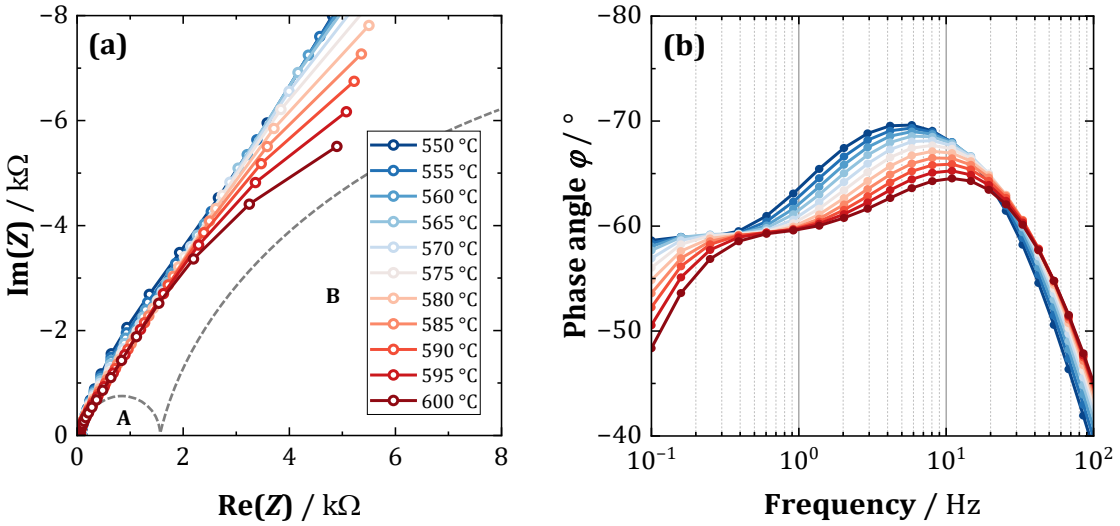

Figure 8.9: EIS measurements of the CeO_{2-x}/Pt/YSZ/Pt system conducted at various temperatures (p(air) = 1 atm); **(a)** Nyquist plots with two schematically drawn semicircles (A) and (B); corresponding high-frequency part is presented in the Appendix; **(b)** corresponding Bode plots for the low-frequency range indicating two processes.

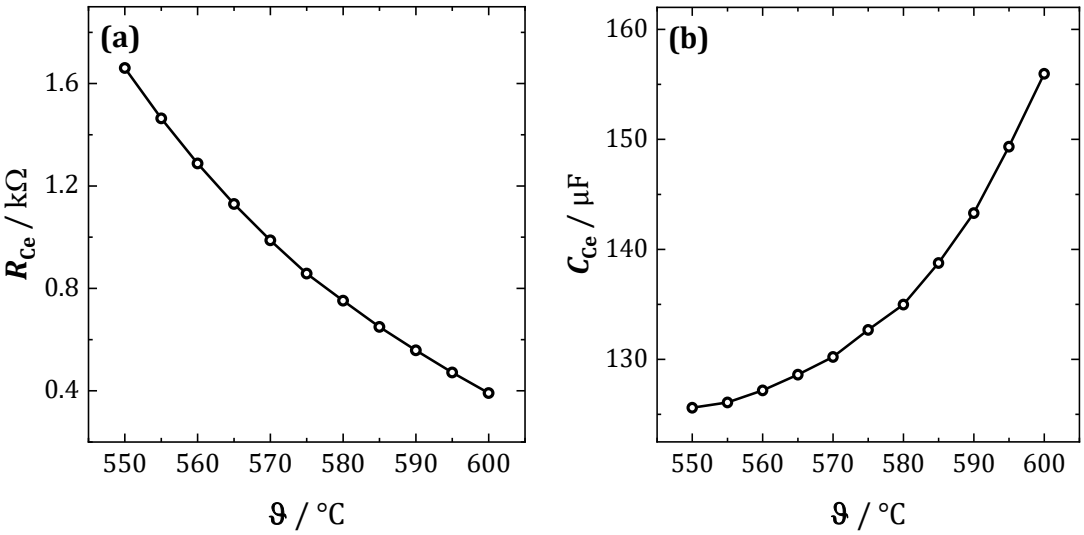

Figure 8.10: Temperature dependence of parameters corresponding to the process associated with the Ce^{4+}/Ce^{3+} redox couple; the corresponding Q and α values can be found in the Appendix; **(a)** temperature dependence of resistance R_{Ce}; **(b)** temperature dependence of capacitance C_{Ce}. Lines are drawn between data points to indicate the trend, respectively.

8.3 Cyclic Voltammetry on CeO_{2-x}/Pt/YSZ/Pt

By performing EIS measurements with the CeO_{2-x}/Pt/YSZ/Pt system, a process was observed, which was attributed to the Ce^{4+}/Ce^{3+} redox couple and the corresponding oxidation or reduction of the cerium oxide film (see Chapter 8.2). In the next step, cyclic voltammetry (CV) was applied to the system to also find influences that are caused by the cerium oxide film. However, in a temperature range from 400 °C to 450 °C, no influence by cerium oxide was observed (see Chapter 8.3.1). Here, the Pt/YSZ system was investigated. From 500 °C on, influences by cerium oxide were observed, which are presented and discussed in Chapter 8.3.2. As illustrated in Figure 8.1, all measurements were carried out with a two-electrode setup with de-wetted platinum film as working electrode (WE) and dense platinum film as counter electrode (CE).

8.3.1 CV Measurements without Cerium Oxide Contribution (400 °C to 450 °C)

At first, reverse potentials E_R were tested to reveal electrochemical processes within the CeO_{2-x}/Pt/YSZ/Pt system. For that, CV measurements were performed with increasing E_R values (ϑ = 400 °C, ν = 20 mV/s, p(air) = 1 atm). Starting with ±0.1 V, the reverse potential was consecutively increased by ±0.1 V as shown in Figure 8.11 (a). By applying a reverse potential of ±0.8 V, one anodic and one cathodic peak were clearly observed. The cathodic peak exhibits a shoulder peak, additionally.

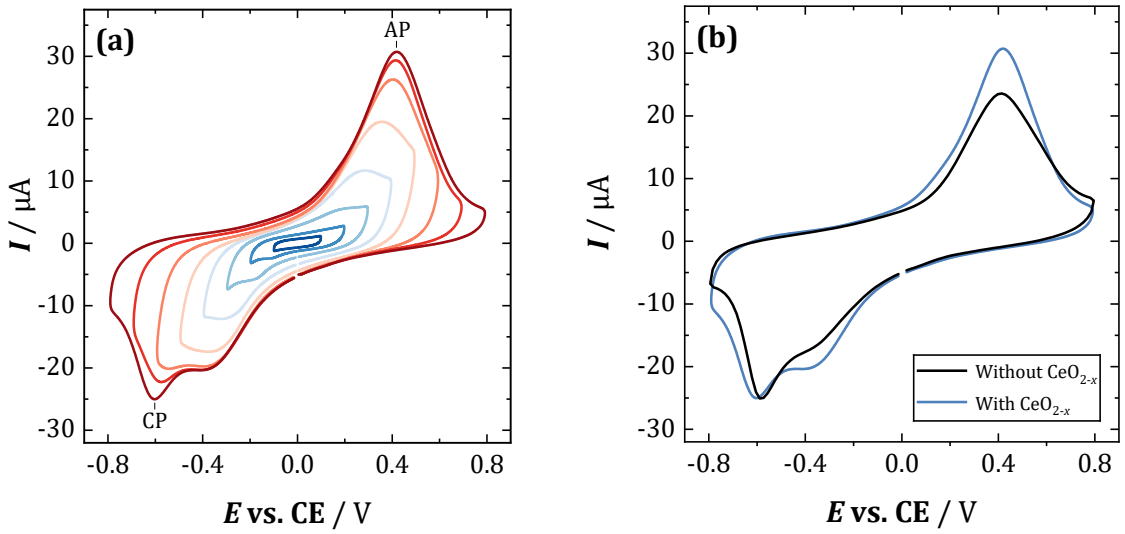

Figure 8.11: **(a)** Cyclic voltammograms obtained for the CeO_{2-x}/Pt/YSZ/Pt system (ϑ = 400 °C, ν = 20 mV/s, p(air) = 1 atm); reverse potentials were increased in ±0.1 V steps; **(b)** comparison of cyclic voltammograms obtained for the CeO_{2-x}/Pt/YSZ/Pt system (blue) and for the Pt/YSZ/Pt reference system without cerium oxide film (black) (ϑ = 400 °C, ν = 20 mV/s, p(air) = 1 atm).

Attribution of peaks appearing

None of the peaks in the cyclic voltammograms are caused by the cerium oxide film since the same peaks were obtained in a respective CV measurement for the Pt/YSZ/Pt system (see Figure 8.11 (b)). According to that, peaks are attributed to charge transfer reactions of the Pt/YSZ electrode system. In literature, these peaks are frequently attributed to the formation of platinum oxides (PtO_x) or to the oxygen exchange reaction occurring at the triple phase boundary (TPB) O_2/Pt/YSZ[55,116–118]. Due to high TPB length of the de-wetted platinum working electrode, the obtained CV peaks were attributed to the oxygen exchange reaction. Thus, the anodic peak represents the oxygen removal from the YSZ lattice, and the cathodic peak represents the oxygen incorporation into the YSZ lattice (see Figure 3.2). The cathodic shoulder peak might occur due to the formation of platinum oxides at the interface of YSZ and the dense Pt counter electrode.

Behavior of peaks at different scan rates and temperatures

To further characterize the peaks attributed to the oxygen exchange reaction, scan rate ν and temperature ϑ were varied. Figure 8.12 shows the resulting cyclic voltammograms obtained for the CeO_{2-x}/Pt/YSZ/Pt system. Here, Figure (a) presents the scan rate dependence at 400 °C, revealing two distinct effects. First, increasing the scan rate led to higher anodic and cathodic peak currents (= I_{AP} and I_{CP}). Second, the corresponding peak potential (= E_P) shifted along the E (vs. CE) axis towards higher absolute values. Varying the temperature also had two effects on the respective voltammograms (see (b)). With increasing temperature, peak currents increased and the corresponding peak potential shifted to lower absolute values.

The trends described can be illustrated by plotting the respective peak points (E_P/I_P). Based on Equations (4.5), (4.6) and (4.7), peak currents were plotted as a function of $\sqrt{\nu}$ and peak potential values were plotted against $\ln(\nu)$. In all cases, linear correlations were obtained as shown in Figure 8.13. Regarding the respective I_P vs. $\sqrt{\nu}$ plots in Figure (a), two additional observations concerning the slopes can be made. First, the absolute slopes m for anodic and cathodic peak current values are quite similar. Second, these slopes increase with temperature. According to Randles-Ševčík equation (4.5), this increase could be attributed to a higher diffusion coefficient D. For the corresponding plots of E_P versus $\ln(\nu)$, a decrease of absolute slope values was observed for higher temperatures (see Figure (b)).

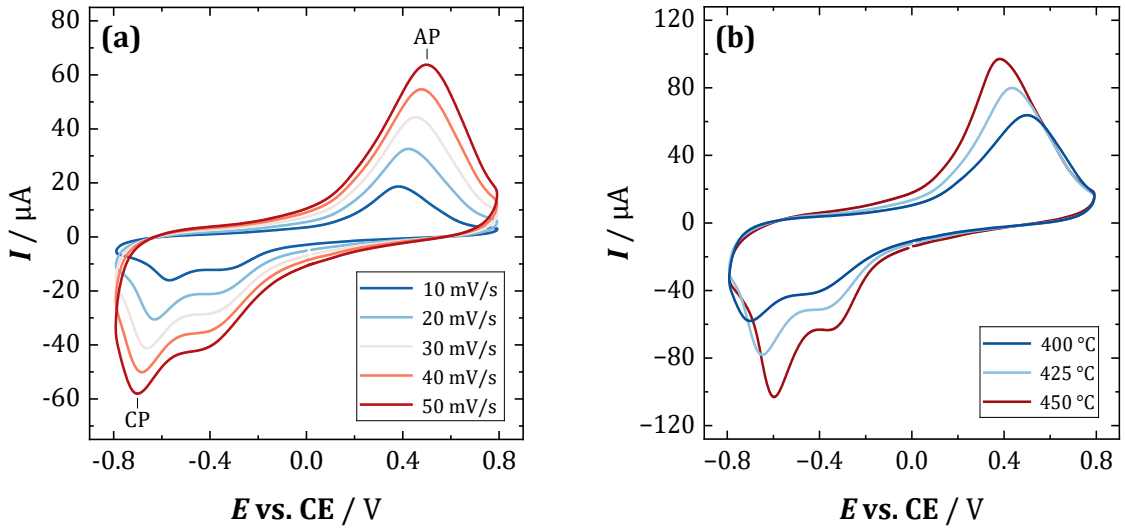

Figure 8.12: Influence of parameters on cyclic voltammograms obtained for the CeO_{2-x}/Pt/YSZ/Pt system in air (p = 1 atm); **(a)** variation of scan rate (ϑ = 400 °C); **(b)** variation of temperature (ν = 50 mV/s).

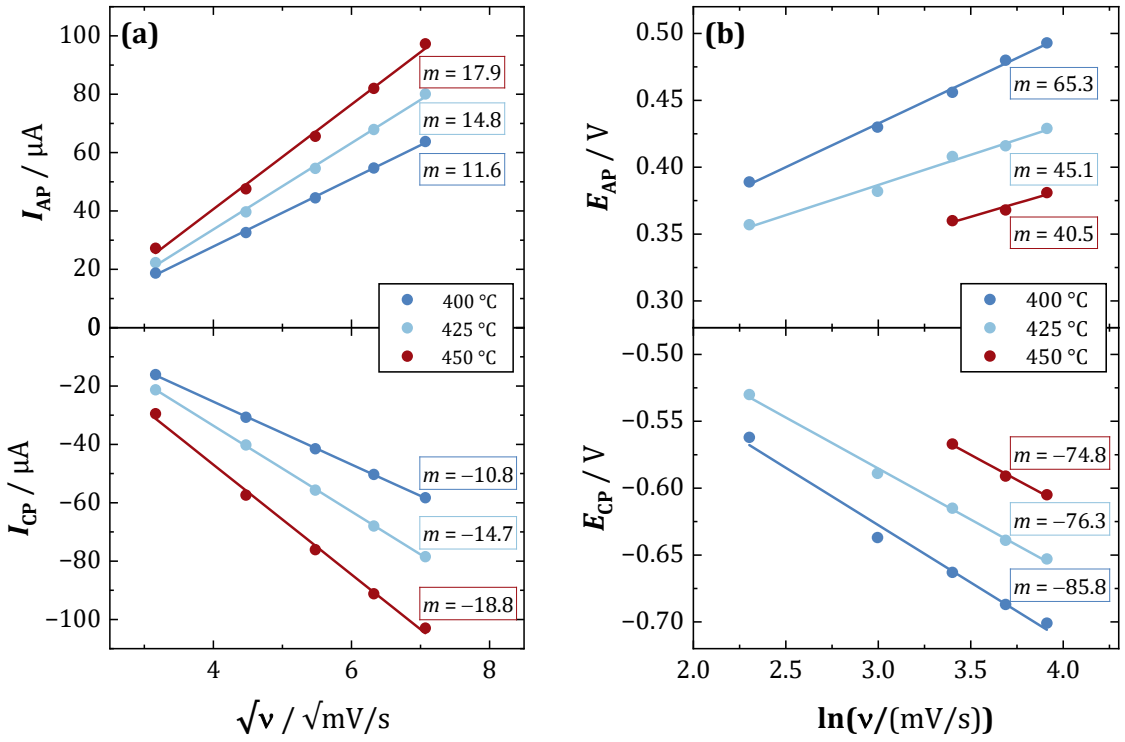

Figure 8.13: Plot of peak points ($E_P|I_P$) obtained from the anodic peak (AP) and from the cathodic peak (CP) as indicated in Figure 8.12 (a); **(a)** I_{AP} or I_{CP} vs. $\sqrt{\nu}$ plots for different temperatures with linear regression and corresponding slope m ([m] = µA√s/√mV); **(b)** E_{AP} or E_{CP} vs. ln(ν) plots for different temperatures with linear regression and corresponding slope m ([m] = mV).

8.3.2 CV Measurements with Cerium Oxide Contribution (500 °C to 600 °C)

For CV measurements in the temperature range from 400 °C to 450 °C, no significant peaks were found, which could be attributed to the cerium oxide film of the CeO_{2-x}/Pt/YSZ/Pt system (see Chapter 8.3.1). Therefore, cyclic voltammetry was performed at higher temperatures. Here, an additional peak was observed for the respective cyclic voltammogram at 500 °C (see Figure 8.14 (a)). Increasing the temperature further, this peak shifted along the *E* (vs. CE) axis as illustrated in Figure 8.14 (b). Besides, with increasing temperature, an additional cathodic peak became more pronounced. These peaks did not appear for the reference system without cerium oxide which is why they were attributed to the Ce^{4+}/Ce^{3+} redox couple. A more detailed discussion on the origin of these peaks is given below.

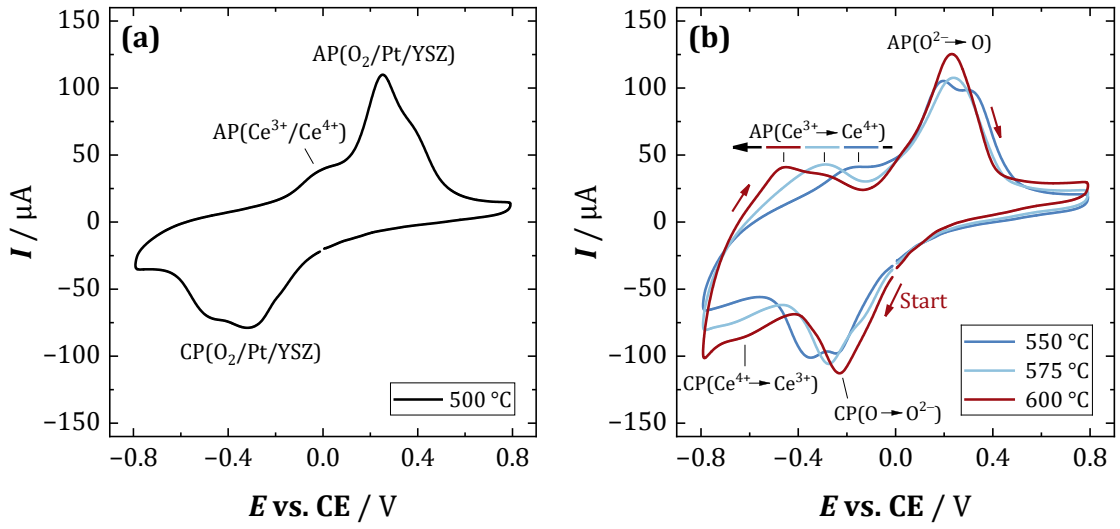

Figure 8.14: Cyclic voltammograms obtained for the CeO_{2-x}/Pt/YSZ/Pt system (ν = 50 mV/s, p(air) = 1 atm); **(a)** measurement at 500 °C; **(b)** measurements at 550 °C, 575 °C and 600 °C with an anodic (AP) and a cathodic peak (CP) associated with the Ce^{4+}/Ce^{3+} redox couple. The anodic peak shift is highlighted with an arrow.

Discussion of cerium oxide related peak(s)

As outlined above, the additional peaks were associated with the Ce^{4+}/Ce^{3+} redox couple. Considering this, the electrochemical processes indicated by the cyclic voltammogram recorded at 600 °C are discussed (see red line in Figure 8.14 (b)). The discussion focuses exclusively on processes occurring at the working electrode. Possible platinum oxide formation was neglected.

Starting from a working electrode potential of 0 V, the potential is shifted towards negative values. By that, oxygen vacancies are pumped to the working electrode. At approximately

–0.2 V (*E* vs. CE), the first cathodic peak appears, which is attributed to oxygen incorporation in YSZ at the O_2/Pt/YSZ triple phase boundary (CP($O \rightarrow O^{2-}$)). Subsequently, a second cathodic peak occurs, representing the reduction of Ce^{4+} to Ce^{3+} (CP($Ce^{4+} \rightarrow Ce^{3+}$)). This reduction process involves the removal of oxygen ions from the cerium oxide lattice. These ions migrate into YSZ and occupy oxygen vacancies accumulated beneath the working electrode during cathodic polarization. After reaching the reverse potential, an anodic peak emerges, which is assigned to the (re)oxidation of Ce^{3+} to Ce^{4+} (AP($Ce^{3+} \rightarrow Ce^{4+}$)), involving the migration of oxygen ions from YSZ back into cerium oxide. The second anodic peak corresponds to the oxygen removal at the triple phase boundary O_2/Pt/YSZ (AP($O^{2-} \rightarrow O$)). All processes described are illustrated in Figure 8.15.

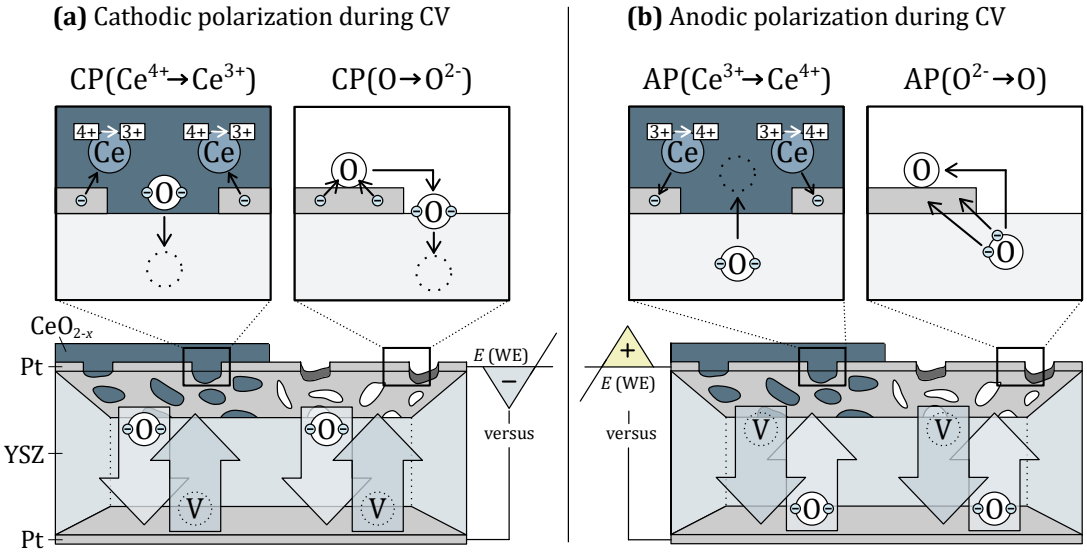

Figure 8.15: Illustration of processes assumed to occur at the CeO_{2-x}/Pt working electrode of the CeO_{2-x}/Pt/YSZ/Pt system during cyclic voltammetry (CV) measurements performed at elevated temperatures (see Figure 8.14 (b)); formation of platinum oxides is neglected; **(a)** cathodic reactions; **(b)** anodic reactions.

Here, it is emphasized that not only EIS measurements (see Chapter 8.2), but also CV measurements revealed an additional contribution that can be attributed to the Ce^{4+}/Ce^{3+} redox couple. This further substantiates the electrochemical integration of the cerium oxide film into the CeO_{2-x}/Pt/YSZ/Pt pumping system and provides an additional hint for the intended working principle (see Chapter 3.3).

Behavior of anodic cerium oxide (re)oxidation peak at different scan rates and temperatures

For further investigation of the anodic peak associated with the (re)oxidation of Ce^{3+} ions (AP($Ce^{3+}\rightarrow Ce^{4+}$)), peak values ($E_{AP}|I_{AP}$) at various temperatures and scan rates are presented in Figure 8.16. According to Equations (4.5) and (4.6), I_{AP} values were plotted against $\sqrt{\nu}$ (Figure (a)) and E_{AP} values were plotted against $\ln(\nu)$ (Figure (b)). The respective I_{AP} vs. $\sqrt{\nu}$ plots show a slight bending, indicating a deviation from linear behavior. However, corresponding slopes increase with temperature, indicating higher diffusion coefficients (see Equation (4.5)). The respective slopes for E_{AP} vs. $\ln(\nu)$ plots decrease with temperature.

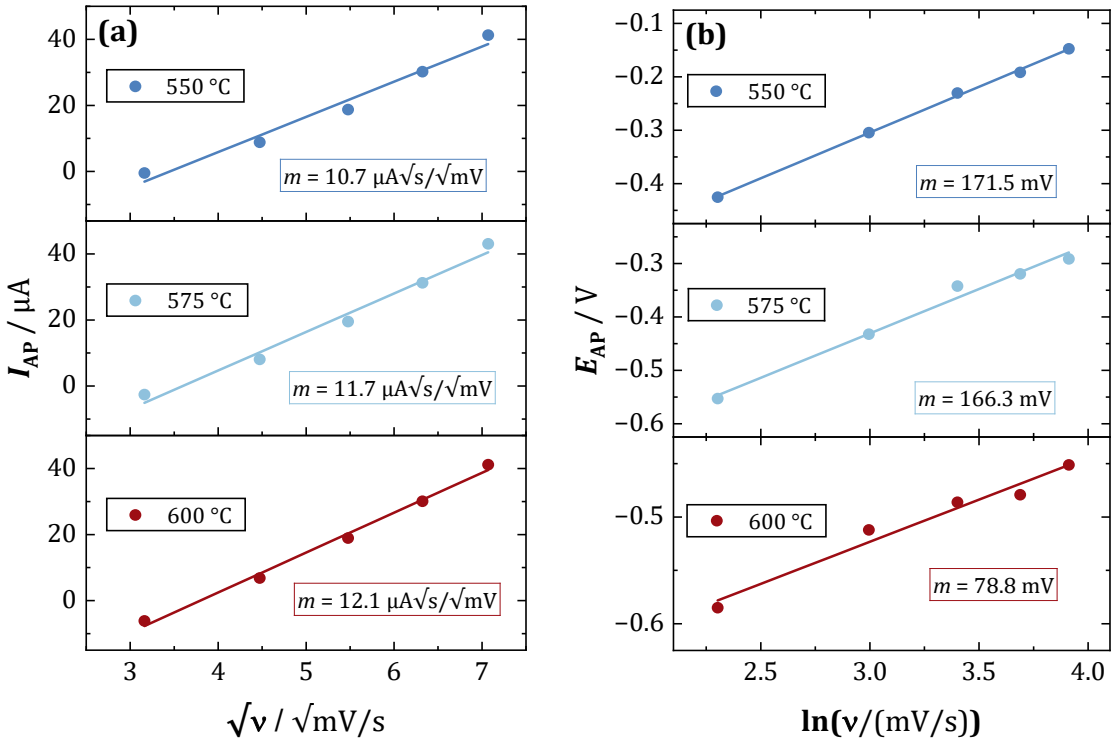

Figure 8.16: Plotting of peak points (E_{AP}/I_{AP}) attributed to the (re)oxidation of cerium oxide as a function of scan rate ν for various temperatures; **(a)** peak current I_{AP} vs. $\sqrt{\nu}$ with linear regression and corresponding slope m; **(b)** peak potential E_{AP} vs. $\ln(\nu)$ with linear regression and corresponding slope m.

8.4 Potentiostatic Polarization on CeO_{2-x}/Pt/YSZ/Pt

In this chapter, potentiostatic polarization experiments on the CeO_{2-x}/Pt/YSZ/Pt system are presented. The de-wetted working platinum electrode was polarized anodically and cathodically (vs. CE) to examine differences in resulting currents. By this, the influence of applied potential (Chapter 8.4.1) and temperature (Chapter 8.4.2) was investigated. Beyond that, it has been investigated how dwell time at a certain temperature influences the polarization experiments. Here, the formation of platinum oxides is considered.

8.4.1 Influence of Applied Potential

Within this chapter, the influence of potential E_{POL} on potentiostatic polarizations of the CeO_{2-x}/Pt/YSZ/Pt system is presented. Comparatively low potentials (E_{POL} = ±100 mV, ±150 mV and ±200 mV) were applied to avoid irreversible changes of the sample. It has been shown that high potentials can lead to oxygen bubble formation beneath dense platinum film electrodes and to subsequent film delamination and cracking[50,58,64,65]. Furthermore, a reduction of the electrolyte is possible under strong polarization conditions[66,67]. Figure 8.17 (a) shows the resulting I versus t curves obtained during potentiostatic polarizations at 450 °C (t_{POL} = 2 min, p(air) = 1 atm). The decline of I could be described in good agreement by a $1/\sqrt{t}$ dependency (see Figure (b)), thereby obeying Cottrell's law (4.8). However, cathodic currents deviate more from linear behavior, which could be caused by two processes occurring during cathodic polarization (see discussion in Chapter 8.4.2).

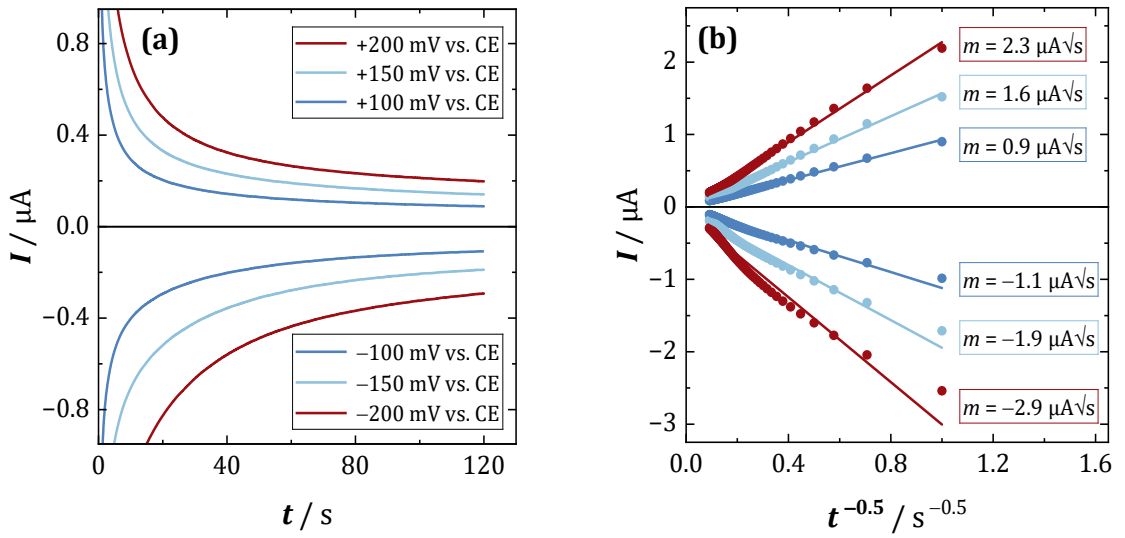

Figure 8.17: **(a)** I versus t curves obtained during potentiostatic polarizations of the CeO_{2-x}/Pt/YSZ/Pt system for various applied potentials (t_{POL} = 2 min, ϑ = 450 °C, p(air) = 1 atm); **(b)** corresponding plots of I versus $1/\sqrt{t}$ with linear regressions and corresponding slopes m.

In general, cathodic currents were higher in absolute values than anodic currents. This can be quantified by the converted charge Q, *i.e.*, the area beneath the respective I vs. t curve. Additionally, it can be demonstrated by the current value after two minutes of polarization (= I_{2min}). The respective plots of Q and $|I_{2min}|$ for the respective electrode potentials E (vs. CE) can be seen in Figure 8.18. A discussion explaining higher cathodic currents is given in Chapter 8.4.2.

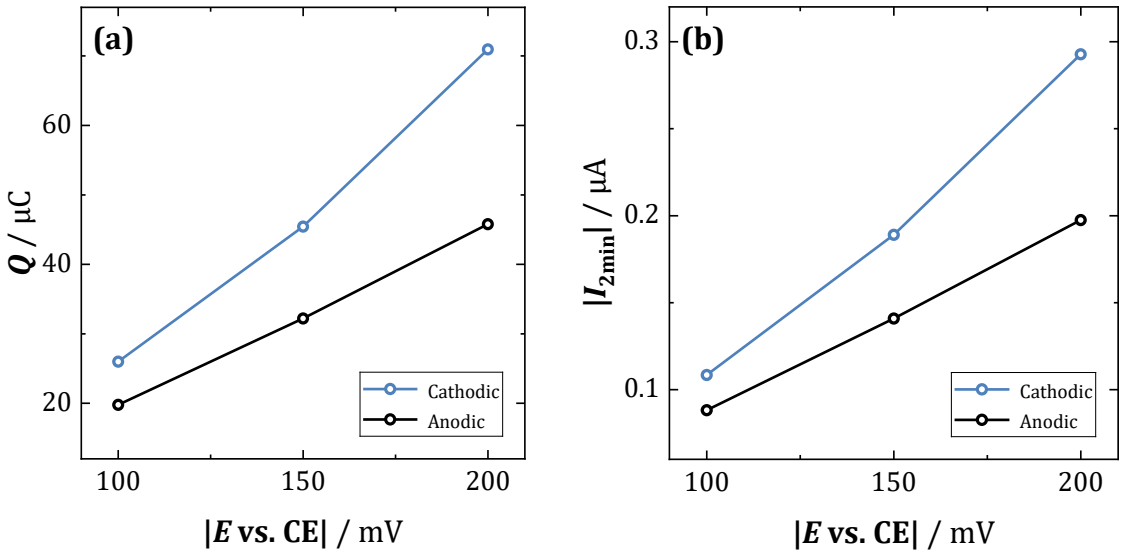

Figure 8.18: Quantification of anodic and cathodic currents obtained for various potentials during potentiostatic polarizations of the CeO_{2-x}/Pt/YSZ/Pt system (t_{POL} = 2 min, ϑ = 450 °C, p(air) = 1 atm); **(a)** converted charge Q vs. absolute working electrode potential $|E$ vs. CE|; **(b)** absolute current value after 2 minutes $|I_{2min}|$ vs. absolute working electrode potential $|E$ vs. CE|.

8.4.2 Influence of Temperature

This chapter shows the influence of temperature on potentiostatic polarization experiments. For that, the CeO_{2-x}/Pt/YSZ/Pt system was polarized at various temperatures from 400 °C to 600 °C (E_{POL} = ±200 mV, t_{POL} = 2 min, p(air) = 1 atm). Figure 8.19 (a) shows the resulting I vs. t curves. It is clearly visible that a higher temperature led to an increase in current. Figure 8.19 (b) shows the development of working electrode potential E (vs. CE) after the potential was applied. The potential E settled down to approximately 0 V. Here, equilibrium is reached faster at higher temperatures. Besides, the respective decline is faster after anodic polarization. This would be in good agreement with the fact that anodic polarization led to less converted charge (see Figure 8.20). Accordingly, less charge needs to be re-converted.

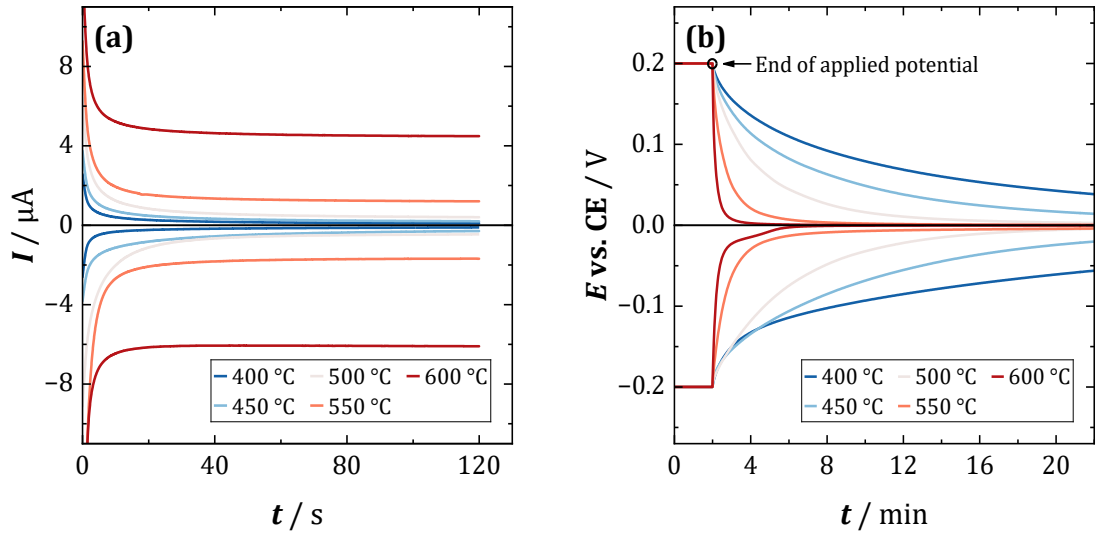

Figure 8.19: Potentiostatic polarizations of the CeO_{2-x}/Pt/YSZ/Pt system performed at various temperatures (E_{POL} = ±200 mV; t_{POL} = 2 min, p(air) = 1 atm); **(a)** resulting I vs. t curves; **(b)** development of working electrode potential E (vs. CE) after potential was applied.

As already noted in Chapter 8.4.1, cathodic polarization led to higher currents than anodic polarization. This is also valid for various temperatures as illustrated in Figure 8.20. For quantification, the converted charge Q and the absolute current value $|I_{2min}|$ are presented.

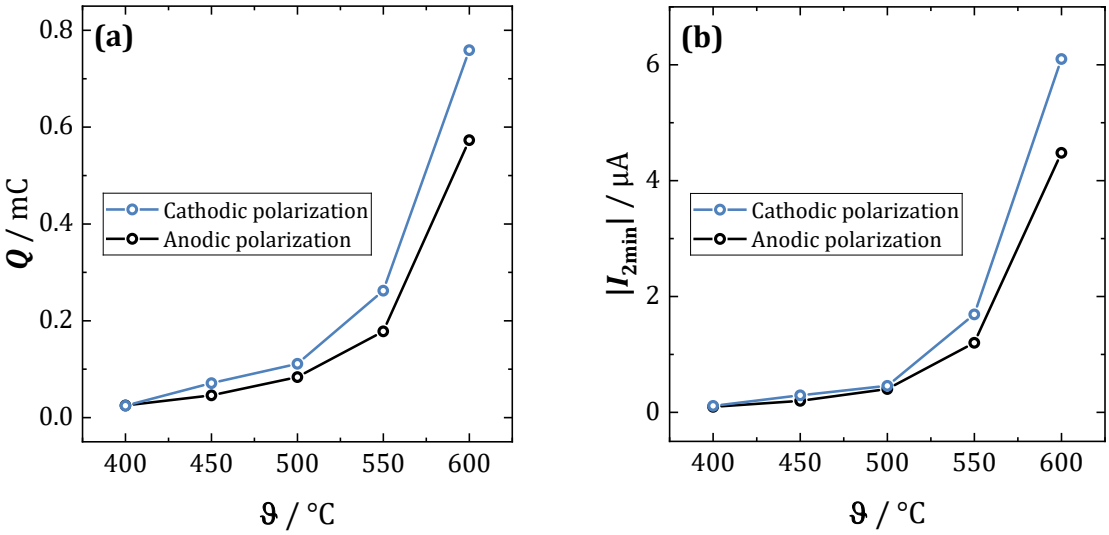

Figure 8.20: Quantification of anodic and cathodic currents obtained for various temperatures during potentiostatic polarizations of the CeO_{2-x}/Pt/YSZ/Pt system; **(a)** converted charge Q vs. ϑ; **(b)** absolute current values after 2 minutes $|I_{2min}|$ vs. ϑ.

Discussion of higher cathodic current

For both anodic and cathodic polarization, a certain amount of resulting current is caused by the electrode process taking place at the O_2/Pt/YSZ triple phase boundary, *i.e.*, the removal and incorporation of oxygen (see Figure 8.21). In case of cathodic polarization (a), oxygen surface species receive electrons from the electrode. Vice versa, the electrode receives electrons from lattice oxygen when polarized anodically (b). Both cases contain electron transfer and contribute to the current, accordingly. However, an additional process associated with the Ce^{4+}/Ce^{3+} redox couple could only occur when the electrode is polarized cathodically.

For explanation, the stoichiometry of cerium oxide is considered a key aspect. According to spectroscopic measurements presented in Chapter 6, annealing in air ($p(O_2) \approx 0.2$ atm) led to an incorporation of oxygen, which resulted in nearly stoichiometric cerium oxide (CeO_{2-x} with $x \approx 0$). Since polarization experiments were also performed at elevated temperatures in air, nearly stoichiometric cerium oxide (CeO_2) is concluded. This means a very low concentration of oxygen vacancies and a Ce^{3+}/Ce^{4+} ratio of approximately 0. Considering this stoichiometric condition, an explanation for polarization results can be derived.

When the CeO_{2-x}/Pt electrode is polarized cathodically, oxygen vacancies are pumped towards the CeO_{2-x}/YSZ interface. Additionally, Ce^{4+} ions at the CeO_{2-x}/Pt/YSZ triple phase boundary are reduced to Ce^{3+} by the platinum electrode. By that, oxygen ions can be released from the cerium oxide lattice, migrate into YSZ and occupy oxygen vacancies. This process includes electron transfer and therefore an additional part for current is given. When the CeO_{2-x}/Pt electrode is polarized anodically, oxygen ions are pumped to the CeO_{2-x}/YSZ interface. However, these oxygen ions cannot be introduced to the cerium oxide lattice since no oxygen vacancies are present. For introducing an oxygen ion into cerium oxide, oxidation of cerium ions would be necessary to maintain electrical neutrality. However, only Ce^{4+} ions are present, which cannot be oxidized. Accordingly, no charge transfer and, thus, no additional contribution to the current is possible. The as-described mechanisms are also illustrated in Figure 8.21.

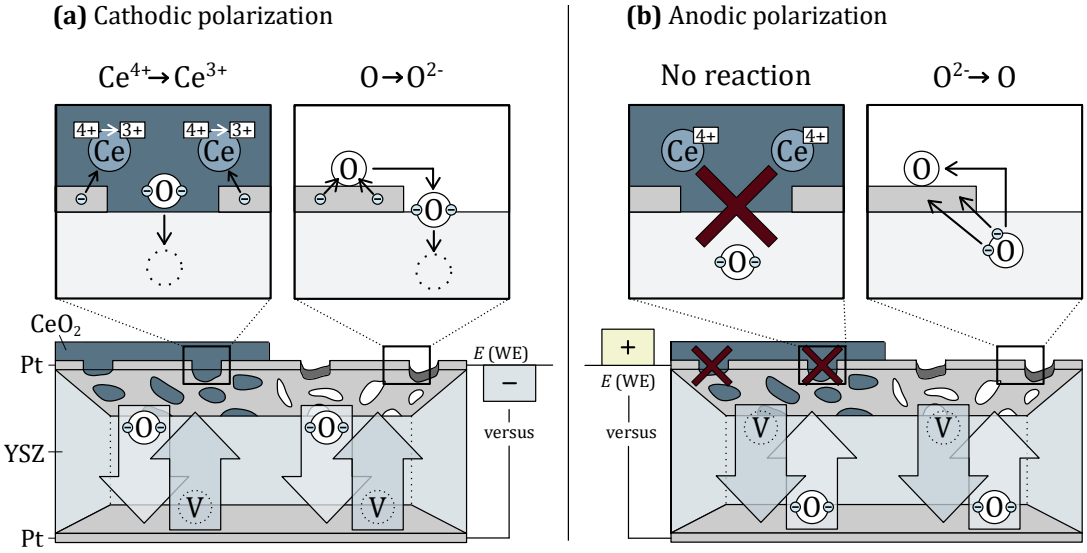

Figure 8.21: Illustration of assumed processes during potentiostatic polarization of the CeO_{2-x}/Pt/YSZ/Pt system; **(a)** reactions occurring at the working electrode during cathodic polarization; **(b)** reactions occurring at the working electrode during anodic polarization.

8.4.3 Formation of Platinum Oxides indicated by Polarization Experiments

Potentiostatic polarization experiments on the CeO_{2-x}/Pt/YSZ/Pt system with the same parameters (E_{POL} = ±200 mV, t_{POL} = 2 min, ϑ = 500°C, p(air) = 1 atm) were performed at intervals of one hour. The sample was heated up to 500 °C and after one hour at 500 °C, a first polarization was performed. After another hour, *i.e.*, 2 hours at 500 °C, another polarization measurement was done. This was done five times in total. Figure 8.22 shows the resulting I vs. t curves that were obtained during respective polarizations. For anodic and cathodic polarization, a respective current decrease with increasing dwell time was observed.

For this decrease, proceeding formation of platinum oxides (PtO_x) might be an explanation. Platinum oxides impede the electrode reaction taking place at the O_2/Pt/YSZ triple phase boundary[63]. In Chapter 8.2.1 it was already shown for the CeO_{2-x}/Pt/YSZ/Pt system that the resistance of this electrode process (= R_{EP}) increases with $\sqrt{t}$ while annealing in air. According to that, a $1/\sqrt{t}$ dependency on current I would be conclusive. A respective plot for I_{2min}, *i.e.*, the current value after two minutes of polarization, is presented in Figure 8.22 (b). Here, a certain bending in the plots can be observed, which could be ascribed to the fact that I_{2min} is not stationary. Indeed, current would further decrease with longer polarization time. However, the slopes obtained for linear regressions are quite similar. From that, it could be

concluded that forming platinum oxides impede anodic and cathodic reactions in the same way.

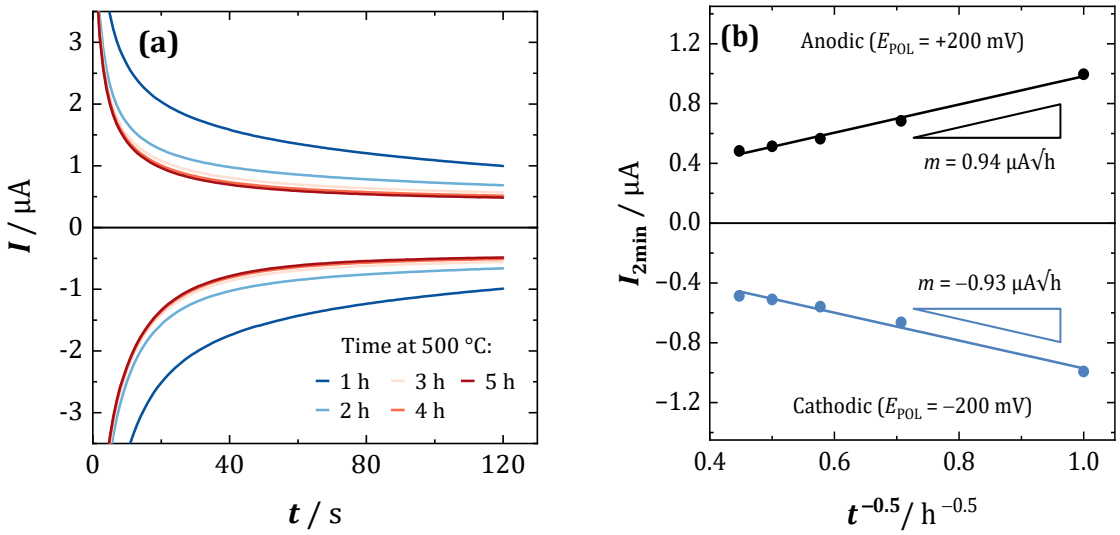

Figure 8.22: Potentiostatic polarization measurements performed at an interval of one hour at 500 °C in air (E_{POL} = ±200 mV, t_{POL} = 2 min, p = 1 atm); **(a)** I vs. t curves with increasing dwell time at 500 °C; **(b)** corresponding I_{2min} vs. $1/\sqrt{t}$ plots with linear regression and corresponding slopes m.

9 Operando XPS

The electrochemical characterization of the CeO_{2-x}/Pt/YSZ/Pt prototype system revealed contributions that were ascribed to the oxidation or reduction of the cerium oxide film (see Chapter 8). Although this could be seen as a hint for the intended working principle, no information about the oxidation state of cerium oxide could be derived from that. Accordingly, a setup was necessary that enabled the spectroscopic investigation of cerium oxide subsequently to polarization. Aiming at that, an *operando* XPS setup was established that allowed sample heating and the connection of a potentiostat (Chapter 9.1). The setup was first used to investigate how the cerium oxide film of the CeO_{2-x}/Pt/YSZ/Pt system behaves under UHV conditions at elevated temperatures (Chapter 9.2). Afterwards, potentials were applied to the CeO_{2-x}/Pt/YSZ/Pt system to prove whether the oxidation state of cerium oxide could be influenced. Here, cathodic and anodic polarizations were performed to reduce and oxidize the cerium oxide film (Chapter 9.3).

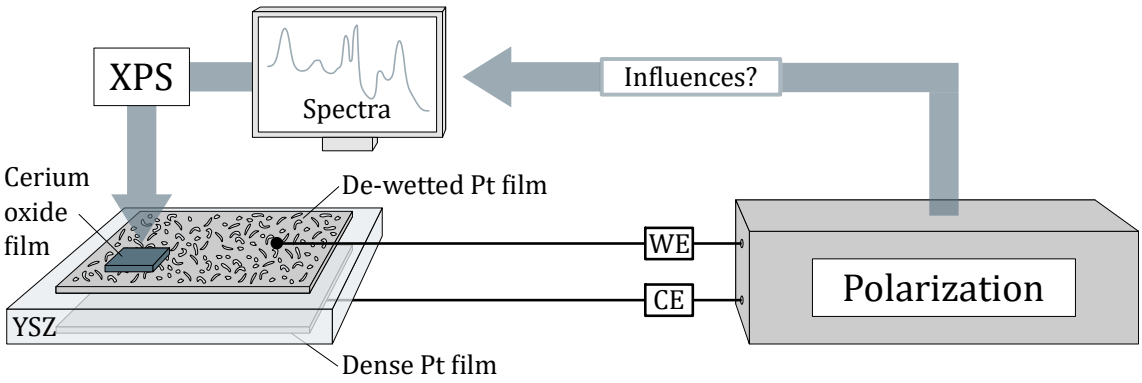

Figure 9.1: Illustration of Chapter 9. Based on an *operando* setup, the cerium oxide film of a CeO_{2-x}/Pt/YSZ/Pt system could be investigated by X-ray photoelectron spectroscopy (XPS) subsequently to anodic or cathodic polarization. By that, the working principle, *i.e.*, the reduction and oxidation of the cerium oxide film, could be proven.

9.1 Establishment of the Setup

This chapter describes the setup for *operando* XPS measurements and is divided into three parts. The first part shows the preparation of an adjusted CeO_{2-x}/Pt/YSZ/Pt system. An adjustment was required for geometric reasons. The second part shows the assembly of the XPS sample holder, and the third part shows the determination of real sample temperature within the XPS chamber.

Preparation of an adjusted CeO_{2-x}/Pt/YSZ/Pt system

To conduct *operando* experiments with a CeO_{2-x}/Pt/YSZ/Pt system, the area of the cerium oxide film had to be reduced in comparison to the prototype system shown in Chapter 8. This was necessary for not covering the cerium oxide film with the stainless-steel stripe or with the pin fingers (see Figure 9.3). Thus, another system with a round cerium oxide film (diameter = 1.5 mm) was prepared by PLD as shown in Figure 9.2. Except for the adjusted geometry of the cerium oxide film, almost the same parameters as depicted in Chapter 8.1 were applied for the depositions. Only the number of pulses were changed for fabrication of a de-wetted platinum film (N = 25,200) and for the cerium oxide film (N = 9,000). For the de-wetted platinum film, the number of pulses had to be adjusted to achieve a comparable degree of de-wetting like shown in Chapter 8.1. Regarding the cerium oxide film, only ¼ of the pulses (compared to Chapter 8.1) were applied to achieve a thinner film. A thinner film might be easier to oxidize or reduce due to a lower amount of oxygen to be converted. It was assumed that the cerium oxide film had a thickness of 1 µm (= ¼ · 4 µm) (cf. Chapter 5.2).

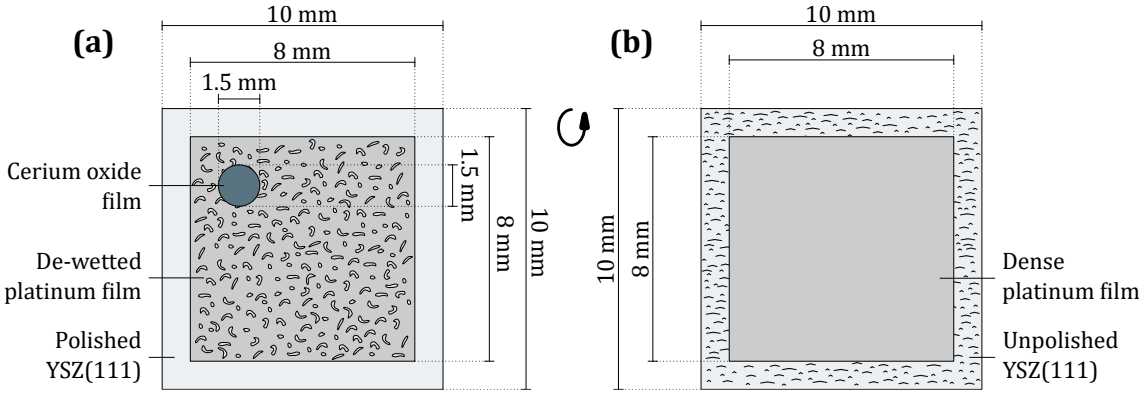

Figure 9.2: Geometries of the adjusted CeO_{2-x}/Pt/YSZ/Pt system to be applied for *operando* XPS experiments; films were prepared by pulsed laser deposition; **(a)** a de-wetted platinum film was grown on the polished side of the YSZ(111) substrate; on top of this film, a cerium oxide film was deposited; **(b)** a dense platinum film was deposited on the unpolished backside of the YSZ(111) substrate.

Preparation of the sample holder

The *operando* XPS experiments were based on a sample holder possessing a heating plate that could reach 500 °C. Besides, electrical pins allow the connection of a potentiostat out of the setup. For sample holder assembly, an Al_2O_3 substrate (V = 20 mm × 10 mm × 1 mm) with a platinum film was first placed on the heating plate of the sample holder. The platinum deposition was performed by PLD with an area of 16 mm × 6 mm (E = 400 mJ, $\vartheta_{\mathrm{Heater}}$ = 700 °C, f = 6 Hz, p(Ar) = 2 Pa, N = 14,400). In this setup, Al_2O_3 was used since it is electrically insulating and exhibits high thermal conductivity[17]. Thereby, no electrical contact between the heating plate and the bottom platinum electrode is given. In the next step, the CeO_{2-x}/Pt/YSZ/Pt sample was placed on the Al_2O_3 substrate and fixed with a stainless-steel stripe and two ceramic screws. Besides, two ceramic rings were placed between the sample holder and the stainless-steel stripe. Lastly, two pin fingers were applied for bonding. The functionality of this setup was proven by impedance spectroscopy (see next part).

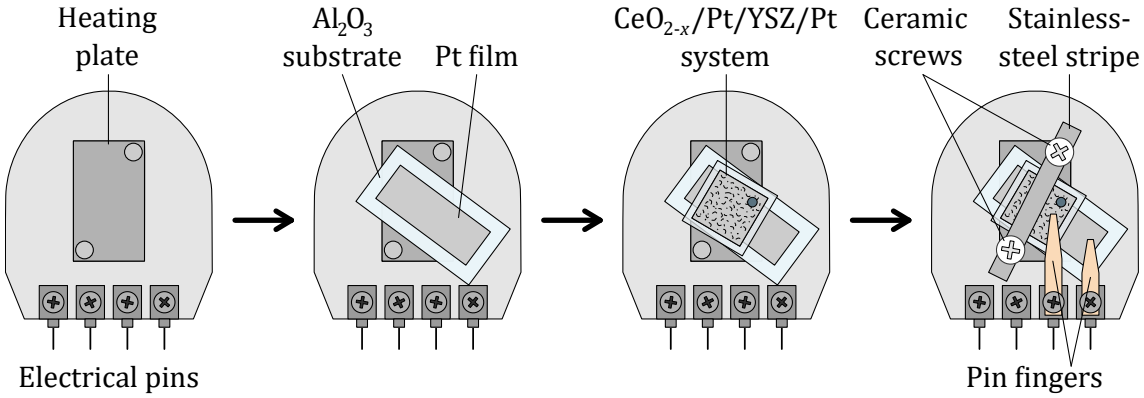

Figure 9.3: Illustration of sample holder assembly for *operando* XPS measurements. The CeO_{2-x}/Pt/YSZ/Pt system is placed on a platinum coated Al_2O_3 substrate and is fixed by a stainless-steel stripe and ceramic screws. Connection to a potentiostat is given by electrical pins and pin fingers.

Real temperature of the sample within the XPS chamber

Electrochemical impedance spectroscopy was applied for estimating the real sample temperature. Figure 9.4 (a) shows a Nyquist plot (R_{YSZ}CPE-CPE), which was obtained for the CeO_{2-x}/Pt/YSZ/Pt system two hours after the heating plate reached 500 °C. The semicircle was ascribed to the bulk resistance of YSZ (R_{YSZ} = 2.46 kΩ). Considering the corresponding data for impedance measurements at various temperatures, a temperature of around 385 °C could be concluded for the CeO_{2-x}/Pt/YSZ/Pt system. This temperature should be considered a middle temperature since the sample is back-heated. Thus, the bottom platinum electrode is likely hotter than the upper electrode as illustrated by the cross-section scheme in Figure 9.4 (b). According to that, the cerium oxide film probably has a

temperature of less than 385 °C since it is located on top of the upper electrode. Another issue that must be regarded is the fact that R_{YSZ} values decrease slightly with time. Six hours after the heater reached 500 °C, a bulk resistance of 2.27 kΩ was determined meaning a real temperature of 387 °C. Therefore, 385 °C can just be considered a rough estimation for the presented *operando* experiments.

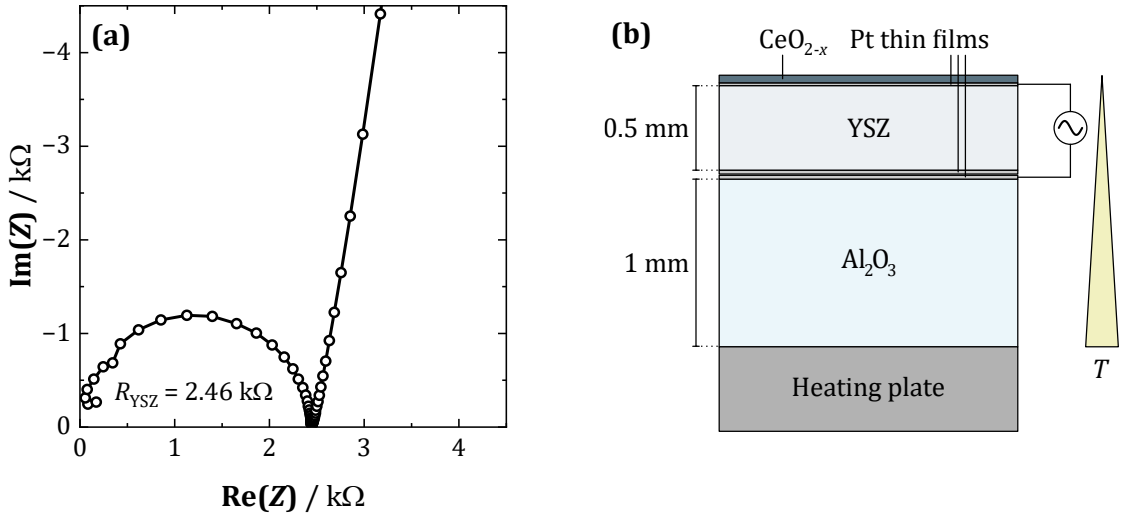

Figure 9.4: Applying electrochemical impedance spectroscopy for estimation of the real temperature of the CeO_{2-x}/Pt/YSZ/Pt sample during *operando* XPS measurements; **(a)** Nyquist plot for the CeO_{2-x}/Pt/YSZ/Pt system obtained two hours after heating plate reached 500 °C; **(b)** cross-section of the assembly with an assumed gradient in temperature.

9.2 XPS Measurements during UHV Annealing

The cerium oxide film of the CeO_{2-x}/Pt/YSZ/Pt system was first investigated by XPS without applying an electric potential. Here, a measurement was performed initially without heating. The resulting Ce 3d XP spectrum is shown in Figure 9.5 (a). Six peaks can be seen indicating nearly stoichiometric CeO_{2-x} with x near to 0[21]. Only two small shoulders around 885 eV and 903 eV indicate a slight reduction[110]. This slight reduction is probably caused by preparation via PLD and was already described in Chapter 6.3. After initial XPS measurements, heating process to 500 °C was started. This was done stepwise within five hours for controlled degassing of the sample. When the heating plate reached 500 °C, XPS measurements were conducted at an interval of 30 minutes. As described in Chapter 9.1, the real temperature of the sample was assumed to be around 385 °C. The resulting Ce 3d XP spectra exhibit a growth of the as-mentioned shoulders, meaning a proceeding reduction of the cerium oxide film. The reduction of cerium oxide due to annealing in UHV is well documented in literature[110,119,120].

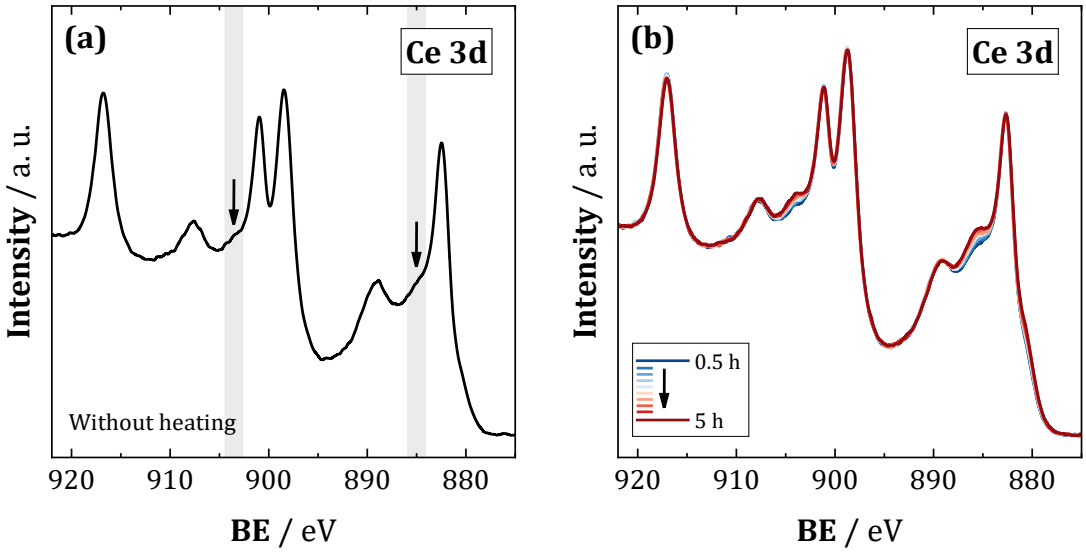

Figure 9.5: Ce 3d XP spectra of the cerium oxide film of the CeO_{2-x}/Pt/YSZ/Pt system; **(a)** measurement without heating showing two slight shoulders; **(b)** development of the XP spectra after heater reached 500 °C ($\vartheta_{Sample} \approx 385$ °C); two shoulders grow with increasing time.

Figure 9.6 shows the corresponding XP spectra for Ce 4d (a) and O 1s (b). For Ce 4d, no significant change due to heating could be observed like for the Ce 3d XP spectra. For the O 1s peak, however, a peak shift was obtained. Without heating, this peak was located at around 529.5 eV. When the heater reached 500 °C, the peak position was located at

529.7 eV. Accordingly, the peak shift already occurred during stepwise heating to 500 °C. When 500 °C were reached, no significant change for the O 1s peak was observed.

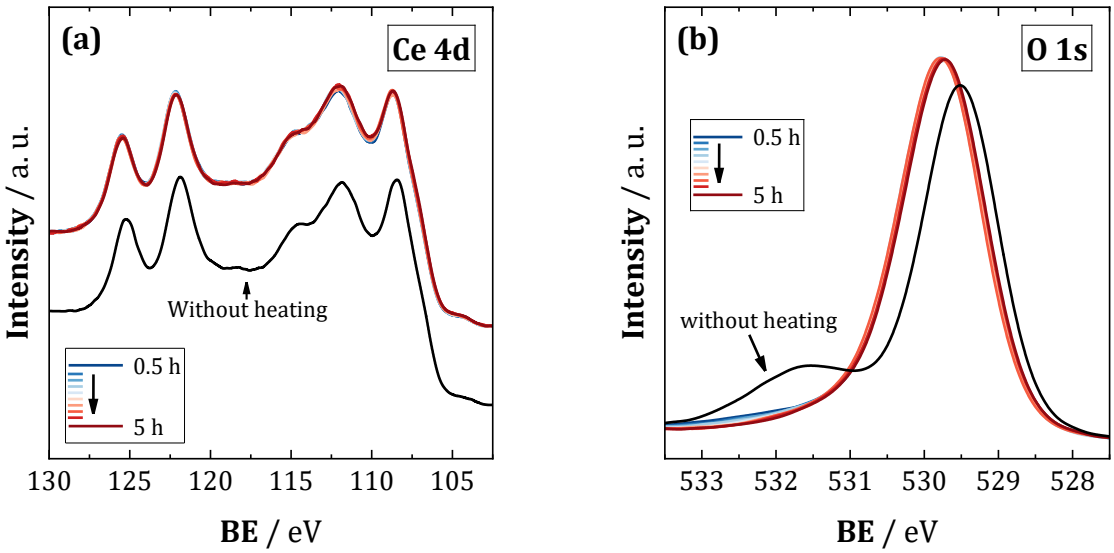

Figure 9.6: Comparison of XP spectra for the cerium oxide film of the CeO_{2-x}/Pt/YSZ/Pt system obtained without heating and with increasing dwell time at ϑ_{Heater} = 500 °C (ϑ_{Sample} ≈ 385 °C); **(a)** Ce 4d XP spectra; **(b)** O 1s XP spectra.

9.3 XPS Measurements after Applying a Potential

In this chapter, the results of *proof of principle* measurements are presented. Accordingly, the effect of applying an electric potential to the CeO_{2-x}/Pt/YSZ/Pt system is investigated by measuring XPS on the cerium oxide film before and after polarization. Here, reduction (part 1) and oxidation (part 2) were tested. In general, it was ensured that XP spectra were constant before applying a potential. As illustrated in Figure 9.1, the de-wetted platinum film is considered the working electrode and the dense platinum film is considered the counter electrode. The temperature of the sample is assumed to be 385 °C (see Chapter 9.1).

Cathodic polarization for reduction of cerium oxide

It was calculated that roughly 148 nmol of oxygen ions are present in the cerium oxide film of the CeO_{2-x}/Pt/YSZ/Pt system. For calculation, stoichiometric cerium oxide with a volume of $1.77 \cdot 10^6$ µm³ was assumed. This amount of oxygen ions corresponds to a total charge of 28.6 mC, assuming two elementary charges per oxygen ion. Taking into account that only two of eight oxygen ions per unit cell could be removed, a total charge of 7.15 mC could be excorporated from the lattice. By that, CeO_2 would be completely reduced down to $CeO_{1.5}$.

According to this calculation, currents in a range of µA would be necessary for several minutes to obtain significant changes in the oxidation state. For reduction, various cathodic potentials were subsequently applied to the CeO_{2-x}/Pt/YSZ/Pt system (t_{POL} = 3 min, respectively). By that, currents in the range of µA were obtained (see Figure 9.7).

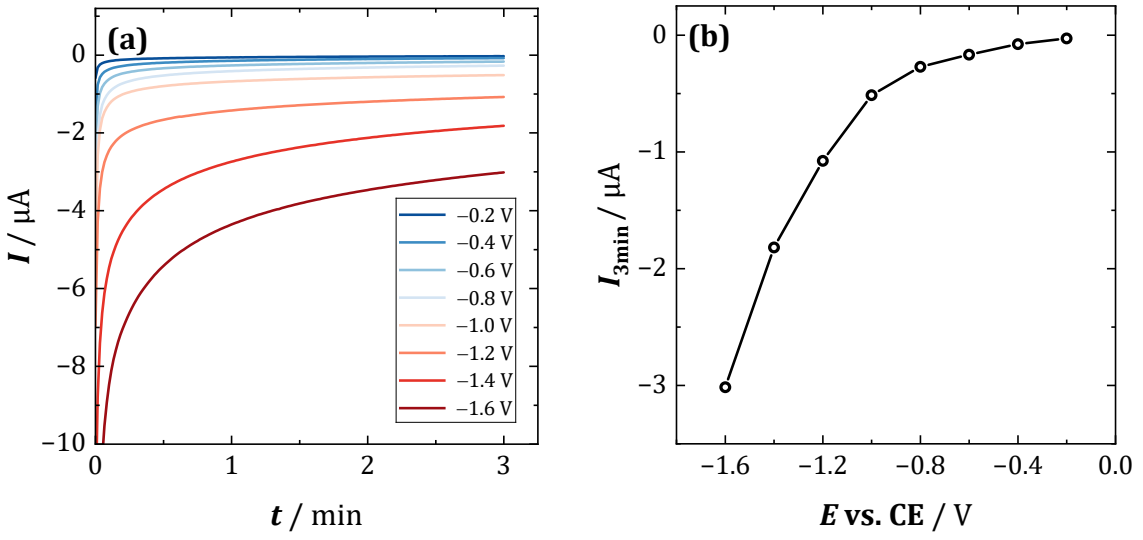

Figure 9.7: Cathodic polarization tests of the CeO_{2-x}/Pt/YSZ/Pt system under UHV conditions at around 385 °C; various potentials E were applied for 3 minutes to the de-wetted electrode (vs. CE); **(a)** I vs. t curves for various cathodic potentials during potentiostatic polarizations; **(b)** I_{3min} values vs. working electrode potential E (vs. CE). Lines are drawn between data points to indicate the trend.

In total, 1.84 mC of charge *Q* were moved or converted due to cathodic polarizations shown in Figure 9.7. This already had an influence on the oxidation state of cerium oxide as the corresponding XP spectra for Ce 3d and Ce 4d show (see Figure 9.8), which were recorded under OCV conditions after the last polarization was performed. The influence on the XP spectra for O 1s is too small to be significant which is why it is not presented here. It can be found in Figure 11.13 in the Appendix.

Regarding the respective Ce 3d XP spectra (a), several features were observed that imply a reduction of the cerium oxide surface[110]. First, peak growths at 885.5 eV (II) and 903.9 eV (III) indicate an increased concentration of Ce^{3+} ions. The decreasing peak intensity at 916.9 eV (IV) corresponds to a lower concentration of Ce^{4+} ions than before. Additionally, shoulder growth (I) between 880 eV and 881 eV respresents an increased amount of Ce^{3+} ions. Beyond that, changes in the Ce 4d XP spectra (b) were also obtained as peak intensities at 122.0 eV (III) and 125.3 eV (IV) decrease while peak intensities at 108.6 eV (I) and 111.9 eV (II) increase. This also implies a reduction of the cerium oxide surface[121].

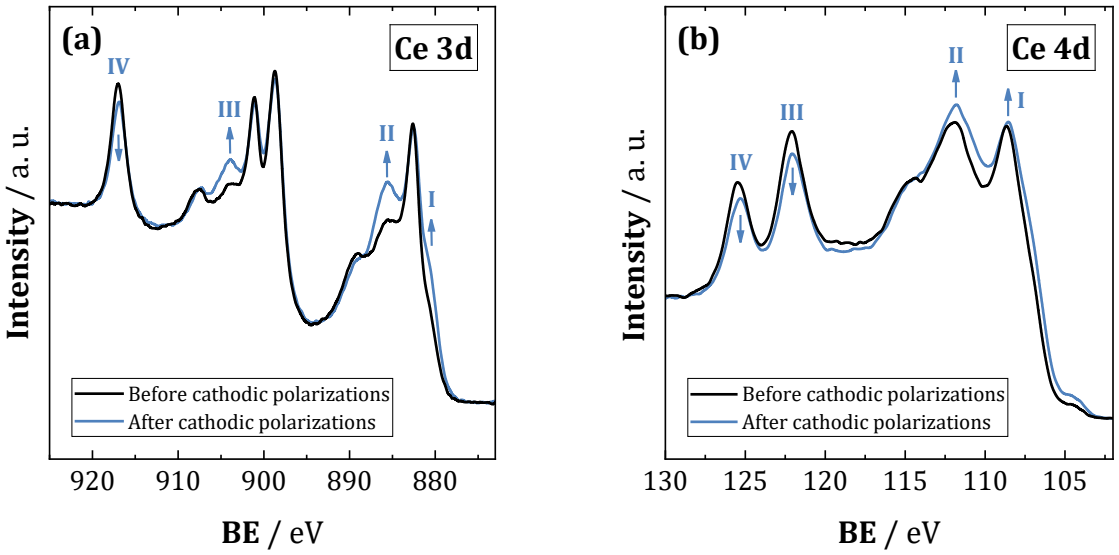

Figure 9.8: Comparison of XP spectra obtained under OCV conditions for the cerium oxide film of the CeO_{2-x}/Pt/YSZ/Pt system before (black) and after (blue) cathodic polarization test measurements ($\vartheta_{Sample} \approx$ 385 °C); the effect of cathodic polarization is illustrated by arrows; **(a)** Ce 3d XP spectra; **(b)** Ce 4d XP spectra.

This result is regarded a first proof for the intended working principle as the oxidation state of the cerium oxide surface was succefully influenced through polarization. Moreover, a reduction due to cathodic polarization was expected. During cathodic polarization, Ce^{4+} ions

are reduced to Ce^{3+} by the de-wetted platinum electrode whereby oxygen ions can be released from the cerium oxide lattice and migrate into YSZ (see Chapter 3.3).

Without applying any further electric potential, the oxidation state change achieved through cathodic polarization remains constant as indicated by a second XPS measurement conducted 30 minutes after the first measurement. This is valid for the Ce 3d XP spectra as well as for the Ce 4d XP spectra (see Figure 9.9).

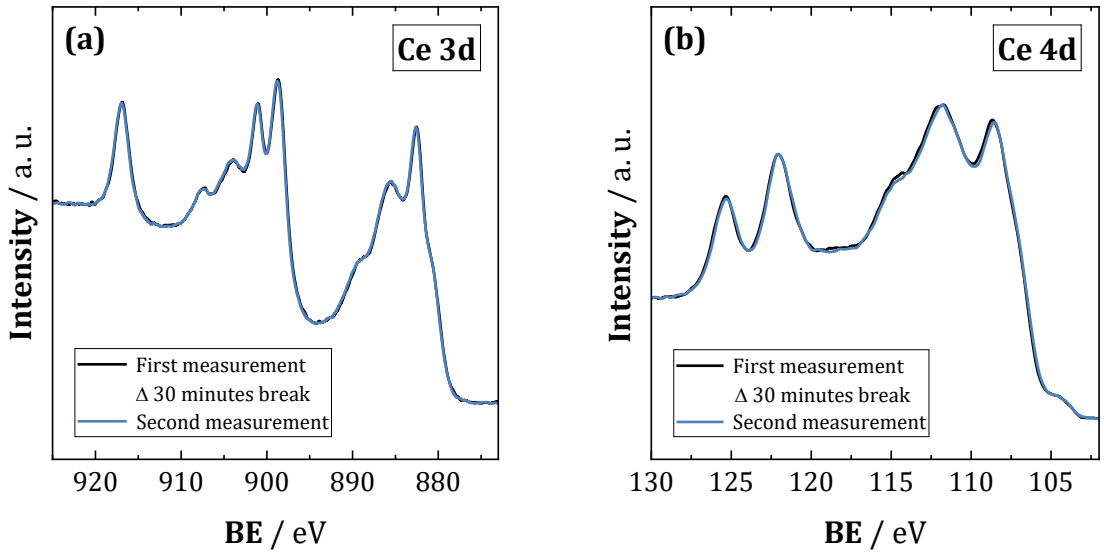

Figure 9.9: Comparison of the first XP spectrum obtained for the cerium oxide film of the CeO_{2-x}/Pt/YSZ/Pt system after cathodic polarizations (black) and a further spectrum that was obtained 30 minutes after the first measurement was performed (blue); measurements were conducted under OCV conditions; **(a)** Ce 3d XP spectra; **(b)** Ce 4d XP spectra.

Anodic polarization for oxidation of cerium oxide

As cathodic polarization of the CeO_{2-x}/Pt/YSZ/Pt system led to a reduction of the corresponding cerium oxide film, anodic polarization had to be performed to examine the reverse reaction, *i.e.*, the oxidation of the cerium oxide film. Therefore, a potential of +1.6 V was applied for 15 minutes to the de-wetted electrode (vs. CE) (Q = 16.4 mC). Indeed, an oxidation of the cerium oxide film was observed after the potential was applied. In the corresponding Ce 3d and Ce 4d XP spectra, the opposite effects as after cathodic polarization were obtained (cf. peaks I-IV in Figures 9.10 and 9.8, respectively). Also here, no significant change in corresponding O 1s XP spectra was obtained (see Figure 11.14 in the Appendix). Like after cathodic polarizations, the corresponding XP spectra after anodic polarization remain constant. Without applying any further potential, a second XPS measurement, taken 30 minutes after the first one, led to a spectrum with no significant changes compared to the first one (see Figures 9.11).

Finally, the results of anodic polarization verify the pumping principle of the CeO_{2-x}/Pt/YSZ/Pt system as oxygen ions are incorporated into cerium oxide (see Chapter 3.3). Accordingly, a system was successfully devised that enables both the oxidation and the reduction of a cerium oxide film.

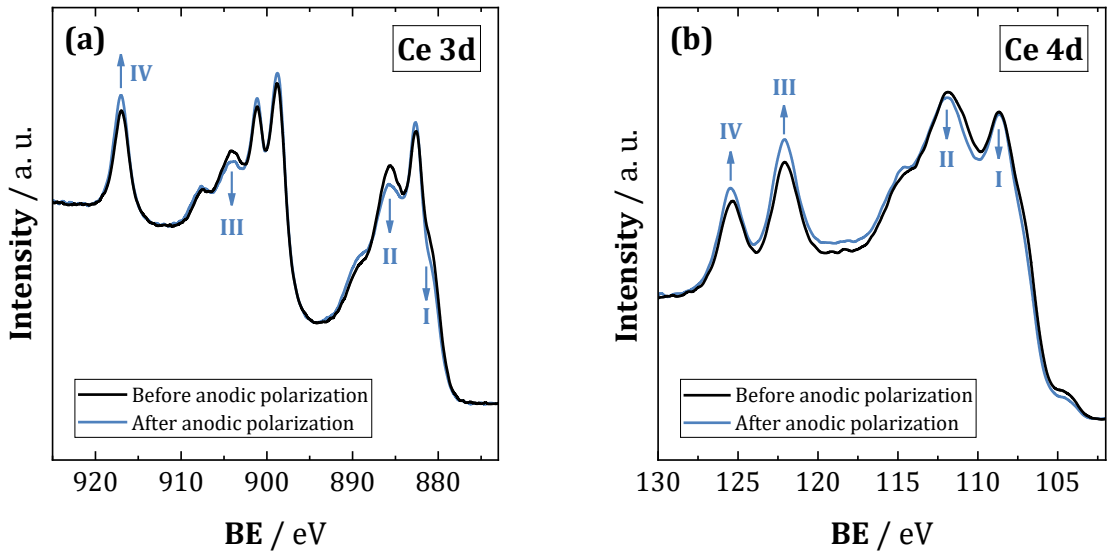

Figure 9.10: Comparison of XP spectra obtained under OCV conditions for the cerium oxide film of the CeO_{2-x}/Pt/YSZ/Pt system before (black) and after (blue) anodic polarization (ϑ_{Sample} ≈ 385 °C); the effect of anodic polarization is illustrated by arrows; **(a)** Ce 3d XP spectra; **(b)** Ce 4d XP spectra.

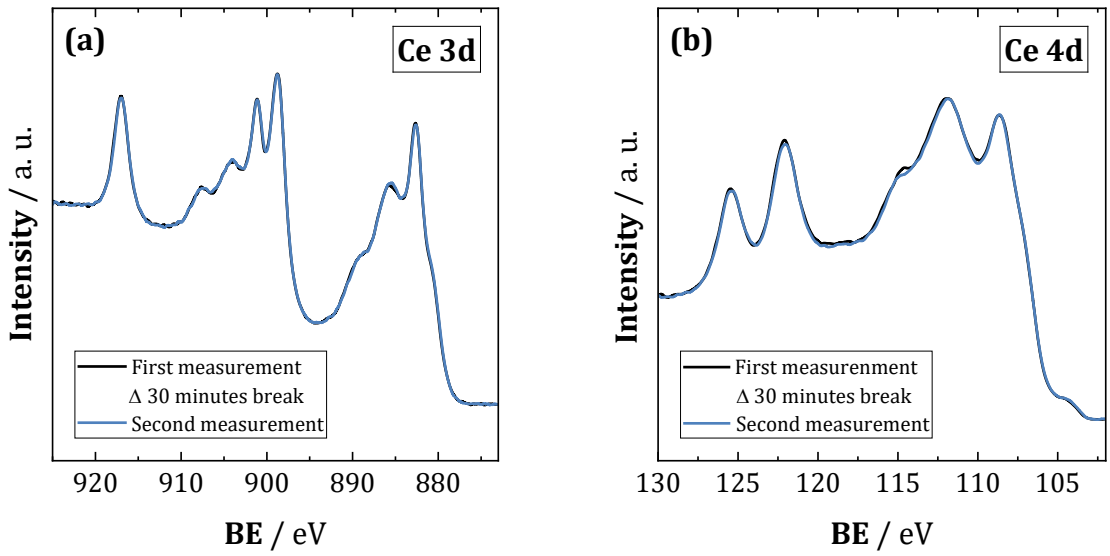

Figure 9.11: Comparison of the first XP spectrum obtained for the cerium oxide film of the CeO_{2-x}/Pt/YSZ/Pt system after anodic polarization (black) and a further spectrum that was obtained 30 minutes after the first XPS measurement was performed (blue); measurements were conducted under OCV conditions; **(a)** Ce 3d XP spectra; **(b)** Ce 4d XP spectra.

10 Conclusion and Outlook

Conclusion

This work focused on the preparation, characterization and testing of an electrochemical pumping system that enables controlled modification of the oxygen deficiency *x* in a CeO_{2-x}(111) film. Such a system would be desirable for fundamental investigations of the Deacon process as previous studies[4,5] reported a clear correlation between oxygen deficiency and catalytic activity.

Based on the Pt/YSZ electrode system[6,7], a respective system was successfully devised within this work. By applying an electric potential to a respective CeO_{2-x}/Pt/YSZ/Pt system, controlled oxidation and reduction of a CeO_{2-x}(111) film could be reached. For establishment of this system, several issues had to be investigated. These include the preparation and (spectroscopic) characterization of cerium oxide films, as well as the electrochemical characterization of Pt/YSZ/Pt and CeO_{2-x}/Pt/YSZ/Pt systems. Beyond that, an *operando* technique was devised enabling *proof of principle* measurements. In the following, key findings from these investigations are summarized.

First, dense and crystalline cerium oxide films with a (111) preferential orientation were prepared by pulsed laser deposition on both dense and de-wetted Pt(111) thin films (see Chapters 5 and 8). Raman spectroscopy and X-ray photoelectron spectroscopy revealed the presence of oxygen vacancies within the films after preparation. Subsequent annealing in air (p = 1 atm) led to the disappearance of these vacancies (see Chapter 6), resulting in nearly stoichiometric CeO_{2-x} with an oxygen deficiency *x* of approximately zero.

In a further step, Pt/YSZ/Pt cell types were prepared and electrochemically characterized by impedance spectroscopy (see Chapter 7). Here, dense and de-wetted platinum electrodes were compared. For the de-wetted platinum electrode, temperature dependence as well as the inhibition of the oxygen exchange reaction were presented. The inhibition was ascribed to the formation of platinum oxides, however, without spectroscopic proof. For both Pt/YSZ/Pt cells, a decrease of activation energies for YSZ oxygen ion conduction with increasing temperature was obtained.

Performing impedance spectroscopy (EIS), cyclic voltammetry (CV) and potentiostatic polarization experiments with a CeO_{2-x}/Pt/YSZ/Pt prototype system, influences caused by the corresponding cerium oxide film were found (see Chapter 8). In EIS and CV measurements, contributions were observed, which did not occur in a Pt/YSZ/Pt reference system. In potentiostatic polarization experiments, differences in anodic and cathodic currents were observed, which were also ascribed to the cerium oxide film. All results were referred to the Ce^{4+}/Ce^{3+} redox couple and gave a first hint that the cerium oxide film is electrochemically integrated in the CeO_{2-x}/Pt/YSZ/Pt system.

Finally, an *operando* setup was presented that enabled XPS measurements at elevated temperatures ($\vartheta_{Sample} \approx 385$ °C) and after applying an electric potential to the CeO_{2-x}/Pt/YSZ/Pt system. By that, the working principle meaning the oxidation and reduction of the corresponding cerium oxide film could be proven.

Outlook

In this work, an *operando* XPS setup was successfully employed to verify the working principle of the CeO_{2-x}/Pt/YSZ/Pt system. However, only a few polarization experiments were conducted with this setup, meaning that further investigations are required to study the effects of polarization in greater detail. In particular, the applied potential and the polarization time could be analyzed in a systematic way. It would be, in general, interesting to determine to which extent the cerium oxide film can be oxidized or reduced. Here, stability of the system should also be examined since applying high potentials for longer time may induce irreversible changes in the film electrodes[50,58,64,65] or in the electrolyte[66,67].

The results obtained from XPS measurements only provided information on the oxidation state of the top layers of the cerium oxide film. Raman spectroscopy, by contrast, is a more bulk-sensitive technique that is also sensitive to oxygen vacancies in cerium oxide films[22]. Therefore, devising a suitable setup for performing *operando* Raman measurements on the CeO_{2-x}/Pt/YSZ/Pt system would be desirable as it could complement the results obtained from *operando* XPS. In literature, various setups have been reported that enable Raman measurements on electrochemical systems at elevated temperatures[122–124].

In a further step, the CeO_{2-x}/Pt/YSZ/Pt system can be transferred to a suitable reactor allowing a detailed study on the correlation between Deacon activity and oxygen vacancies in cerium oxide (surfaces). By that, the application of cerium oxide as catalyst could be optimized, aiming at a viable alternative to expensive ruthenium-based catalysts.

11 Appendix

Chapter 5:

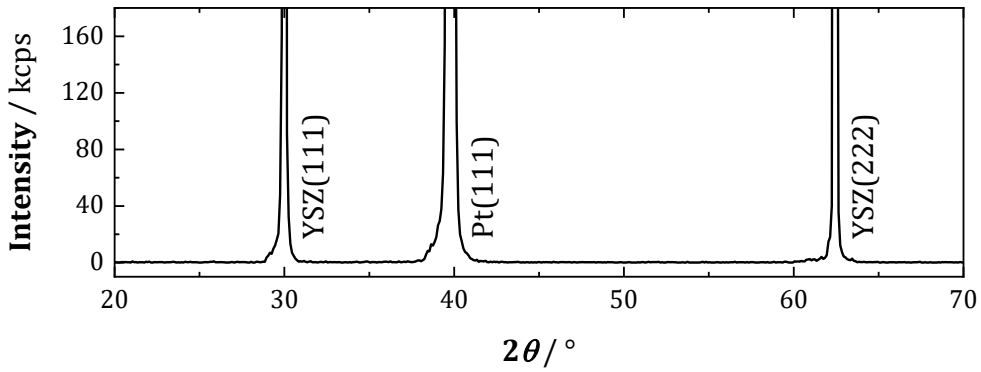

Figure 11.1: XRD pattern for a platinum film deposited on the polished YSZ(111) substrate side (PLD parameters: E = 400 mJ, f = 6 Hz, p(Ar) = 2 Pa, ϑ_{Heater} = 700 °C, N = 7,200). Reflex positions are 30.0°, 39.8° and 62.4°. The film had a thickness of around 160 nm.

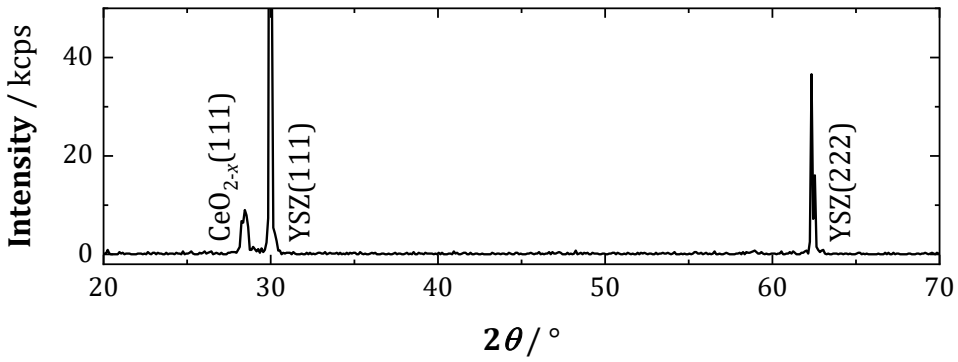

Figure 11.2: XRD pattern for a cerium oxide film deposited on the polished YSZ(111) substrate side (PLD parameters: E = 300 mJ, f = 10 Hz, p(Ar) = 2 Pa, ϑ_{Heater} = 300 °C, N = 36,000). Reflex positions are 28.4°, 30.0° and 62.4°. The film had a thickness of around 4 µm.

Chapter 6:

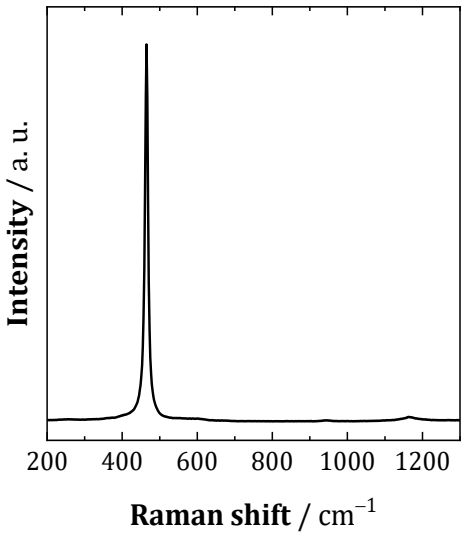

Figure 11.3: Raman spectrum of the CeO_2 target used for PLD depositions. The main peak, *i.e.*, the F_{2g} mode, is at around 465 cm^{-1}.

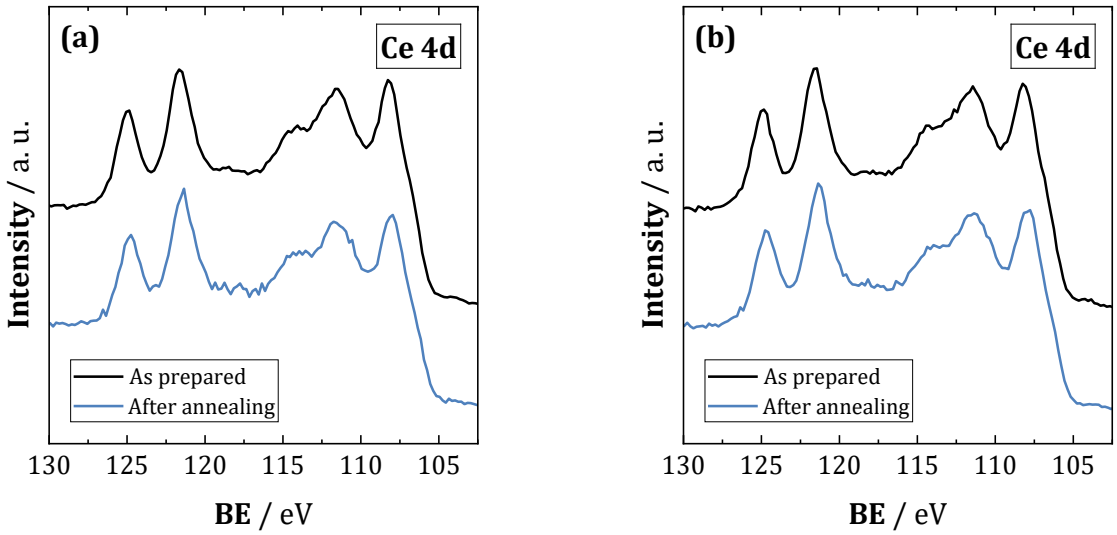

Figure 11.4: Ce 4d XP spectra for cerium oxide films after PLD preparation (black) and after annealing in air (blue) (ϑ = 600 °C, t = 12 h, p(air) = 1 atm); **(a)** CeO_{2-x}/Pt/YSZ sample; **(b)** CeO_{2-x}/YSZ sample.

Chapter 7:

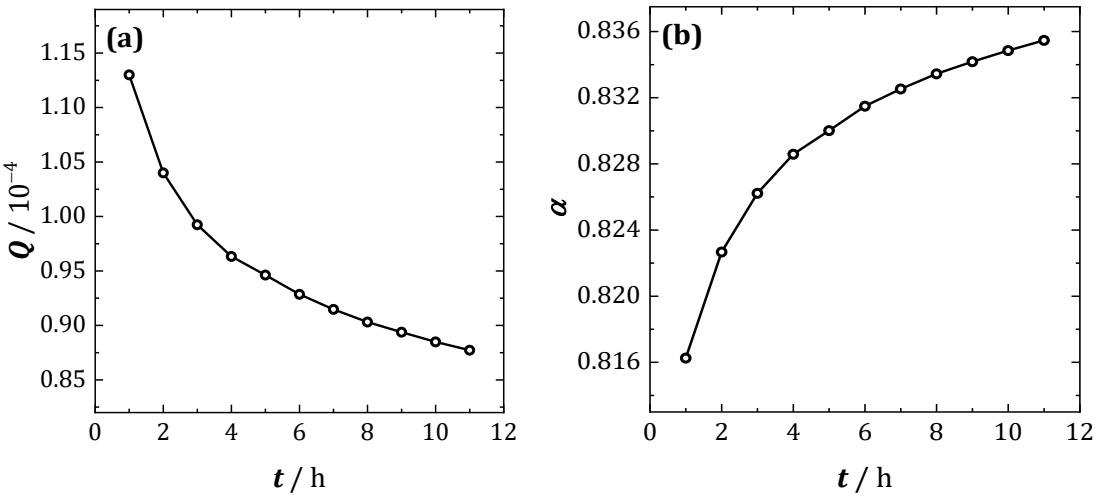

Figure 11.5: EIS data obtained for the Pt/YSZ/Pt cell with two dense platinum film electrodes during annealing in air (ϑ = 600 °C, t = 12 h, p(air) = 1 atm); the data belong to the CPE in the R_{YSZ}-*RL*-CPE circuit; **(a)** development of corresponding Q values during dwell time t; **(b)** development of corresponding α values during dwell time t. Lines are drawn between data points to indicate the trend, respectively.

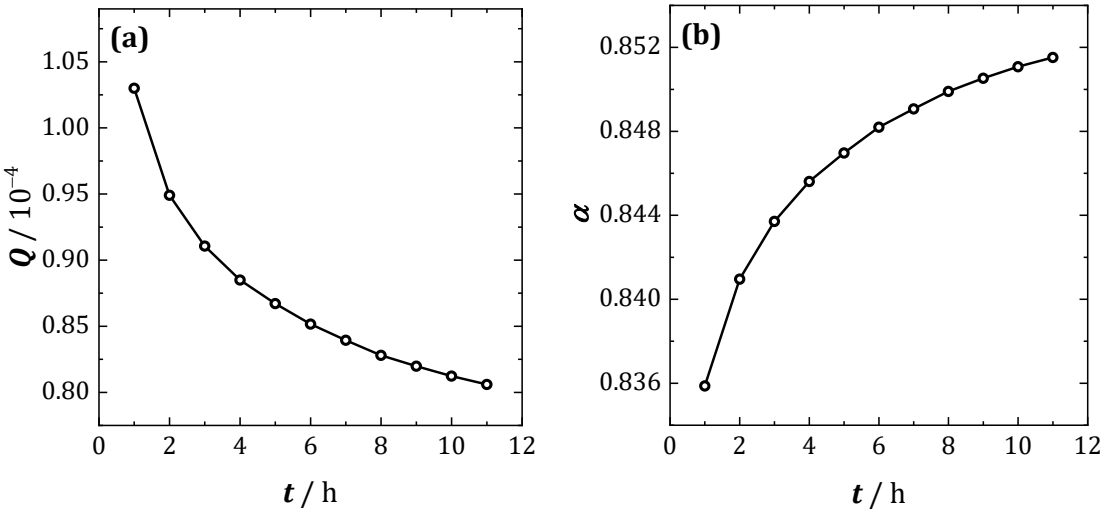

Figure 11.6: EIS data obtained for the Pt/YSZ/Pt cell with one de-wetted and one dense platinum film electrode during annealing in air (ϑ = 600 °C, t = 12 h, p(air) = 1 atm); the data belong to the CPE in the R_{YSZ}-*RL*-R_{EP}CPE circuit; **(a)** development of corresponding Q values during dwell time t; **(b)** development of corresponding α values during dwell time t. Lines are drawn between data points to indicate the trend, respectively.

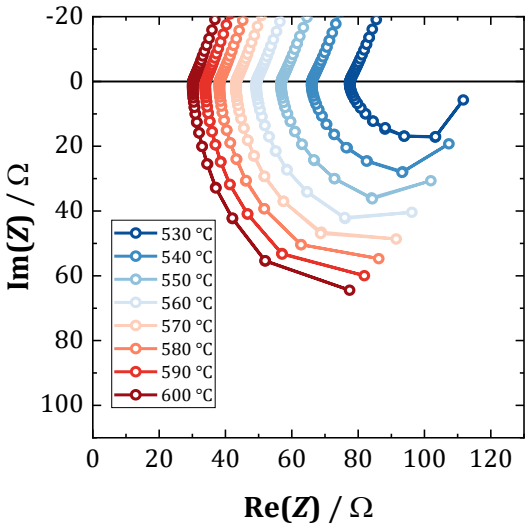

Figure 11.7: High-frequency part of Nyquist plots obtained for the Pt/YSZ/Pt cell with one de-wetted platinum thin film and one dense platinum thin film for various temperatures (p(air) = 1 atm).

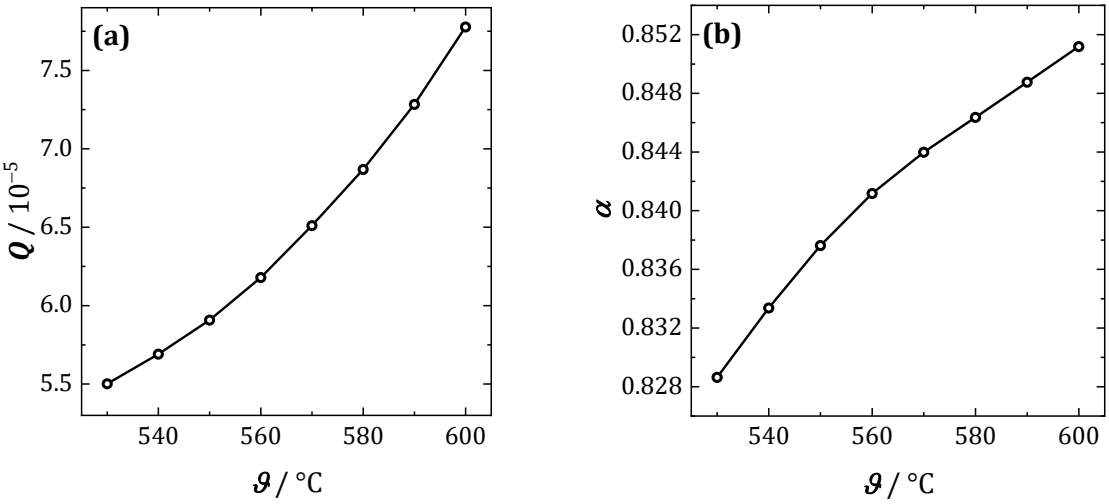

Figure 11.8: EIS data obtained for the Pt/YSZ/Pt cell with one de-wetted and one dense platinum film electrode for various temperatures (p(air) = 1 atm); the data belong to the CPE in the R_{YSZ}-RL-R_{EP}CPE circuit; **(a)** temperature dependence of corresponding Q values; **(b)** temperature dependence of corresponding α values. Lines are drawn between data points to indicate the trend, respectively.

Chapter 8:

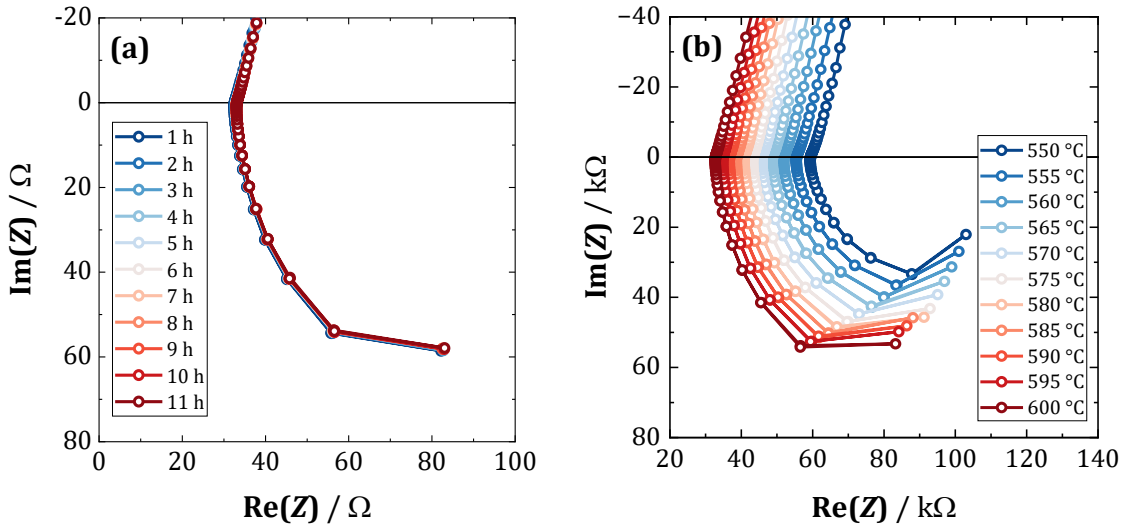

Figure 11.9: High-frequency parts of Nyquist plots obtained for the CeO_{2-x}/Pt/YSZ/Pt system; **(a)** during annealing in air (ϑ = 600 °C, t = 12 h, p(air) = 1 atm); time represents dwell time at 600 °C; **(b)** at various temperatures.

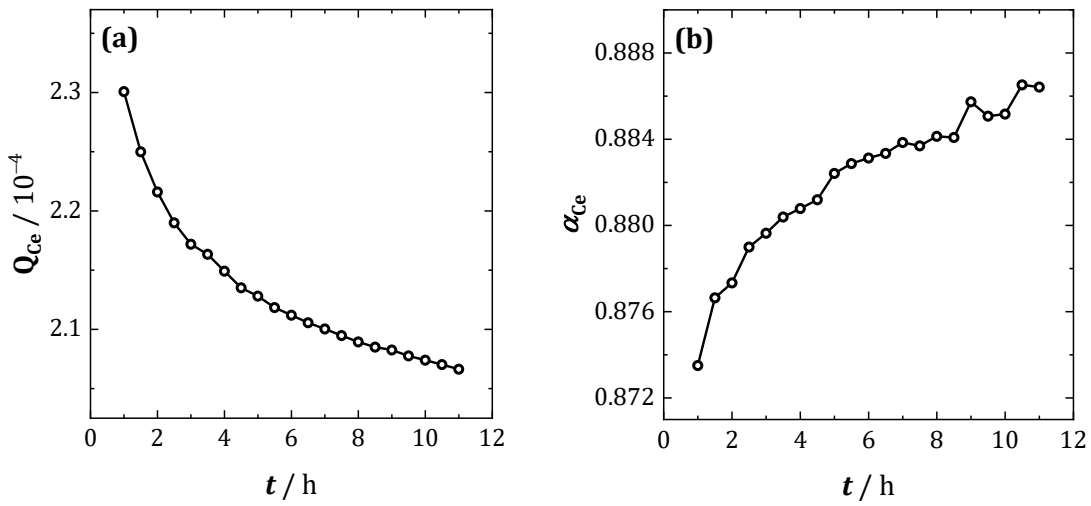

Figure 11.10: EIS data obtained for the CeO_{2-x}/Pt/YSZ/Pt system during annealing (ϑ = 600 °C, t = 12 h, p(air) = 1 atm); the data belong to the CPE_{Ce} in the R_{YSZ}-R_LL-$R_{Ce}$$CPE_{Ce}$-$R_{EP}$$CPE_{EP}$ circuit; **(a)** development of corresponding Q values during dwell time t; **(b)** development of corresponding α values during dwell time t. Lines are drawn between data points to indicate the trend, respectively.

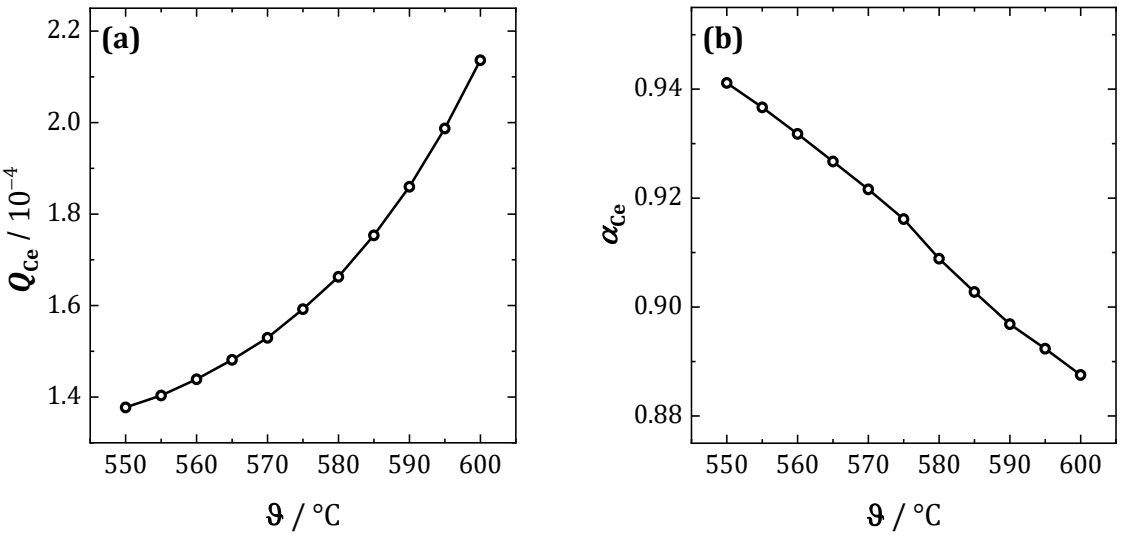

Figure 11.11: EIS data obtained for the CeO_{2-x}/Pt/YSZ/Pt system for various temperatures (p(air) = 1 atm); the data belong to the CPE_{Ce} in the R_{YSZ}-R_LL-$R_{Ce}$$CPE_{Ce}$-$R_{EP}$$CPE_{EP}$ circuit; **(a)** temperature dependence of corresponding Q values; **(b)** temperature dependence of corresponding α values. Lines are drawn between data points to indicate the trend, respectively.

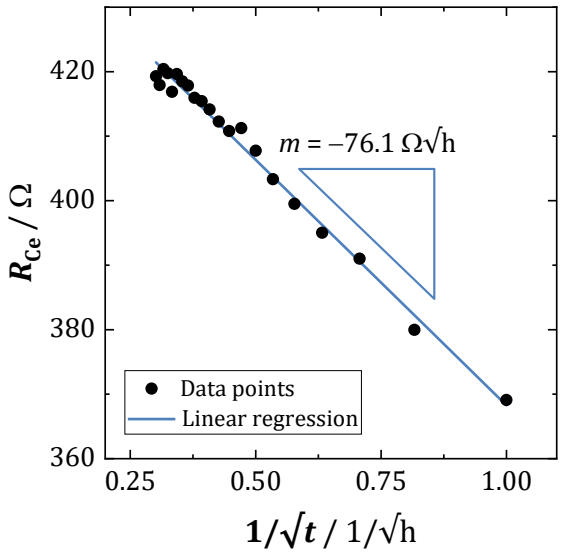

Figure 11.12: Plotting of R_{Ce} values versus inverse square root of dwell time t with linear regression. This graph contains the same data as shown in Figure 8.8 (a).

Chapter 9:

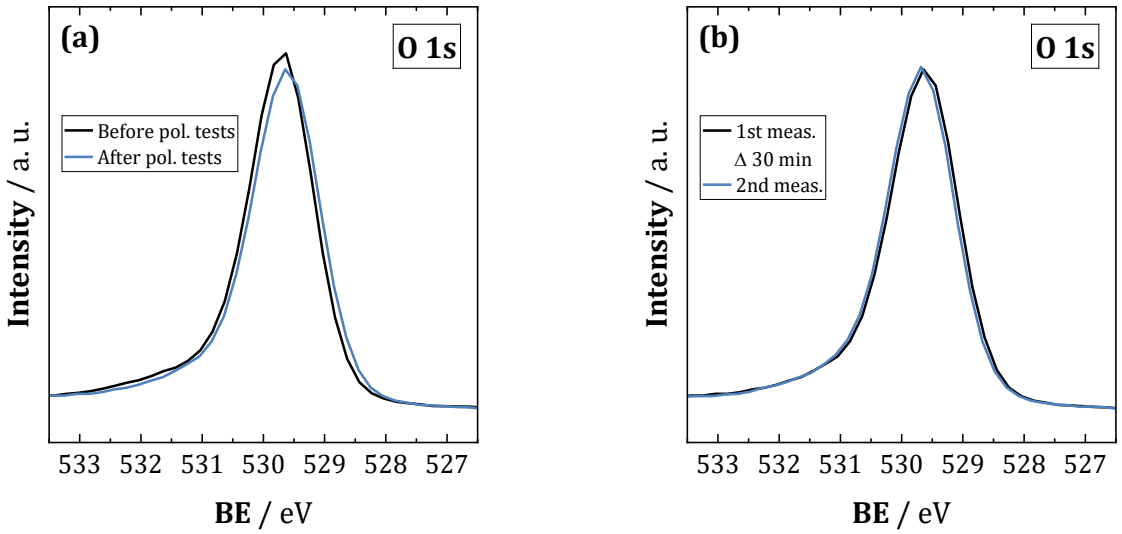

Figure 11.13: O 1s XP spectra obtained for the cerium oxide film of the CeO_{2-x}/Pt/YSZ/Pt system during *operando* experiments (ϑ_{Sample} ≈ 385 °C); measurements were conducted under OCV conditions, respectively; **(a)** comparison of spectra obtained before and after cathodic polarization tests; **(b)** comparison of first measurements after cathodic polarization tests and subsequent measurement taken 30 minutes later.

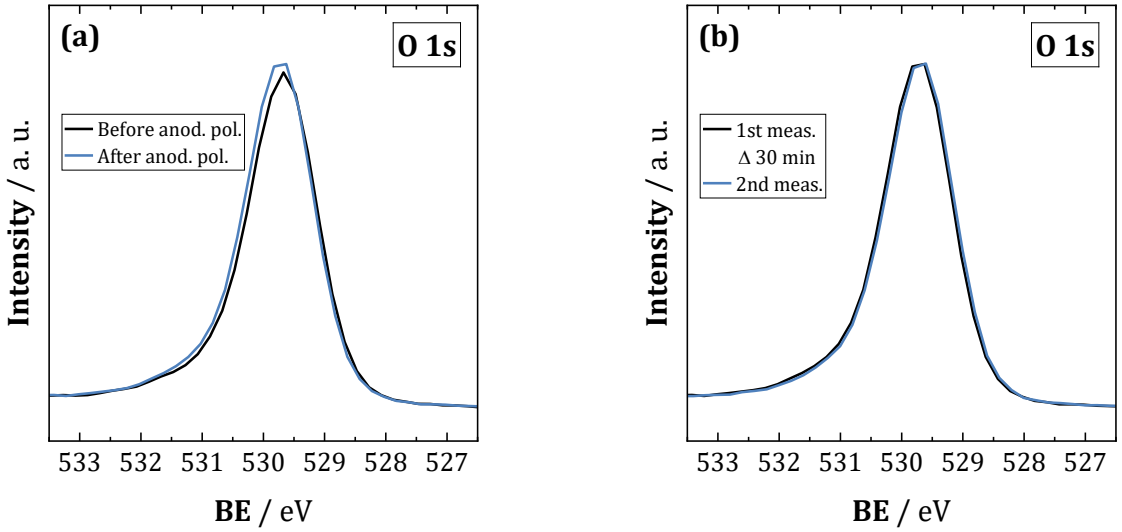

Figure 11.14: O 1s XP spectra obtained for the cerium oxide film of the CeO_{2-x}/Pt/YSZ/Pt system during *operando* experiments (ϑ_{Sample} ≈ 385 °C); measurements were conducted under OCV conditions, respectively; **(a)** comparison of spectra obtained before and after anodic polarization; **(b)** comparison of first measurements after anodic polarization and subsequent measurement taken 30 minutes later.

12 List of Abbreviations

AP	Anodic peak
a. u.	Arbitrary units
BE	Binding energy
CE	Counter electrode
CP	Cathodic peak
CPE	Constant phase element
CV	Cyclic voltammetry
EIS	Electrochemical impedance spectroscopy
EP	Electrode process
EPOC	Electrochemical promotion of catalysis
FWHM	Full width at half maximum
(k)cps	(Kilo) counts per second
NEMCA	Non-Faradaic electrochemical modification of catalytic activity
OSC	Oxygen storage capacity
POL	Polarization
PLD	Pulsed laser deposition
RE	Reference electrode
RS	Raman spectroscopy
SEM	Scanning electron microscopy
SOFC	Solid oxide fuel cell
TBC	Thermal barrier coating
TPB	Triple phase boundary

TWC	Three-way catalyst
UHV	Ultrahigh vacuum
WD	Working distance
WE	Working electrode
XPS	X-ray photoelectron spectroscopy
XRD	X-ray diffraction
YSZ	Yttria-stabilized zirconia

13 List of Symbols

α	Alpha value (corresponding to CPE)
α	Charge transfer coefficient (Equations (4.6) and (4.7))
Γ	Jump frequency
θ	Angle
ϑ	Temperature (in °C)
$\vartheta_{\mathrm{Heater}}$	Heater temperature
λ	Wavelength
λ_{ϑ}	Thermal conductivity
ν	Scan rate (in context of CV)
ν	Attempt frequency (Equation (3.4))
ρ	Specific resistivity
σ	Specific conductivity
σ_0	Conductivity constant
ϕ	Work function
φ	Phase angle
ω	Frequency
A	Area (of the electrode)
A	Laser spot size (in context of PLD)
a	Jump distance
C	Capacitance
c	Concentration
D	Diffusion coefficient

D_0	Diffusion constant
d	Distance
E	Electrode potential
E	Electric field (Figure 3.8)
E	(Pulse) energy (in context of PLD)
e	Elementary charge
E^0	Standard electrode potential
E_A	Activation energy
E_{AP}	Anodic peak potential
E_B	Binding energy
E_{CP}	Cathodic peak potential
E_K	Kinetic energy
E_P	Peak potential
E_{POL}	Polarization potential
E_R	Reverse potential
F	Faraday constant
f	Pulse frequency
Δg_m	Energy barrier
ΔH^0	Reaction enthalpy
h	Planck constant
I	Current
I_{AC}	Alternating current
I_{AP}	Anodic peak current
I_{CP}	Cathodic peak current
I_P	Peak current
$I_{t(POL)}$	Current value at t_{POL}
i	Imaginary unit
$\mathrm{Im}(Z)$	Imaginary part of impedance Z
J	Flux
k	Reaction rate constant
k_B	Boltzmann constant
L	Inductance

m	Slope (of a linear regression)
N	Number of pulses
n	Diffraction order (Bragg's law (4.1))
n	Number of electrons to be converted during a redox process
p	Pressure
Q	Q value (corresponding to CPE)
Q	Converted charge (in context of polarization)
R	Gas constant
R	Resistance
Re(Z)	Real part of impedance Z
T	Temperature (in K)
t	Time
t_{POL} / t(POL)	Polarization time
U_{AC}	Alternating voltage
$V_O^{\bullet\bullet}$ / V	Oxygen vacancy
V	Volume (of a substrate)
x	Oxygen deficiency
Z	Charge number (Figure 3.8)
Z	Impedance (in context of EIS)

14 Bibliography

1 Euro Chlor, https://www.eurochlor.org/news/august-2025-chlorine-production/, (accessed 9 October 2025).

2 I. Moussallem, J. Jörissen, U. Kunz, S. Pinnow and T. Turek, Chlor-alkali electrolysis with oxygen depolarized cathodes: history, present status and future prospects, *J Appl Electrochem*, 2008, **38**, 1177–1194.

3 K. Seki, Development of RuO_2/Rutile-TiO_2 Catalyst for Industrial HCl Oxidation Process, *Catal Surv Asia*, 2010, **14**, 168–175.

4 A. P. Amrute, C. Mondelli, M. Moser, G. Novell-Leruth, N. López, D. Rosenthal, R. Farra, M. E. Schuster, D. Teschner, T. Schmidt and J. Pérez-Ramírez, Performance, structure, and mechanism of CeO_2 in HCl oxidation to Cl_2, *Journal of Catalysis*, 2012, **286**, 287–297.

5 C. Li, Y. Sun, I. Djerdj, P. Voepel, C.-C. Sack, T. Weller, R. Ellinghaus, J. Sann, Y. Guo, B. M. Smarsly and H. Over, Shape-Controlled CeO_2 Nanoparticles: Stability and Activity in the Catalyzed HCl Oxidation Reaction, *ACS Catal.*, 2017, **7**, 6453–6463.

6 W. C. Chueh, A. H. McDaniel, M. E. Grass, Y. Hao, N. Jabeen, Z. Liu, S. M. Haile, K. F. McCarty, H. Bluhm and F. El Gabaly, Highly Enhanced Concentration and Stability of Reactive Ce^{3+} on Doped CeO_2 Surface Revealed In Operando, *Chem. Mater.*, 2012, **24**, 1876–1882.

7 Z. A. Feng, M. L. Machala and W. C. Chueh, Surface electrochemistry of CO_2 reduction and CO oxidation on Sm-doped CeO_{2-x}: coupling between Ce^{3+} and carbonate adsorbates, *Phys. Chem. Chem. Phys.*, 2015, **17**, 12273–12281.

8 D. R. Mullins, The surface chemistry of cerium oxide, *Surface Science Reports*, 2015, **70**, 42–85.

9 C. C. Sack, *CeO_x(111)/Ru(0001) als Modellkatalysator für die HCl-Oxidation*, 2019.

10 V. Koller, *The Deacon Process from the Perspective of Surface Science: HCl Oxidation on CeO_{2-x}(111)/Ru (0001) Thin Films*, 2024.

11 R. Farra, S. Wrabetz, M. E. Schuster, E. Stotz, N. G. Hamilton, A. P. Amrute, J. Pérez-Ramírez, N. López and D. Teschner, Understanding CeO_2 as a Deacon catalyst by probe molecule adsorption and in situ infrared characterisations, *Phys. Chem. Chem. Phys.*, 2013, **15**, 3454–3465.

12 V. Koller, P. G. Lustemberg, A. Spriewald-Luciano, S. M. Gericke, A. Larsson, C. Sack, A. Preobrajenski, E. Lundgren, M. V. Ganduglia-Pirovano and H. Over, Critical Step in the HCl Oxidation Reaction over Single-Crystalline CeO_{2-x}(111): Peroxo-Induced Site Change of Strongly Adsorbed Surface Chlorine, *ACS Catal.*, 2023, **13**, 12994–13007.

13 V. Koller, C. Sack, P. Lustemberg, M. V. Ganduglia-Pirovano and H. Over, Dynamic Response of Oxygen Vacancies in the Deacon Reaction over Reduced Single Crystalline CeO_{2-x}(111) Surfaces, *J. Phys. Chem. C*, 2022, **126**, 13202–13212.

14 C. Sack, P. Lustemberg, V. Koller, M. V. Ganduglia-Pirovano and H. Over, Interaction of HCl with a CeO_2(111) Layer Supported on Ru(0001): A Theory and Experiment Combined Study, *J. Phys. Chem. C*, 2018, **122**, 19584–19592.

15 E. Riedel and C. Janiak, eds., *Anorganische Chemie*, De Gruyter, Berlin, Boston, 10th edn., 2022.

16 M. Mogensen, Physical, chemical and electrochemical properties of pure and doped ceria, *Solid State Ionics*, 2000, **129**, 63–94.

17 D. R. Lide, ed., *CRC Handbook of Chemistry and Physics*, CRC Press, Boca Raton, 2005.

18 D.-J. Kim, Lattice Parameters, Ionic Conductivities, and Solubility Limits in Fluorite-Structure MO_2 Oxide [M = Hf^{4+}, Zr^{4+}, Ce^{4+}, Th^{4+}, U^{4+}] Solid Solutions, *Journal of the American Ceramic Society*, 1989, **72**, 1415–1421.

19 A. Pfau and K. D. Schierbaum, The electronic structure of stoichiometric and reduced CeO_2 surfaces: an XPS, UPS and HREELS study, *Surface Science*, 1994, **321**, 71–80.

20 M. Romeo, K. Bak, J. El Fallah, F. Le Normand and L. Hilaire, XPS Study of the reduction of cerium dioxide, *Surface & Interface Analysis*, 1993, **20**, 508–512.

21 D. Mullins, S. Overbury and D. Huntley, Electron spectroscopy of single crystal and polycrystalline cerium oxide surfaces, *Surface Science*, 1998, **409**, 307–319.

22 R. Schmitt, A. Nenning, O. Kraynis, R. Korobko, A. I. Frenkel, I. Lubomirsky, S. M. Haile and J. L. M. Rupp, A review of defect structure and chemistry in ceria and its solid solutions, *Chemical Society Reviews*, 2020, **49**, 554–592.

23 D. Bevan and J. Kordis, Mixed oxides of the type MO_2 (fluorite)—M_2O_3—I oxygen dissociation pressures and phase relationships in the system CeO_2-Ce_2O_3 at high temperatures, *Journal of Inorganic and Nuclear Chemistry*, 1964, **26**, 1509–1523.

24 R. J. Panlener, R. N. Blumenthal and J. E. Garnier, A thermodynamic study of nonstoichiometric cerium dioxide, *Journal of Physics and Chemistry of Solids*, 1975, **36**, 1213–1222.

25 H. L. Tuller and A. S. Nowick, Defect Structure and Electrical Properties of Nonstoichiometric CeO_2 Single Crystals, *J. Electrochem. Soc.*, 1979, **126**, 209–217.

26 R. J. D. Tilley, *Defects in solids*, John Wiley & Sons, 2008.

27 T. Montini, M. Melchionna, M. Monai and P. Fornasiero, Fundamentals and Catalytic Applications of CeO_2-Based Materials, *Chemical reviews*, 2016, **116**, 5987–6041.

28 C. Sun, H. Li and L. Chen, Nanostructured ceria-based materials: synthesis, properties, and applications, *Energy Environ. Sci.*, 2012, **5**, 8475.

29 J.-H. Park and R. N. Blumenthal, Electronic Transport in 8 Mole Percent Y_2O_3-ZrO_2, *J. Electrochem. Soc.*, 1989, **136**, 2867–2876.

30 C. Ahamer, A. K. Opitz, G. M. Rupp and J. Fleig, Revisiting the Temperature Dependent Ionic Conductivity of Yttria Stabilized Zirconia (YSZ), *J. Electrochem. Soc.*, 2017, **164**, F790-F803.

31 J. A. Krogstad, M. Lepple, Y. Gao, D. M. Lipkin and C. G. Levi, Effect of Yttria Content on the Zirconia Unit Cell Parameters, *J. Am. Ceram. Soc.*, 2011, **94**, 4548–4555.

32 R. E. W. Casselton, Low field DC conduction in yttria-stabilized zirconia, *Phys. Stat. Sol. (a)*, 1970, **2**, 571–585.

33 A. I. Ioffe, D. S. Rutman and S. V. Karpachov, On the nature of the conductivity maximum in zirconia-based solid electrolytes, *Electrochimica Acta*, 1978, **23**, 141–142.

34 P. Manning, The kinetics of oxygen transport in 9.5 mol % single crystal yttria stabilised zirconia, *Solid State Ionics*, 1997, **100**, 1–10.

35 E. D. Wachsman and K. T. Lee, Lowering the temperature of solid oxide fuel cells, *Science*, 2011, **334**, 935–939.

36 B. C. Steele and A. Heinzel, Materials for fuel-cell technologies, *Nature*, 2001, **414**, 345–352.

37 N. Miura, T. Sato, S. A. Anggraini, H. Ikeda and S. Zhuiykov, A review of mixed-potential type zirconia-based gas sensors, *Ionics*, 2014, **20**, 901–925.

38 L. B. Chen, Yttria-Stabilized Zirconia Thermal Barrier Coatings — A Review, *Surf. Rev. Lett.*, 2006, **13**, 535–544.

39 J. W. Arblaster, Crystallographic Properties of Platinum, *Platinum Metals Review*, 1997, **41**, 12–21.

40 A. E. Hughes, N. Haque, S. A. Northey and S. Giddey, Platinum Group Metals: A Review of Resources, Production and Usage with a Focus on Catalysts, *Resources*, 2021, **10**, 93.

41 J. Poppe, S. Völkening, A. Schaak, E. Schütz, J. Janek and R. Imbihl, Electrochemical promotion of catalytic CO oxidation on Pt/YSZ catalysts under low pressure conditions, *Phys. Chem. Chem. Phys.*, 1999, **1**, 5241–5249.

42 A. Toghan, M. Greiner, A. Knop-Gericke and R. Imbihl, Identification of the surface species in electrochemical promotion: ethylene oxidation over a Pt/YSZ catalyst, *Phys. Chem. Chem. Phys.*, 2021, **23**, 21591–21598.

43 B. Luerßen, J. Janek and R. Imbihl, Electrocatalysis on Pt/YSZ electrodes, *Solid State Ionics*, 2001, **141-142**, 701–707.

44 J. Janek, M. Rohnke, B. Luerßen and R. Imbihl, Promotion of catalytic reactions by electrochemical polarization, *Phys. Chem. Chem. Phys.*, 2000, **2**, 1935–1941.

45 C. G. Vayenas, S. Bebelis and S. Ladas, Dependence of catalytic rates on catalyst work function, *Nature*, 1990, **343**, 625–627.

46 B. Luerßen, S. Günther, H. Marbach, M. Kiskinova, J. Janek and R. Imbihl, Photoelectron spectromicroscopy of electrochemically induced oxygen spillover at the Pt/YSZ interface, *Chemical Physics Letters*, 2000, **316**, 331–335.

47 B. Luerßen, J. Janek, S. Günther, M. Kiskinova and R. Imbihl, Microspectroscopy at a moving reduction front in zirconia solid electrolyte, *Phys. Chem. Chem. Phys.*, 2002, **4**, 2673–2679.

48 P. Vernoux, L. Lizarraga, M. N. Tsampas, F. M. Sapountzi, A. de Lucas-Consuegra, J.-L. Valverde, S. Souentie, C. G. Vayenas, D. Tsiplakides, S. Balomenou and E. A. Baranova, Ionically conducting ceramics as active catalyst supports, *Chemical reviews*, 2013, **113**, 8192–8260.

49 C. Bachmann, *Kinetic, electrochemical and spectroscopic investigation of the oxidation of CO and C_2H_4 on YSZ-supported metal model electrodes*, 2015.

50 E. Mutoro, C. Koutsodontis, B. Luerssen, S. Brosda, C. G. Vayenas and J. Janek, Electrochemical promotion of Pt(111)/YSZ(111) and Pt–FeO /YSZ(111) thin catalyst films: Electrocatalytic, catalytic and morphological studies, *Applied Catalysis B: Environmental*, 2010, **100**, 328–337.

51 S. B. Adler, Factors governing oxygen reduction in solid oxide fuel cell cathodes, *Chemical reviews*, 2004, **104**, 4791–4843.

52 J. Janek, B. Luerßen, E. Mutoro, H. Fischer and S. Günther, In situ imaging of electrode processes on solid electrolytes by photoelectron microscopy and microspectroscopy – the role of the three-phase boundary, *Top Catal*, 2007, **44**, 399–407.

53 A. K. Opitz and J. Fleig, Investigation of O_2 reduction on Pt/YSZ by means of thin film microelectrodes: The geometry dependence of the electrode impedance, *Solid State Ionics*, 2010, **181**, 684–693.

54 T. Ryll, H. Galinski, L. Schlagenhauf, P. Elser, J. L. M. Rupp, A. Bieberle-Hutter and L. J. Gauckler, Microscopic and Nanoscopic Three-Phase-Boundaries of Platinum Thin-Film Electrodes on YSZ Electrolyte, *Adv Funct Materials*, 2011, **21**, 565–572.

55 E. Mutoro, B. Luerßen, S. Günther and J. Janek, The electrode model system Pt(O_2)|YSZ: Influence of impurities and electrode morphology on cyclic voltammograms, *Solid State Ionics*, 2009, **180**, 1019–1033.

56 N. Baumann, E. Mutoro and J. Janek, Porous model type electrodes by induced dewetting of thin Pt films on YSZ substrates, *Solid State Ionics*, 2010, **181**, 7–15.

57 H. Pöpke, E. Mutoro, C. Raiß, B. Luerßen, M. Amati, M. K. Abyaneh, L. Gregoratti and J. Janek, The role of platinum oxide in the electrode system Pt(O_2)/yttria-stabilized zirconia, *Electrochimica Acta*, 2011, **56**, 10668–10675.

58 V. Vonk, S. Volkov, T. F. Keller, A. Hutterer, P. Lakner, F. Bertram, J. Fleig, A. K. Opitz and A. Stierle, Reversible Ultrathin PtO_x Formation at the Buried Pt/YSZ(111) Interface Studied In Situ under Electrochemical Polarization, *The journal of physical chemistry letters*, 2023, **14**, 2065–2071.

59 H. Pöpke, E. Mutoro, B. Luerssen and J. Janek, Oxidation of Platinum in the Epitaxial Model System Pt(111)/YSZ(111): Quantitative Analysis of an Electrochemically Driven PtO_x Formation, *J. Phys. Chem. C*, 2012, **116**, 1912–1920.

60 S. Sridhar, Effect of oxygen-containing species on the impedance of the Pt/ YSZ interface, *Solid State Ionics*, 1997, **100**, 17–22.

61 V. Stancovski, S. Sridhar and U. B. Pal, Thermodynamic Stability and Interfacial Impedance of Solid-Electrolyte Cells with Noble-Metal Electrodes, *Journal of Electroceramics*, 1999, **3**, 279–299.

62 T. Chao, K. Walsh and P. Fedkiw, Cyclic voltammetric study of the electrochemical formation of platinum oxide in a Pt/yttria-stabilized zirconia cell, *Solid State Ionics*, 1991, **47**, 277–285.

63 H. Pöpke, E. Mutoro, B. Luerßen and J. Janek, Oxygen reduction and oxidation at epitaxial model-type Pt(O_2)/YSZ electrodes – On the role of PtO_x formation on activation, passivation, and charge transfer, *Catalysis Today*, 2013, **202**, 12–19.

64 E. Mutoro, S. Günther, B. Luerßen, I. Valov and J. Janek, Electrode activation and degradation: Morphology changes of platinum electrodes on YSZ during electrochemical polarisation, *Solid State Ionics*, 2008, **179**, 1835–1848.

65 H. Pöpke, E. Mutoro, B. Luerßen and J. Janek, The potential of in situ-scanning electron microscopy — Morphology changes of electrically polarized thin film Pt(O_2)/YSZ model electrodes, *Solid State Ionics*, 2011, **189**, 56–62.

66 B. Luerßen, *In situ-mikrospektroskopische Untersuchungen an Pt/YSZ-Elektroden*, 2003.

67 J. Janek, Electrochemical blackening of yttria-stabilized zirconia - morphological instability of the moving reaction front, *Solid State Ionics*, 1999, **116**, 181–195.

68 Gold.de, https://www.gold.de/kurse/rutheniumpreis/, (accessed 15 December 2025).

69 H. Over and R. Schomäcker, What Makes a Good Catalyst for the Deacon Process?, *ACS Catal.*, 2013, **3**, 1034–1046.

70 J. Pérez-Ramírez, C. Mondelli, T. Schmidt, O. F.-K. Schlüter, A. Wolf, L. Mleczko and T. Dreier, Sustainable chlorine recycling via catalysed HCl oxidation: from fundamentals to implementation, *Energy Environ. Sci.*, 2011, **4**, 4786.

71 M. W. M. Hisham and S. W. Benson, Thermochemistry of the Deacon Process, *J. Phys. Chem.*, 1995, **99**, 6194–6198.

72 M. Capdevila-Cortada, G. Vilé, D. Teschner, J. Pérez-Ramírez and N. López, Reactivity descriptors for ceria in catalysis, *Applied Catalysis B: Environmental*, 2016, **197**, 299–312.

73 P. Luches, F. Pagliuca and S. Valeri, Morphology, Stoichiometry, and Interface Structure of CeO_2 Ultrathin Films on Pt(111), *J. Phys. Chem. C*, 2011, **115**, 10718–10726.

74 K.-D. Schierbaum, Ordered ultra-thin cerium oxide overlayers on Pt(111) single crystal surfaces studied by LEED and XPS, *Surface Science*, 1998, **399**, 29–38.

75 P. Luches, F. Pagliuca, S. Valeri and F. Boscherini, Structure of Ultrathin CeO_2 Films on Pt(111) by Polarization-Dependent X-ray Absorption Fine Structure, *J. Phys. Chem. C*, 2013, **117**, 1030–1036.

76 P. R. Willmott and J. R. Huber, Pulsed laser vaporization and deposition, *Rev. Mod. Phys.*, 2000, **72**, 315–328.

77 M. N. R. Ashfold, F. Claeyssens, G. M. Fuge and S. J. Henley, Pulsed laser ablation and deposition of thin films, *Chemical Society Reviews*, 2004, **33**, 23–31.

78 N. A. Shepelin, Z. P. Tehrani, N. Ohannessian, C. W. Schneider, D. Pergolesi and T. Lippert, A practical guide to pulsed laser deposition, *Chemical Society Reviews*, 2023, **52**, 2294–2321.

79 M. W. Sigrist, *Laser: Theorie, Typen und Anwendungen*, Springer Spektrum, Berlin, 8th edn., 2018.

80 M. Kleine-Boymann, *Ceria - zirconia thin films : influence of nanostructure and moisture on charge transport properties*, 2021.

81 R. Egerton, *Physical principles of electron microscopy*, 2005.

82 G. F. Harrington and J. Santiso, Back-to-Basics tutorial: X-ray diffraction of thin films, *J Electroceram*, 2021, **47**, 141–163.

83 R. Loudon, The Raman effect in crystals, *Advances in Physics*, 1964, **13**, 423–482.

84 F. A. Stevie and C. L. Donley, Introduction to x-ray photoelectron spectroscopy, *J. Vac. Sci. Technol. A*, 2020, **38**.

85 E. Mutoro, E. J. Crumlin, H. Pöpke, B. Luerssen, M. Amati, M. K. Abyaneh, M. D. Biegalski, H. M. Christen, L. Gregoratti, J. Janek and Y. Shao-Horn, Reversible Compositional Control of Oxide Surfaces by Electrochemical Potentials, *J. Phys. Chem. Lett.*, 2012, **3**, 40–44.

86 A.-K. Huber, M. Falk, M. Rohnke, B. Luerssen, L. Gregoratti, M. Amati and J. Janek, In situ study of electrochemical activation and surface segregation of the SOFC electrode material $La_{0.75}Sr_{0.25}Cr_{0.5}Mn_{0.5}O_{(3\pm\delta)}$, *Phys. Chem. Chem. Phys.*, 2012, **14**, 751–758.

87 A. K. Opitz, A. Nenning, C. Rameshan, M. Kubicek, T. Götsch, R. Blume, M. Hävecker, A. Knop-Gericke, G. Rupprechter, B. Klötzer and J. Fleig, Surface Chemistry of Perovskite-Type Electrodes During High Temperature CO_2 Electrolysis Investigated by Operando Photoelectron Spectroscopy, *ACS applied materials & interfaces*, 2017, **9**, 35847–35860.

88 A.-K. Huber, M. Falk, M. Rohnke, B. Luerssen, M. Amati, L. Gregoratti, D. Hesse and J. Janek, In situ study of activation and de-activation of LSM fuel cell cathodes – Electrochemistry and surface analysis of thin-film electrodes, *Journal of Catalysis*, 2012, **294**, 79–88.

89 J. Chastain, *Handbook of X-ray photoelectron spectroscopy*, 1992.

90 A. C. Lazanas and M. I. Prodromidis, Electrochemical Impedance Spectroscopy-A Tutorial, *ACS measurement science au*, 2023, **3**, 162–193.

91 E. Laviron, General expression of the linear potential sweep voltammogram in the case of diffusionless electrochemical systems, *Journal of Electroanalytical Chemistry and Interfacial Electrochemistry*, 1979, **101**, 19–28.

92 A. J. Bard, L. R. Faulkner and H. S. White, *Electrochemical Methods. Fundamentals and Applications*, John Wiley & Sons, 2022.

93 G. Beck, H. Fischer, E. Mutoro, V. Srot, K. Petrikowski, E. Tchernychova, M. Wuttig, M. Rühle, B. Luerßen and J. Janek, Epitaxial Pt(111) thin film electrodes on YSZ(111) and YSZ(100) — Preparation and characterisation, *Solid State Ionics*, 2007, **178**, 327–337.

94 G. Beck, H. Pöpke, B. Luerßen and J. Janek, Microstructure of platinum films on YSZ prepared by pulsed laser deposition, *Journal of Crystal Growth*, 2011, **322**, 95–102.

95 G. Beck, C. Bachmann, R. Bretzler and R. Kmeth, Thermal stability of platinum, palladium and silver films on yttrium-stabilised zirconia, *Thin Solid Films*, 2014, **573**, 164–175.

96 A. Farkas, K. Zalewska-Wierzbicka, C. Bachmann, J. Goritzka, D. Langsdorf, O. Balmes, J. Janek and H. Over, High Pressure Carbon Monoxide Oxidation over Platinum (111), *J. Phys. Chem. C*, 2013, **117**, 9932–9942.

97 G. Balakrishnan, S. T. Sundari, P. Kuppusami, P. C. Mohan, M. P. Srinivasan, E. Mohandas, V. Ganesan and D. Sastikumar, A study of microstructural and optical properties of nanocrystalline ceria thin films prepared by pulsed laser deposition, *Thin Solid Films*, 2011, **519**, 2520–2526.

98 G. Balakrishnan, A. K. Panda, C. M. Raghavan, A. Singh, M. N. Prabhakar, E. Mohandas, P. Kuppusami and J. i. Song, Microstructure, optical and dielectric properties of cerium oxide thin films prepared by pulsed laser deposition, *J Mater Sci: Mater Electron*, 2019, **30**, 16548–16553.

99 D. R. Mullins, P. M. Albrecht, T.-L. Chen, F. C. Calaza, M. D. Biegalski, H. M. Christen and S. H. Overbury, Water Dissociation on CeO_2(100) and CeO_2(111) Thin Films, *J. Phys. Chem. C*, 2012, **116**, 19419–19428.

100 J. Zahnow, M. Bastianello, J. Janek and M. T. Elm, Defect Chemistry of Individual Grains with and without Grain Boundaries of Al-Doped Ceria Determined Using Well-Defined Microelectrodes, *J. Phys. Chem. C*, 2022, **126**, 2737–2746.

101 H. Li, P. Zhang, G. Li, J. Lu, Q. Wu and Y. Gu, Stress measurement for nonstoichiometric ceria films based on Raman spectroscopy, *Journal of Alloys and Compounds*, 2016, **682**, 132–137.

102 T. Suzuki, I. Kosacki, H. U. Anderson and P. Colomban, Electrical Conductivity and Lattice Defects in Nanocrystalline Cerium Oxide Thin Films, *Journal of the American Ceramic Society*, 2001, **84**, 2007–2014.

103 P. Cop, R. Maile, Y. Sun, O. Khalid, I. Djerdj, P. Esch, S. Heiles, H. Over and B. M. Smarsly, Impact of Aliovalent/Isovalent Ions (Gd, Zr, Pr, and Tb) on the Catalytic Stability of Mesoporous Ceria in the HCl Oxidation Reaction, *ACS Appl. Nano Mater.*, 2020, **3**, 7406–7419.

104 M. Guo, J. Lu, Y. Wu, Y. Wang and M. Luo, UV and visible Raman studies of oxygen vacancies in rare-earth-doped ceria, *Langmuir : the ACS journal of surfaces and colloids*, 2011, **27**, 3872–3877.

105 T. Tsuchiya, S. Miyoshi, Y. Yamashita, H. Yoshikawa, K. Terabe, K. Kobayashi and S. Yamaguchi, Room temperature redox reaction by oxide ion migration at carbon/Gd-doped CeO_2 heterointerface probed by an in situ hard x-ray photoemission and soft x-ray absorption spectroscopies, *Science and Technology of Advanced Materials*, 2013, **14**, 45001.

106 N. Kainbayev, M. Sriubas, D. Virbukas, Z. Rutkuniene, K. Bockute, S. Bolegenova and G. Laukaitis, Raman Study of Nanocrystalline-Doped Ceria Oxide Thin Films, *Coatings*, 2020, **10**, 432.

107 S. A. Acharya, V. M. Gaikwad, S. W. D'Souza and S. R. Barman, Gd/Sm dopant-modified oxidation state and defect generation in nano-ceria, *Solid State Ionics*, 2014, **260**, 21–29.

108 J. E. Spanier, R. D. Robinson, F. Zhang, S.-W. Chan and I. P. Herman, Size-dependent properties of CeO_{2-y} nanoparticles as studied by Raman scattering, *Phys. Rev. B*, 2001, **64**, 245407.

109 Z. Wu, M. Li, J. Howe, H. M. Meyer and S. H. Overbury, Probing defect sites on CeO_2 nanocrystals with well-defined surface planes by Raman spectroscopy and O_2 adsorption, *Langmuir : the ACS journal of surfaces and colloids*, 2010, **26**, 16595–16606.

110 M. A. Henderson, C. L. Perkins, M. H. Engelhard, S. Thevuthasan and C. Peden, Redox properties of water on the oxidized and reduced surfaces of CeO_2, *Surface Science*, 2003, **526**, 1–18.

111 G. Praline, B. E. Koel, R. L. Hance, H.-I. Lee and J. M. White, X-Ray photoelectron study of the reaction of oxygen with cerium, *Journal of Electron Spectroscopy and Related Phenomena*, 1980, **21**, 17–30.

112 N. Bosio, A. Schaefer and H. Grönbeck, Can oxygen vacancies in ceria surfaces be measured by O1s photoemission spectroscopy?, *Journal of physics. Condensed matter : an Institute of Physics journal*, 2022, **34**, 174004.

113 M. Filal, Ionic conductivity of yttrium-doped zirconia and the "composite effect", *Solid State Ionics*, 1995, **80**, 27–35.

114 Y. Arachi, Electrical conductivity of the ZrO_2–Ln_2O_3 (Ln=lanthanides) system, *Solid State Ionics*, 1999, **121**, 133–139.

115 S. Ikeda, O. Sakurai, K. Uematsu, N. Mizutani and M. Kato, Electrical conductivity of yttria-stabilized zirconia single crystals, *J Mater Sci*, 1985, **20**, 4593–4600.

116 A. Jaccoud, G. Fóti, R. Wüthrich, H. Jotterand and C. Comninellis, Effect of microstructure on the electrochemical behavior of Pt/YSZ electrodes, *Top Catal*, 2007, **44**, 409–417.

117 A. Jaccoud, G. Fóti and C. Comninellis, Electrochemical investigation of platinum electrode in solid electrolyte cell, *Electrochimica Acta*, 2006, **51**, 1264–1273.

118 J. Yi, A. Kaloyannis and C. G. Vayenas, High temperature cyclic voltammetry of Pt catalyst-electrodes in solid electrolyte cells, *Electrochimica Acta*, 1993, **38**, 2533–2539.

119 P. Luches, F. Pagliuca and S. Valeri, Structural and morphological modifications of thermally reduced cerium oxide ultrathin epitaxial films on Pt(111), *Phys. Chem. Chem. Phys.*, 2014, **16**, 18848–18857.

120 C. Barth, C. Laffon, R. Olbrich, A. Ranguis, P. Parent and M. Reichling, A perfectly stoichiometric and flat CeO_2(111) surface on a bulk-like ceria film, *Sci Rep*, 2016, **6**, 21165.

121 J. Wang, D. N. Mueller and E. J. Crumlin, Recommended strategies for quantifying oxygen vacancies with X-ray photoelectron spectroscopy, *Journal of the European Ceramic Society*, 2024, **44**, 116709.

122 C. Solís, M. Balaguer and J. M. Serra, In Situ Raman Characterization of SOFC Materials in Operational Conditions: A Doped Ceria Study, *Membranes*, 2020, **10**, 148.

123 J. D. Kirtley, D. M. Halat, M. D. McIntyre, B. C. Eigenbrodt and R. A. Walker, High-temperature "spectrochronopotentiometry": correlating electrochemical performance with in situ Raman spectroscopy in solid oxide fuel cells, *Analytical chemistry*, 2012, **84**, 9745–9753.

124 X. Li, K. Blinn, D. Chen and M. Liu, In Situ and Surface-Enhanced Raman Spectroscopy Study of Electrode Materials in Solid Oxide Fuel Cells, *Electrochem. Energ. Rev.*, 2018, **1**, 433–459.